UNIVERSITY OF CALIFORNIA, SAN DIEGO

The Inversion of Vertical Current Shear from X-Band Observations of the Wavefield

A dissertation submitted in partial satisfaction of the
requirements for the degree
Doctor of Philosophy

in

Oceanography

by

Jeffrey Daniel Campana

Committee in charge:

W. Kendall Melville, Co-Chair
Eric Terrill, Co-Chair
Falk Feddersen
Eugene Pawlak
Robert Pinkel

2016

The Dissertation of Jeffrey Daniel Campana is approved, and it is acceptable in quality and form for publication on microfilm and electronically:

Co-Chair

Co-Chair

University of California, San Diego

2016

EPIGRAPH

Think and wonder. Wonder and think.

– Dr. Seuss

TABLE OF CONTENTS

LIST OF FIGURES

LIST OF TABLES

ACKNOWLEDGEMENTS

I would first like to thank my family for their unending love and support. I would truly not be where I am without you all. Thanks Mom and Dad for being there every step of the way. Thank you, Becky for always ensuring I write good. Amanda, your love, patience, and encouragement has kept me sane throughout this process. Thank you for being an incredible fiancée, travel companion, dog mom, and, of course, dive buddy.

Thank you to Eric Terrill for the invaluable advice and support during my time here at Scripps. Also thank you to Ken Melville and my doctoral committee for your guidance over the past few years. I would also like to acknowledge the crews of the R/V Thomas G. Thompson, R/V Melville, R/V Sproul and R/P FLIP for their part in collecting the data used for this dissertation. Thanks to the CORDC lab for all of your assistance in engineering support in data collection and processing. Thanks to my office mate, Travis Schramek, for the countless stimulating white-board talks. Sam Wilson and Nick Cavanaugh, surf sessions with you guys made my time at Scripps so much better. Thank you for your friendship and support.

Chapters 1, in full, has been submitted to *the Journal of Atmospheric and Oceanic Technology* in 2015. Campana, Jeffrey; de Paolo, Anthony; Terrill, Eric J., Inversion of Vertical Shear from X-Band Observations in a River Inlet. The dissertation author was the primary investigator and author of this paper.

Chapters 2 is as it has been submitted to the *Journal of Atmospheric and Oceanic Technology* in 2016. Campana, Jeffrey; de Paolo, Anthony; Terrill, Eric J., A New

Inversion Method to Obtain Upper Ocean Current Shear using X-Band Observations of Deep Water Waves. The dissertation author was the primary investigator and author of this paper.

Chapter 3 is currently being prepared for submission for the publication of the material. Campana, Jeffrey; Terrill, Eric J. Observations of Wind-Driven Current Shear from the Inversion of X-Band Backscatter. The dissertation author was the primary investigator and author of this material.

VITA

2010 Bachelor of Science, University of California, San Diego

2016 Doctor of Philosophy, University of California, San Diego

FIELDS OF STUDY

Major Field: Applied Ocean Science

Studies in Applied Mathematics
Professors W.R. Young and E. Lauga

Studies in Physical Oceanography
Professors L.D. Talley and F. Feddersen

Studies in Linear and Nonlinear Ocean Waves
Professor W.K. Melville

Studies in Fluid Dynamics and Turbulence
Professors M.C. Hendershott and L. Armi

Studies in Physical Oceanographic Data Analysis
Professors R. Pinkel and D.L. Rudnick

ABSTRACT OF THE DISSERTATION

The Inversion of Vertical Current Shear from X-Band Observations of the Wavefield

by

Jeffrey Daniel Campana

Doctor of Philosophy in Oceanography

University of California, San Diego, 2016

W. Kendall Melville, Co-Chair
Eric Terrill, Co-Chair

Ocean surface waves propagate according to a dispersion relationship, which defines the relationship between a wave's wavenumber and its frequency. In the presence of underlying currents, waves are accelerated or decelerated, and this dispersion relationship is augmented by an additional Doppler shift. Furthermore, if the underlying currents are not depth-uniform, the Doppler shift-wavenumber relationship is non-linear. This dissertation focuses on the development of an inversion method to estimate current-depth profiles from a collection of wavelength-dependent Doppler shift measurements.

This process leverages Gaussian quadrature along with multiple least squares techniques to supply constraints to the otherwise inherently noisy inversion.

To measure Doppler shifts to be used as inputs into the inversion process, this work takes advantage of the sensitivity of marine X-band backscatter to space-time wavefield properties. Sequential images of backscatter are collected and, using a Fast Fourier Transform, are transformed into wavenumber-frequency space for current extraction.

X-Band backscatter (along with supporting wind and current measurements) was collected during two unique field campaigns. The first took place in June, 2013 as a part of the Riverine and Estuarine Transport Experiment 2 (RIVET2) field campaign in the Mouth of the Columbia River (MCR), Oregon. The second data set was collected from R/P FLIP in the Southern California bight in November 2013 as a part of the SoCal2013 experiment. From the strong, polarized currents in the MCR to the weaker, wind- and tide-driven currents of the deeper water off of California, the contrast between the data sets from the perspective of wave-current interaction is significant.

The results of the new inversion method from both data sets are compared to those measured by ADCPs. The depth- and time-dependence of the comparisons show that inverted currents successfully capture important geophysical phenomena such as depth-dependent tidal intrusions in the MCR and wind-driven current shear in deeper water. In deep water, the inversion is shown to provide reliable current estimates to a depth of $-k_{\min}{}^{-1}$, where $k_{\min}$ is the minimum measured wavenumber. Furthermore, the inversion is shown to supply valuable current information within the upper 2 m of the surface, filling a historical gap in current measurement capability.

Introduction

As wind blows over the ocean surface, mass, momentum, and energy are transferred from the atmosphere into the water. As waves build and break, momentum is injected into the surface layer, contributing to current generation. (Phillips 1966; Melville 1996). The time evolution and vertical structure of the near surface currents, therefore, contain valuable information about air-sea interaction processes. However, measurements of mean currents in the near surface using traditional methods are contaminated by surface heave, wave orbital motions, and bubble intrusions. Stewart and Joy (1974) described the phenomenon in which mean currents of different depths have unique effects on waves of different wavelengths. Specifically, shorter waves are only affected by shallow currents, whereas longer waves are also influenced by deeper currents. Using this concept, this dissertation is an investigation into the efficacy of leveraging broadband wavefield measurements to indirectly measure the vertical structure of near surface currents.

Wavefield observations used for this study are provided via the processing of marine X-Band backscatter images in the time-space domain. Transmitted EM waves from the X-Band interact resonantly with capillary waves via Bragg scattering. This resonant interaction leads to a peak in the reflected energy measured by the radar at the location of the Bragg scatterer. By transmitting EM pulses from a rotating antenna, the locations of capillary waves can be accurately measured in range and direction for each rotation. The interaction between capillary and underlying gravity waves causes the capillary waves to collect near the crest of the longer waves (Alpers 1981a). Combined

with the effect of geometric tilting on the forward face of the longer waves, the strongest reflection of the X-Band EM waves occurs just forward of the wave crest. Also, because the radar operates at near-grazing, wave crests shadow the troughs behind them. The combination of these effects leads to a backscatter map comprised of illuminated wave crests, and shadowed wave troughs. Sequential backscatter maps can therefore be used to provide information about a 2 dimensional wavefield in time and space (Young et al. 1985). A Fast Fourier Transform (FFT) transforms this time-space backscatter into the broadband wavenumber-frequency information used for the current inversion process in this work.

Stewart and Joy (1974) derived a relationship between the current-depth profile $\mathbf{u}(z)$ and the resulting change in the wave speed in deep water. They're results are expressed by

$$\hat{\mathbf{u}}(k) = 2k\int_{-\infty}^{0} \mathbf{u}(z)e^{2kz}dz$$

where $\hat{\mathbf{u}}(k)$ is the *effective velocity*, or the velocity representing the combined effects of the currents on a wave with wavenumber *k*. Part of this work will involve a detailed discussion about this integral relationship and its moderate depth counterpart (Kirby and Chen 1989). This includes a description of common approximations used in the remote sensing community to simplify current (and current shear) estimation from wave speed measurements. Also, a forward solution will be used to predict the wavefield's reaction to observed currents, providing insight into the relationship between the two. Finally,

Gaussian quadrature and various least squares techniques are used to develop an inversion method to calculate depth-current profiles from wavefield observations.

In Chapter 1, a method is developed to extract current shear from wavefield observations in a river inlet. The energetic, tidally-forced river inlet environment provides a unique test bed for current shear estimates as current signals are strong, periodic, and contain a large amount of shear due to the merging of fresh and salt water. Chapter 2 adapts this inversion process for use in a deep water environment. Challenges introduced by this transition include lower current signal and wave-current direction variability. The deep water inversion therefore includes extra steps to minimize the amplification of measurement noise, including the removal Stokes drift effects and the application of a supplementary, 2-dimensional, constrained inversion to extract wavefield measurements from the X-Band backscatter. Chapter 3 is a detailed examination of the very near surface (shallower than -4 m) current measurements made in Chapter 2. This discussion examines the reaction of inverted currents to propagating internal waves as well as to wind forcing. The vertical structure of the current estimates will then be compared to models of wind-driven current shear. Finally, concluding remarks will summarize the findings and offer suggested extensions of the current inversion technique.

Chapter 1

Inversion of Vertical Shear from X-Band Radar Observations in a River Inlet

Abstract

The influence of wave-current interactions on time series of marine X-band radar backscatter maps at the Mouth of the Columbia River (MCR) near Astoria, Oregon is examined. The energetic wave environment at the MCR, coupled with the strong tidally forced currents provides a unique test environment to explore the limitations in accurately determining the magnitude and vertical structure of upper ocean currents from wavefield measurements. Direct observation in time and space of the wave-induced radar backscatter and supporting Acoustic Doppler Current Profiler (ADCP) current measurements provide a rich data set for investigating how currents shift the observed wave dispersion relationship. First, current extraction techniques that assume a specific current-depth profile are tested against ADCP measurements. These constrained solutions prove to have inaccuracies because the models do not properly account for vertical shear. A forward solution using measured current profiles to predict the wavenumber - Doppler shift relationship for the range of ocean waves sensed by the radar is introduced. This approach confirms the ocean wavefield is affected by underlying vertical current shear. Finally, a new inversion method is developed to extract current profiles from the wavenumber-dependent Doppler shift observations. The success of inversion model is

shown to be sensitive to the range of wavenumbers spanned by observed Doppler shifts, with skill exceeding 0.8 when wavenumbers span more than 0.1 rad m^{-1}. This agreement during times of broadband observations suggests X-band backscatter is a viable means of remotely estimating current shear.

1.1 Introduction

Upper ocean currents and current shear at the air-sea boundary play important roles in the vertical mixing of entrained atmospheric gasses, advection of pollution plumes including spilled oil, and wave dynamics; in addition to influencing other navigational and scientific concerns (Phillips 1966; Halpern 1977; Davis 1981). Despite their importance, accurate in situ measurements of near surface currents remain difficult using traditional oceanographic tools due to platform motion complications and wave contamination of the current signal. Traditional point measurement current meters also lack spatial coverage (Paduan 1996). Remote sensing techniques have recently received considerable attention with the use of High Frequency (HF) radar which provides maps of ocean currents with spatial resolutions of O(1-6) km out to distances of tens of km and is used operationally around the U.S. (e.g. Terrill et al. 2006; Harlan et al. 2009; Harlan et al. 2011) . Shifting to higher frequency EM such as incoherent marine X-Band radar, offers the advantage of providing sea surface backscatter maps from a relatively large range (out to approximately 3-8 km depending on user-defined parameters and environmental conditions). This unique large spatial scale, however, makes comparison to in situ current measurements in the open ocean difficult because of potentially weak currents and the presence of horizontal current shear from eddies or current fronts (Kohut

et al. 2006; Ohlmann et al. 2007). The strong, periodic currents within the tidally forced Mouth of the Columbia River (MCR) make the region an ideal test bed for the development and validation of X-Band current estimation techniques. Furthermore, the dynamics of tidally forced river inlets are a concern for navigation, civil, and scientific communities, who will directly benefit from the ability to retrieve accurate current and current shear information remotely.

The use of radar as a tool to study wave-current interaction began with Crombie's 1955 observations of Doppler shifts using High-Frequency radar. Since then, many studies have taken advantage of the sensitivity of different types of radar to ocean wave celerity to estimate both surface current velocity as well as bathymetry (e.g. Barrick 1972; Shuchman 1979; Alpers 1981b; Young et al. 1985; Bell 1999). Readily available commercial marine X-Band provides an advantage over other radar types by offering near real-time imaging of a broad range of ocean wavelengths, ranging between approximately 20 and 200 m. The simultaneous measurement of time-space properties of the backscatter allow for exploration in the frequency-wavenumber domain. Where HF radar techniques involve direct observations of radio wave Doppler shifts, X-Band backscatter images are processed to supply a broadband wavenumber-Doppler shift relationship from which currents can be estimated.

Incoherent radars such as the one used in this study differ from coherent in that incoherent systems supply only backscatter magnitude and not the phase of the returned EM signal. Thus, a single scan from an incoherent radar supplies information about the locations, but not velocities of individual scatterers. The modulation of incoherent marine

X-Band backscatter visible in the radar imagery is a result of Bragg Scatter with centimeter-scale ocean roughness that is modified by the underlying surface gravity waves via three mechanisms: 1) hydrodynamic modulation, which, due to orbital velocities and wave-wave interactions, lead to the collection of capillary waves near the crests of longer waves, 2) shadowing by wave crests in low grazing angle geometries (typical of marine radar deployment), and 3) geometric scatter that occurs from the forward face of the ocean waves (Alpers 1981a; Nieto Borge 2004). A series of sequential backscatter images therefore captures the spatial and temporal evolution of the surface wave field, which can then be transformed into the wavenumber-frequency domain using a Fourier Transform (Young et al. 1985). Surface current information is present in the observed Doppler shift-wavenumber relationship and can be extracted using various techniques (e.g. Stewart and Joy 1974; Ha 1979; Young et al. 1985).

In previous studies, currents are extracted from wavenumber-dependent Doppler shift measurements under strict assumptions of the underlying current-depth profile shape (e.g. that currents are either depth-uniform or vary linearly with depth) (Young et al. 1985; Senet et al. 2001; Teague et al. 2001; Trizna and Xu 2006; Hessner et al. 2009). One aim of this work is to carry out a rigorous comparison of X-Band-derived currents under both uniform and linear current profile assumptions to in-situ current profile measurements. These comparisons are made over multiple tidal cycles to evaluate the success of each method in the presence of varying degrees of current shear.

There has been limited success in estimating depth-varying currents from wavefield measurements. Qualitative observations of current shear have been made using

broadband Doppler shift-wavenumber measurements (Ha 1979; Fernandez et al. 1996; Dugan 2008) by noting fluctuations in the Doppler shift-wavenumber relationships, suggesting the presence of vertical current shear. Ha (1979) attempted to use the wavenumber-dependence of Doppler shift measurements to solve for the arbitrary current-depth profile (i.e. without an assumption of its shape) using a 4-frequency HF system. This small number of discrete wavenumbers, however, did not adequately constrain the inversion, yielding noisy results. In this study the concept of extracting currents from the observed Doppler shifted dispersion relationship is extended. The ability of the X-band radar to image a broad range of ocean wavelengths is used in combination with a constrained least squares technique of the wavenumber-dense data to invert for current profiles.

1.2 Data collection

As a part of the Office of Naval Research (ONR) funded Riverine and Estuarine Transport Experiment 2 (RIVET2) field campaign, X-Band backscatter was collected at the MCR near Astoria, Oregon from 24 May 2013 to 4 June 2013. The land-based radar system was located inside the mouth at the south jetty (Figure 1.1).

Supporting current and water depth measurements were collected using a bottom-mounted Acoustic Doppler Current profiler (ADCP, 1000kHz Nortek AWAC) within the radar field of view (Figure 1.1), collecting vertical profiles of 3 dimensional currents at 15 min intervals in 0.5 m bins. The overlaid current variance ellipse, representing the depth average variances of channel and cross-channel currents, shows the currents were strongly polarized due to the channel geometry. This lead to the adoption of the

convention that current directions were limited to positive (up-channel) and negative (down-channel). The vertical structure of the stream wise current (Figure 1.2) shows strong, tidally forced currents, ranging between -3.5 and 1.3 m s^{-1}. Stronger currents occurred during ebb tides when the tidal and river forcing were aligned. The vertical current shear structure was also tidally dependent (Figure 1.3). During slack conditions, tidal forcing became small and the flow was dominated by the river forcing, resulting in slightly negative, depth uniform currents. Flood and ebb conditions, however, were dominated by strong tidal forcing and complicated salt-fresh water flow, resulting in strong current shear.

An example of a single radar scan (0800 UTC 3 June 2013) shows strong reflection from land features that illuminate the coastline, as well as the north and south jetties bounding the inlet (Figure 1.4). Each radar scan was georeferenced using known stationary points in the field of view. Backscatter from incoming waves can be seen within the inlet. Overlaid on this scan is a 750 m x 750 m box centered over the position of the ADCP, which represents the region over which data was processed to study wave-current interactions. Bathymetry contours under the inspection square (Figure 1.5) collected by the United States Geological Survey (USGS) show waves within the inspection square propagated over depths ranging between -10 and -15 m (MLLW). To capture the large spatial scale of the MCR, X-Band operating parameters (Table 1.1) were tuned to maximize the usable radar range by collecting a large number of samples (1024 samples per beam) with a range resolution of approximately 7.5 m.

Measurements of the relevant environmental conditions during the RIVET2 experiment include the wind conditions measured at the radar site and incident wave conditions collected approximately 8 km offshore by a California Data Information Program buoy (Figure 1.6a-b).

The signal strength of radar backscatter is influenced by a combination of wave height and wind conditions. A signal-to-noise ratio (SNR) was calculated by defining noise as the mean energy return in a high wavenumber, low frequency region of the backscatter spectrum, far removed from expected ocean wave information (Young et al. 1985). The evolution of the SNR for data recorded within the inspection box region demonstrates the radar signal's complicated relationship to wind and incident wave conditions approaching the MCR (Figure 1.6c). Sections of sustained high SNR correspond to times of large magnitude and near incident (North West) wind and waves.

The study of wave-current interaction is dependent on the relative angle between the current and overlying wave propagation directions. By estimating the local wave direction as the direction of the maximum SNR, the relative wave-current direction $\Delta\theta_{W-C}$ was calculated. The cosine of this angle was used as a metric of the degree to which the waves and currents are collinear (Figure 1.6d).

The 3-day time period of sustained SNR and collinear waves and currents ($\cos(\Delta\theta_{W-C} > 0.98)$) in Figure 1.6 (1200 UTC 29 May 2013 to 1200 UTC 1 June 2013) defines the time period of X-Band backscatter used for this current extraction study.

1.3 Methods

1.3.1 Doppler shift extraction

For each radar scan, backscatter within the inspection square was selected to create square subsections. 128 successive subsections (representing 3 minutes of data collection), were stacked to create a cube of data in (x,y,t), which was transform into directional wavenumber-frequency (k_x, k_y, ω) space via a 3D Fast Fourier Transform (FFT). To increase SNR, 4 subsequent FFT results were averaged. The result, therefore, represented 6 minutes of data with 8 degrees of freedom. A dispersion mask was applied to remove data separated from the zero-current dispersion line by a maximum expected current magnitude. Two examples of the azimuthally integrated results of the FFT, representative of ebb and flood current conditions (Figure 1.7a and b respectively), display the location of X-Band backscatter energy in the wavenumber magnitude - frequency domain. In the absence of currents, linear wave theory suggests waves behave according to the dispersion relationship

$$\omega^2 = \sqrt{gk \tanh(kh)} \tag{1}$$

where ω is the wave frequency, k is the wavenumber magnitude, and h is the local water depth, which was measured by the ADCP's pressure sensor.

The dominant energy during the ebb tide (Figure 1.7a) lies below the zero-current line, representing the Doppler shift effect of a strong current adverse to the wave direction, whereas during the flood (Figure 1.7b), much of the energy lies just above the zero current line, suggesting waves and currents traveling in the same direction.

However, there is also a portion of energy that appears high above the dispersion line in the higher wavenumbers (0.1 to 0.14 rad m^{-1}) during the flood tide. This energy was attributed to the first harmonic of the peak energy, which is located on the line described by the harmonic dispersion relationship for water of finite depth

$$\omega_p = (p+1)\sqrt{\frac{gk}{p+1}\tanh\left(\frac{kh}{p+1}\right)},$$

where p=0 represents the fundamental mode and p=1 represents the first harmonic (Senet et al. 2001). Harmonics in the backscatter data originate from nonlinearities in the observed wavefield, as well as nonlinearities introduced from the near-grazing imaging process of the wavefield which results in shadowing. If the observed harmonic signal were due to wave nonlinearities, the signal would be enhanced at times of maximum ebb, when oncoming currents steepen waves. However, because the observed harmonic signal appeared at flood tide, during which the grazing angle between the antenna and ocean surface decreased by an average of 15%, the harmonics were most likely caused by the nonlinearities in the imaging process when waves shadowed the radar signal. This signal, therefore, contained no additional exploitable Doppler shift information and was removed. To eliminate this signal from the wavenumber-frequency domain, energy that introduced large discontinuities (>0.1 rad s^{-1}) in the frequency-wavenumber profile was isolated and removed.

The remaining ridge of energy in the wavenumber-frequency domain was isolated, and wavenumber-dependent Doppler shifts were calculated by subtracting the dispersive frequency (1) from the observed frequency.

Young et al. (1985) developed a method of current extraction from X-Band radar using the Doppler shift expression

$$\Delta\omega(k) = \mathbf{k} \cdot \mathbf{u}_{\mathbf{eff}}(k) = k u_{eff}(k) \cos(\Delta\theta_{C-W}) \tag{2}$$

where $\Delta\omega$ is the Doppler shift, and $\mathbf{k}$ is the wavenumber vector. $\mathbf{u}_{\mathbf{eff}}(k)$ is the 2-D *effective current velocity* vector that is wavenumber-dependent, which represents a weighted depth-average effect currents have on the wavefield (Stewart and Joy 1974). The scalar product in (2) implies that waves are Doppler shifted only by current components collinear with the wave propagation (Phillips 1966). For this study, because of polarized currents (Figure 1.1) and waves (Figure 1.6d) within the inspection square, the vector quantities $\mathbf{k}$ and $\mathbf{u}_{\mathbf{eff}}$ were replaced with the channel direction magnitudes k and u_{eff}. Because a time period was selected such that $\cos(\Delta\theta_{C-W}) > 0.98$, the error introduced by this simplification into the Doppler shift calculation was less than 2% .

The relationship between the wavenumber-dependent effective velocity $u_{eff}(k)$ and the depth-varying current $u(z)$ was first derived by Stewart and Joy (1974) in deep water (i.e. $kh \to \infty$) and then expanded to account for finite depth effects by Kirby and Chen (1989). The finite depth relationship is

$$u_{eff}(k) = \frac{\Delta\omega}{k} = \frac{2k}{\sinh(2kh)} \int_h^0 u(z) \cosh\left[2k(h+z)\right] dz \tag{3}$$

The weighting function within the integral indicates that Doppler shifts of all wavenumbers are heavily influenced by near surface currents.

1.3.2. Depth-Uniform and Linear Current Estimation

If the currents affecting the wavefield are depth uniform, or $u(z) = u_0$, the evaluation of (3) shows that the effective velocity is independent of wavenumber, and $u_{eff} = u_0$. This simplification reduces (2) into the linear expression

$$\Delta\omega = ku_0 \tag{4}$$

which implies that depth uniform currents can be estimated with a linear fit of observed Doppler shift-wavenumber profiles. Because u_0 is wavenumber independent, it describes the bulk effect underlying currents have on the wavefield. u_0 is therefore referred to as the *velocity of encounter* or *bulk current velocity* (e.g. Dankert and Rosental 2004). In an example from data collected on 0520 UTC 31 May 2013 (Figure 1.6), a linear regression of the Doppler shift - wavenumber observations during the maximum ebb current had a slope of -1.9 m s^{-1}, which defines an estimate of the bulk current magnitude for this time period. This linear regression technique to calculate bulk currents was repeated throughout the 3-day time period, and results were compared with depth-averaged ADCP current velocities.

In the presence of depth-varying currents, the effective velocity remains wavenumber-dependent. Previous studies carried out in deep water have estimated depth-varying currents from Doppler shift measurements by assuming that the currents vary linearly with depth (e.g. Stewart and Joy 1974; Ha 1979; Young et al. 1985). Evaluating (3) with a linear current profile yields

$$u_{eff}(k) = u\left(z = -\frac{1}{2k}\tanh(kh)\right) \tag{5}$$

which implies that the observed effective velocity at wavenumber k is equal to the geophysical current velocity at a depth of $z = -(2k)^{-1}\tanh(kh)$. The expression in (5) was used to map observed effective velocities to estimate current-depth profiles, which were compared to ADCP current profile measurements over the selected 3-day time period.

The strong, depth-dependent current shear measured by the ADCP (Figure 1.3) suggests that accuracy of radar-derived current estimates would be enhanced by removing assumptions of the current-depth structure. To account for the effects of arbitrary current profiles on the wavefield, the integral equation (3) can be used in either the "forward" or the "inverse" problem. The forward problem involves transforming measured current profiles (e.g. from an ADCP) into Doppler shift-wavenumber profiles for comparison with X-Band observations. The inverse problem is the extraction of current profiles from X-Band measurements of wavenumber-dependent Doppler shifts.

1.3.3 The Forward Problem

To transform the discrete ADCP current-depth profiles into Doppler shift-wavenumber profiles, (3) was discretized to match the ADCP measurement interval. The resulting finite sum is

$$u_{eff}(k_j) = \frac{\Delta\omega_j}{k_j} \approx \frac{2k_j}{\sinh(2k_j h)} \sum_{i=1}^{m} u_i \cosh\left[2k_j(h+z_i)\right]\Delta z\ , \tag{6}$$

where there are m depth bins of size Δz, and h is the measured water depth. The sum was evaluated using ADCP current measurements for each k_j measured by the X-Band to build a Doppler shift-wavenumber profile for each time to be directly compared to those observed by the radar.

1.3.4 The Inverse Problem

The inverse problem involves extracting current profiles $u(z)$ from the Doppler shift-wavenumber observations using (3). The inversions of Laplace-type expressions, such as this, are plagued by the amplification of inherent measurement noise and truncation error (Ha 1979). Two methods were used in this study to stabilize the inversion: 1) the Gauss-Legendre method was applied to reduce the integral to quadrature (Weeks 1966; Cohen 2007) and 2) a constrained least squares approach was used to invert the resulting matrix expression (Twomey 1977; Wunsch 1996).

Gauss-Legendre quadrature suggests that an integral can be approximated by the finite sum

$$\int_{-1}^{1} f(x)dx \approx \sum_{i=1}^{n} f(x_i)w_i \tag{7}$$

where x_i and w_i are the quadrature points and weights, respectively, which are chosen by requiring that (7) be satisfied exactly for any polynomial with order $m<n$-1 (Golub 1969). The orthogonal polynomials for which this condition holds are the Legendre polynomials, where x_i are their zeros and w_i are weights, both of which are well tabulated (e.g. Cohen

2007). To reduce (3) to the quadrature form in (7), first the substitution $x=1+2zh^{-1}$ is made. The integral expression becomes

$$\frac{u_{eff}(k)\sinh(2kh)}{kh} = \int_{-1}^{1} \cosh\left[2k(h+z(x)\right]u\left[z(x)\right]dx\,,$$

where

$$z(x) = \frac{h}{2}(x-1)\,.$$

Using (7), the quadrature form becomes

$$\frac{u_{eff}(k_j)\sinh(2k_jh)}{k_jh} \approx \sum_{i=1}^{n} \cosh\left[2k_j(h+z_i)\right]u_i w_i$$

where $z_i = \frac{h}{2}(x_i - 1)$ and n is Legendre polynomial order. This sum can be rewritten as the matrix equation

$$d = \mathbf{G}u\,,$$

where

$$d_j = \frac{u_{eff}(k_j)\sinh(2k_jh)}{k_jh}$$

$$G_{ij} = \cosh\left\lfloor 2k_j\,(h+z_i)\,\right\rfloor w_i$$

$$u = u(z_i)\,.$$

In this way, the model is now in a form that can be solved using least squares techniques, which minimize the model misfit $\mathbf{G}u$-d with respect to u. The number of discrete solutions is defined by the order of the Legendre polynomial, n, which is adjustable to minimize noise amplification. To further stabilize the inversion, the curvature of the resulting current profiles was constrained using a model-weighting matrix. Using the Taylor series expansion of $\mathbf{u}(z)$, the second derivative can be approximated as

$$\frac{\partial^2 u_i}{\partial z^2} \approx \frac{u_{i-1} - 2u_i + u_{i+1}}{\Delta z_i^2}$$

or in matrix form,

$$\frac{\partial^2 u}{\partial z^2} \approx \frac{1}{\Delta z^2}\begin{bmatrix} 1 & -1 & 0 & 0 & 0 & \\ 1 & -2 & 1 & 0 & 0 & \cdots \\ 0 & 1 & -2 & 1 & 0 & \\ 0 & 0 & 1 & -2 & 1 & \\ & & \vdots & & & \ddots \end{bmatrix} u = \mathbf{C}u$$

Minimizing both the misfit and the new model weighting matrix with respect to u results in the constrained least squares solution

$$u = \left[\mathbf{G}^T\mathbf{G} + \lambda(\mathbf{C}^T\mathbf{C})\right]^{-1}\mathbf{G}^T d \tag{8}$$

(Twomey 1977) where λ is a tunable parameter defining the extent to which the result is constrained by $\mathbf{C}$. The Legendre order n and the adjustable parameter λ were tuned by inverting the results of the forward problem and comparing with the original ADCP current profile measurements. The tuned model was then applied to invert current profiles from X-Band wavefield measurements.

Model skill was used as the error metric to quantify the comparison between estimated currents from the X-Band inversion and those measured by the ADCP. The definition of model skill (Bogden 1996; Hetland 2006) is

$$skill = 1 - \frac{< (u_{adcp} - u_{XBand})^2 >}{< u_{adcp}{}^2 >}, \tag{9}$$

where angle brackets denote an average (in time or depth). Zero misfit between ADCP and inverted currents results in a maximum skill of 1, whereas large inverted currents that disagree with ADCP observation can yield a negative skill. One advantage of model skill is the normalization of error during times of low signal. Another advantage of the skill metric is that is a single number representing the evaluation of either depth or temporally averaged inversion results. For this study, model skill was used to evaluate the success of current inversions in both time and depth.

1.4 Results

1.4.1 Depth-Uniform and Linear Current Estimation

Currents were estimated under the depth-uniform current assumption using the linear regression in (4) over the selected 3-day time period. These results were compared to depth-averaged ADCP currents (Figure 1.9). Time periods of missing X-Band data correspond to low SNR, for example due to low wind speed (below 3 ms^{-1}) (Figure 1.6c). The time series shows the agreement was good during slack tides, but reduced as the currents reached flood and ebb conditions (Figure 1.9a). The scatter plot shows the best agreement occurred when the depth-averaged current was between -0.25 m s^{-1} and -0.5 m

s^{-1}, corresponding to times when the current was dominated by the river outflow (Figure 1.9b).

Current profiles were estimated under the linear current-depth assumption using (5) and the results were compared with ADCP measurements (Figure 1.10). Because solutions from this method only exist at depths defined by the effective depth $z = -(2k)^{-1}\tanh(kh)$, the current profile estimates were constrained to a narrow range of depths, between -2.5 and -4.75 m.

1.4.2 The forward problem

To compute the forward problem, the weighted sum in (6) was used to transform ADCP current measurements to Doppler-shift wavenumber profiles. The results were then directly comparable to X-Band Doppler shift observations (Figure 1.11). Missing X-Band data in the higher wavenumbers during flood tides was due to the presence of the harmonics, which overwhelmed the fundamental signal (e.g. Figure 1.7). Results from the forward problem qualitatively agree with X-Band profiles over the 3-day time period, exhibiting similar structure in the wavenumber-dependence of the observed Doppler shifts.

To quantitatively compare the forward problem and X-Band Doppler shift profiles (Figure 1.11 b and c), the average slope of each $\Delta\omega(k)$ profile were compared (Figure 1.12). Good agreement between X-Band and forward problem average slopes show that the wavefield observations and current measurements are accurately related through the model developed by Kirby and Chen (1989). Because estimating the average slope of

$\Delta\omega(k)$ profiles is similar to using (2) to estimate depth-uniform currents, depth-averaged ADCP currents were overlaid on the average slope comparison. If the observed currents were depth uniform, the slopes of the forward problem results would be the same as the depth-averaged currents. Discrepancy between the two, therefore, implies the presence of current shear has a significant effect on the Doppler shift-wavenumber relationship.

1.4.3 The Inverse Problem

1.4.3a MODEL TUNING

The Doppler shift-wavenumber profiles from the forward problem were used as input into (8) to tune the inversion method. The Legendre polynomial order and the tunable parameter λ were varied , until the best match with the measured ADCP current profiles was found (Figure 1.13), which occurred with n=7 and λ=*0.04*.

1.4.3b INVERSION OF X-BAND BACKSCATTER

The tuned inversion model (8) was used to estimate current profiles from the X-Band $\Delta\omega(k)$ profiles (Figure 1.14a). Current profiles range from the river bed to the surface, whereas ADCP current measurements (Figure 1.14b) are limited to a smaller depth range (indicated by black lines in Figure 1.14a) due to instrument mounting height and surface contamination. The vertical structure of the inverted currents compares well with ADCP structure qualitatively, showing the complicated exchange between tidal forcing and river outflow through tidal evolutions. (9) was used to calculate the skill of the inversion result as a function of time (Figure 1.14c). With skill exceeding 0.8, the inversion model shows good results during ebb and slack current conditions. However,

the skill drops below zero during flood currents, when $\Delta\omega(k)$ are truncated due to harmonic contamination. The depth-dependence of skill was calculated during ebb and slack conditions (Figure 1.15), showing that inverted currents agree well with ADCP currents from the surface (*skill*>0.8) to 9 m, where skill falls below 0.7.

1.5 Discussion

Results of the depth-uniform analysis show that error in currents estimated under the depth-uniform assumption exceeded 20% within one hour of slack currents (Figure 1.9). This confirmed that the presence of current shear plays an important role in estimating currents from wavefield measurements. The simplest way to include the effects of current shear was to assume a linear depth-current relationship, which resulted in a model to directly map effective velocities of individual wavenumbers to currents of unique effective depths (Figure 1.10). Although current estimates appeared to capture some evidence of current shear, solutions were limited to a small depth range of approximately 2.5 m. Furthermore, because of the direct mapping between individual wavenumbers to individual water depths, noisy or missing data and truncated Doppler shift data led to discontinuous and truncated current-depth profiles. Because of the small depth range and inconsistency of the current estimates, a more rigorous solution involving the entire depth-current profile was sought after.

The forward problem investigated the sensitivity of the wavefield to the arbitrary current profile shapes measured by the ADCP. The Doppler shift-wavenumber profiles resulting from the forward problem compared will with those observed by the X-Band

(Figure 1.11 and Figure 1.12), implying that the model developed by Kirby and Chen (1989) appropriately describes the observed wave-current relationship in the MCR. Furthermore, the result of the forward problem shows that the observed current shear significantly altered the Doppler shift-wavenumber relationship, suggesting that the retrieval of current shear information from Doppler shift measurements is possible. A method was therefore developed to calculate the inversion of the model used in the forward problem. Free parameters were tuned by forcing the inversion of the forward problem results to match ADCP current profiles (Figure 1.13). Residual error between the two was partially due to error in the forward problem, which arose from the truncation of ADCP profiles near the river bed (due to instrument mounting and blanking range) as well as below the surface (to avoid surface contamination).

The inversion method resulted in current estimates, which successfully captured the evolution of the current profile throughout multiple tidal cycles in the MCR, with model skill exceeding 0.8 during ebb and slack current conditions (Figure 1.14). The drop in model skill during flood tides (Figure 1.14c), when harmonic contamination resulted in a narrower usable wavenumber range, shows the success of the inversion was dependent on broadband Doppler shift observations. The depth dependence of skill (Figure 1.15) shows agreement between inverted and measured currents were best in the top 9 m of the ADCP range. The skill of current estimates below -10 m declined rapidly as waves within the observed wavenumber range were less sensitive to deeper currents as indicated by (3).

One source of error in the results of the inversion was the bathymetric variation under the inspection square (Figure 1.5). The range of bathymetry-induced Doppler shifts

caused the “smearing” of energy in the wavenumber-frequency space (e.g. Figure 1.7), which led to uncertainty in the Doppler shift estimation.

Water depth uncertainty contributed to error in the calculation of Doppler shifts as well as in the process of inverting the Doppler shifts to estimate currents. To examine the effects of error in water level on each of these parts of the inversion method separately, the water level was varied by ± 2 m first before, and then after Doppler shifts were estimated (Figure 1.16). By varying the water level before Doppler shifts were estimated, model skill was affected by the error in the wavefield measurements (i.e. the dispersion relationship (1)) and the inversion process (8). By varying the water level after Doppler shifts were calculated, the wavefield measurements were assumed to be accurate and variations in model skill only reflected the sensitivity of the inversion model to water level. Water level error in the dispersion relationship calculations resulted in much higher sensitivity to water level, with model skill falling to 0 when water depth was altered by +1.5 m. Depth error in the inversion process alone, however, lead to skill variations of less than 0.1 over depth variations between ± 2 m. The maximum skill at a depth offset of 0 m confirms that there was no bias in the water level used for current inversions in this study.

Both the time and depth dependence of skill suggest that results of this study could be improved by expanding the wavenumber range used in the inversion. Raising the antenna height, for example, would minimize wave shadowing and therefore avoid the harmonic contamination during flood tides. Increasing the range resolution of the radar backscatter measurements would extend the Nyquist wavenumber cutoff by

sampling smaller waves. Increasing the size of the inspection square would result in a smaller low wavenumber cutoff, potentially increasing the inversion skill below -10 m depth. However, a larger inspection area would be sensitive to a larger range of water depths, resulting in more uncertainty in Doppler shift estimation.

The accuracy of Doppler shift estimates depends on the time window of the FFT to exceed the wavefield's decorrelation time scale. At a minimum one should ensure that time windows capture multiple wave periods of the longest measurable wave. However, increasing the FFT time window to sample multiple wave groups would ensure the maximum energy in each frequency band is observed, increasing the SNR. A potential improvement to the inversion example shown in this study, therefore, is to explore the effect of much longer time windows to sample across several time scales across which wave groups pass.

The success of future applications of the current inversion method will rely on both the presence and the ability to observe a broad-banded wavefield. Wavefields comprised only of short waves are largely unaffected by deeper currents, limiting the depth range of inversion results. Conversely, the inversion of wavefield measurements that contain only low wavenumber information will limit the ability to resolve near surface currents.

1.6 Conclusion

In this work, X-Band backscatter was collected in the Mouth of the Columbia River, Oregon to investigate the validity of current and current shear estimations from

Doppler shift measurements. Although the well-established method that assumes uniform depth-current profiles provided reasonable current estimates during times of low shear, discrepancies exceed 20% within 1 hour of slack tide. The estimation of current profiles under a linear depth-current profile assumption was shown to be limited to a depth range of approximately 2.5 m, and be sensitive to observation noise. Through the use of the integral transform (Kirby and Chen 1989) that takes current shear into account, ADCP current profiles were transformed into Doppler shift-wavenumber profiles for comparison with X-Band observations. The agreement between ADCP and X-Band observations was improved by the inclusion of the observed current shear information. This result indicated the X-Band observations of the wavefield contained information about the underlying current shear, which should be taken into account when estimating currents from Doppler shift observations.

A new inversion model to estimate current-depth profiles from X-Band observations of the wavefield's Doppler shift-wavenumber relationship was introduced. Applying the model to estimate current profiles in the MCR showed good agreement to concurrent ADCP measurements, with a model skill exceeding 0.8 during ebb and slack current conditions. X-Band-derived results were shown to be accurately depict depth and time variable phenomena such as the tidally forced countercurrent at depth during tidal transition. The ability to remotely sense such phenomena suggest this new model can be used to address many types of near-shore scientific, navigational and civil concerns. To support studies of open ocean currents on the submesoscale, future work can expand this inversion method to be applicable for use in deep-water environments. Expansion to the

open ocean introduces geometric complications, with relative directions of waves of various wavenumbers and currents of various depths becoming important. Furthermore, smaller current magnitudes may make it more difficult to extract Doppler shift-wavenumber profiles in poor SNR environments.

Acknowledgments

The authors would like to thank ONR for funding support and collaborators Dr. Rocky Geyer and Dr. Peter Traykovski at WHOI for the ADCP measurements. We would also like to thank USACE for CDIP buoy data support and USGS for the bathymetric survey data. Chapters 1, in full, has been submitted to *the Journal of Atmospheric and Oceanic Technology* in 2015. Campana, Jeffrey; de Paolo, Anthony; Terrill, Eric J., Inversion of Vertical Shear from X-Band Observations in a River Inlet. The dissertation author was the primary investigator and author of this paper.

Table 1.1 – Operational parameters for the land-based X-Band radar during the RIVET2 campaign that collected data from 24 May 2013 to 4 June 2013.

RIVET2 X-Band Collection Parameters	
Radar Type	Furuno 2117bb
Peak Output Power	12 kW
Antenna Length	8 ft
Beam Width	0.95^{o} (Horizontal) 20^{o} (Vertical)
Radar Scan Rate	42 rpm
Range Resolution	7.5 m
Maximum Range	~8 km
Radio Wave Frequency	9410 +/- 30 MHz
Bragg Scatterer Wavelength	3.2 cm
Antenna Height	16-20 m
ADC resolution	12 bit

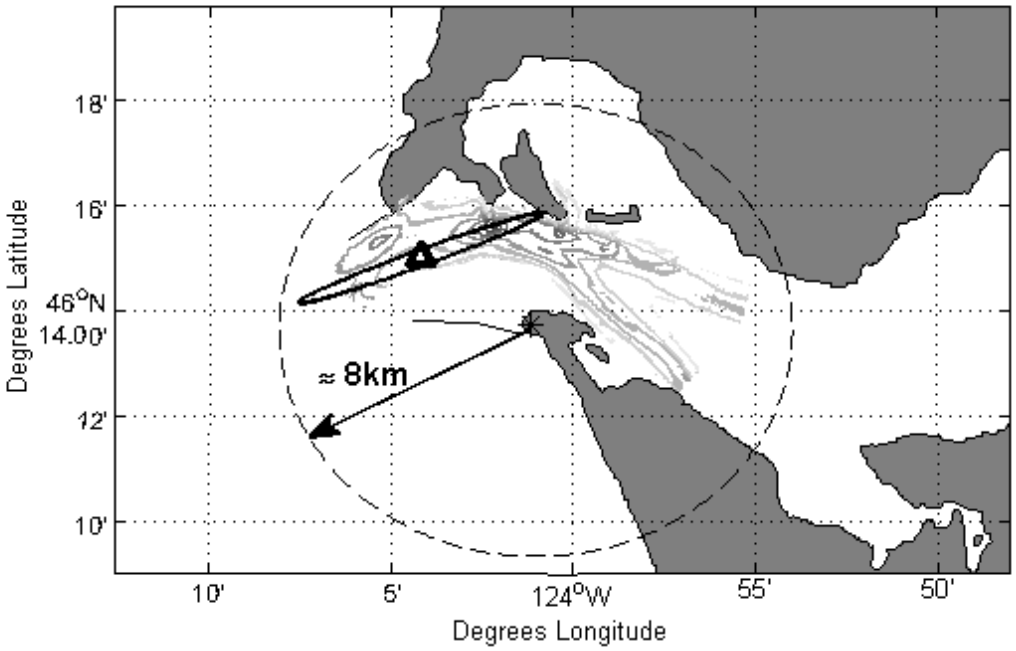

Figure 1.1 – A map of the Columbia River Mouth, where grey is land and white is water. Light gray countours show bathymetry collected by USGS surveys.The dashed circle denotes the approximate maximum range of the X-Band radar and the triangle indicates the location of a bottom mounted ADCP. The variance ellipse of the depth-averaged currents during RIVET2 is shown in black.

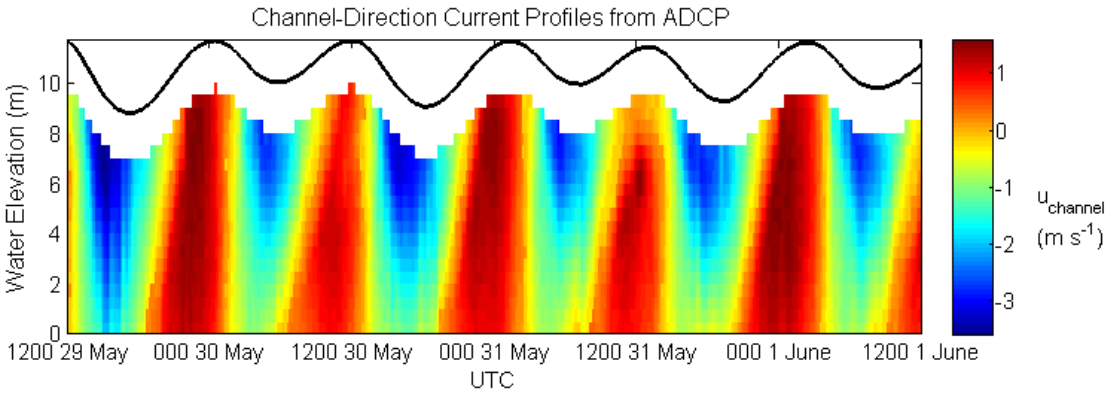

Figure 1.2 – ADCP measurements of the tidally forced currents over a 3 day period. Warm colors indicate up-river flow and cool colors indicate down-river flow.

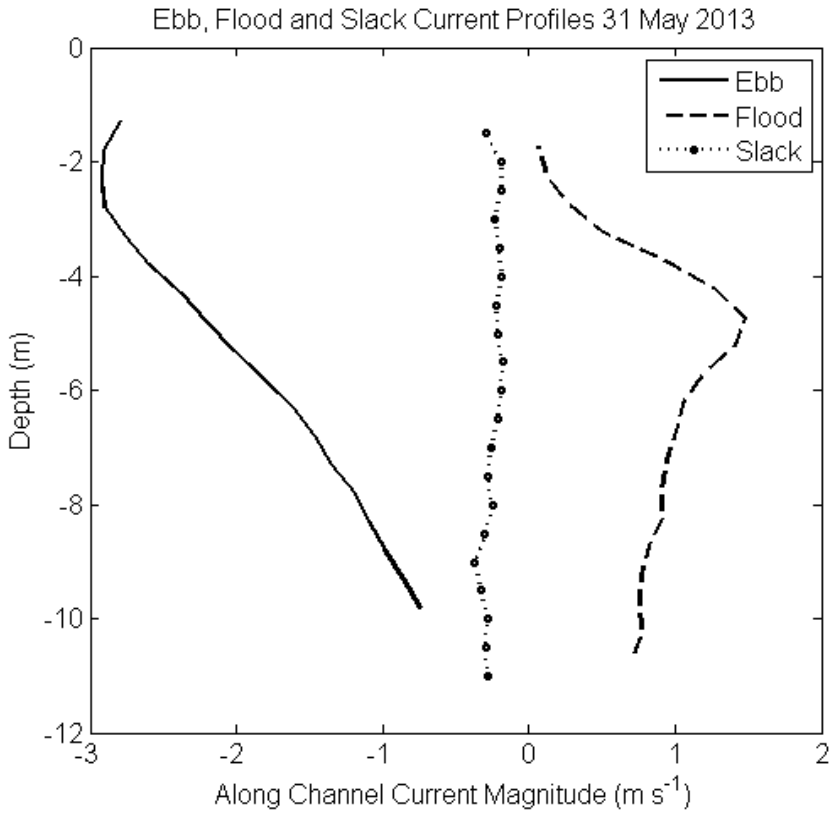

Figure 1.3 – Ebb, Flood and Slack current profiles measured by the ADCP on 31 May 2013.

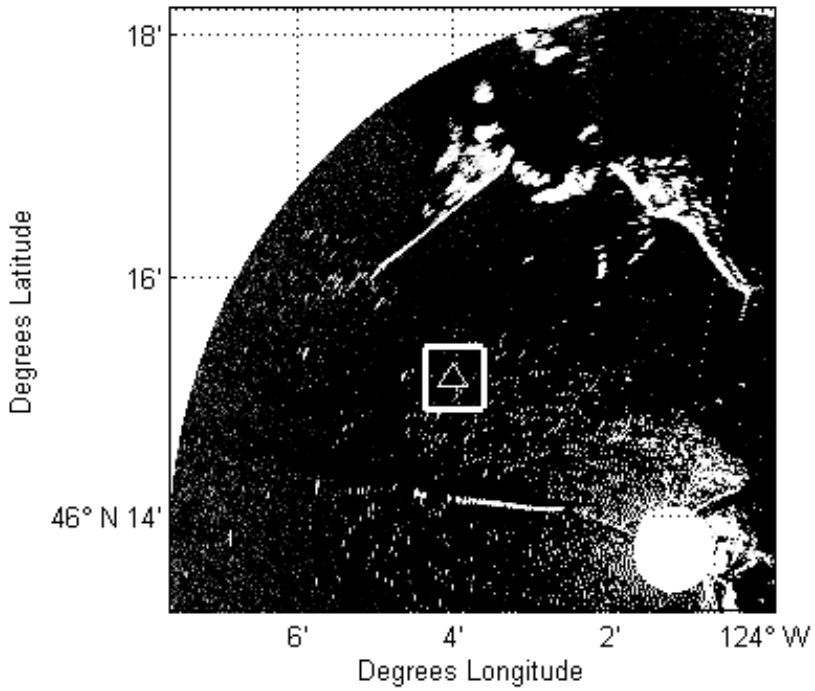

Figure 1.4- A section of a single X-Band scan of the MCR, where light and dark shading represent high and low signal return respectively.The radar is located in the middle of the white disk in the lower right, which denotes the 500 m blanking range. The study region (white square) is centered over the bottom mounted ADCP (triangle).

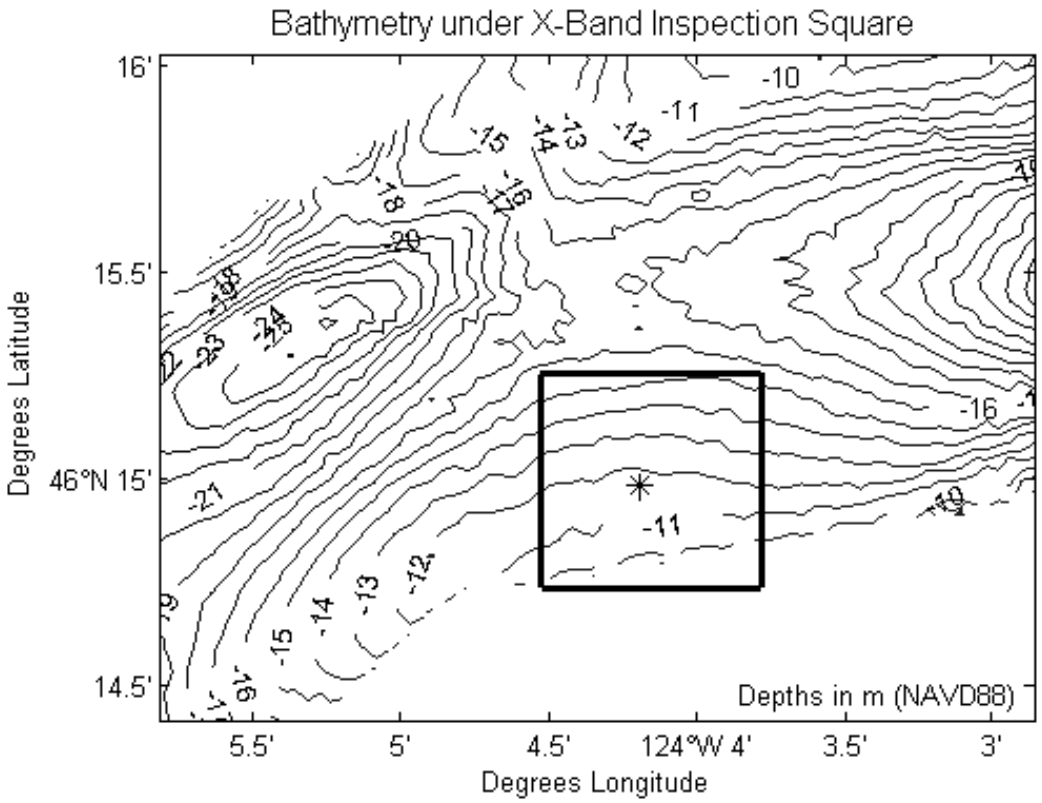

Figure 1.5 – Bathymetry (MLLW) from USSG surveys shows that water depth under the inspection square varies between -10 m and -15 m. The ADCP (asterisk) was mounted at a depth of -11 m.

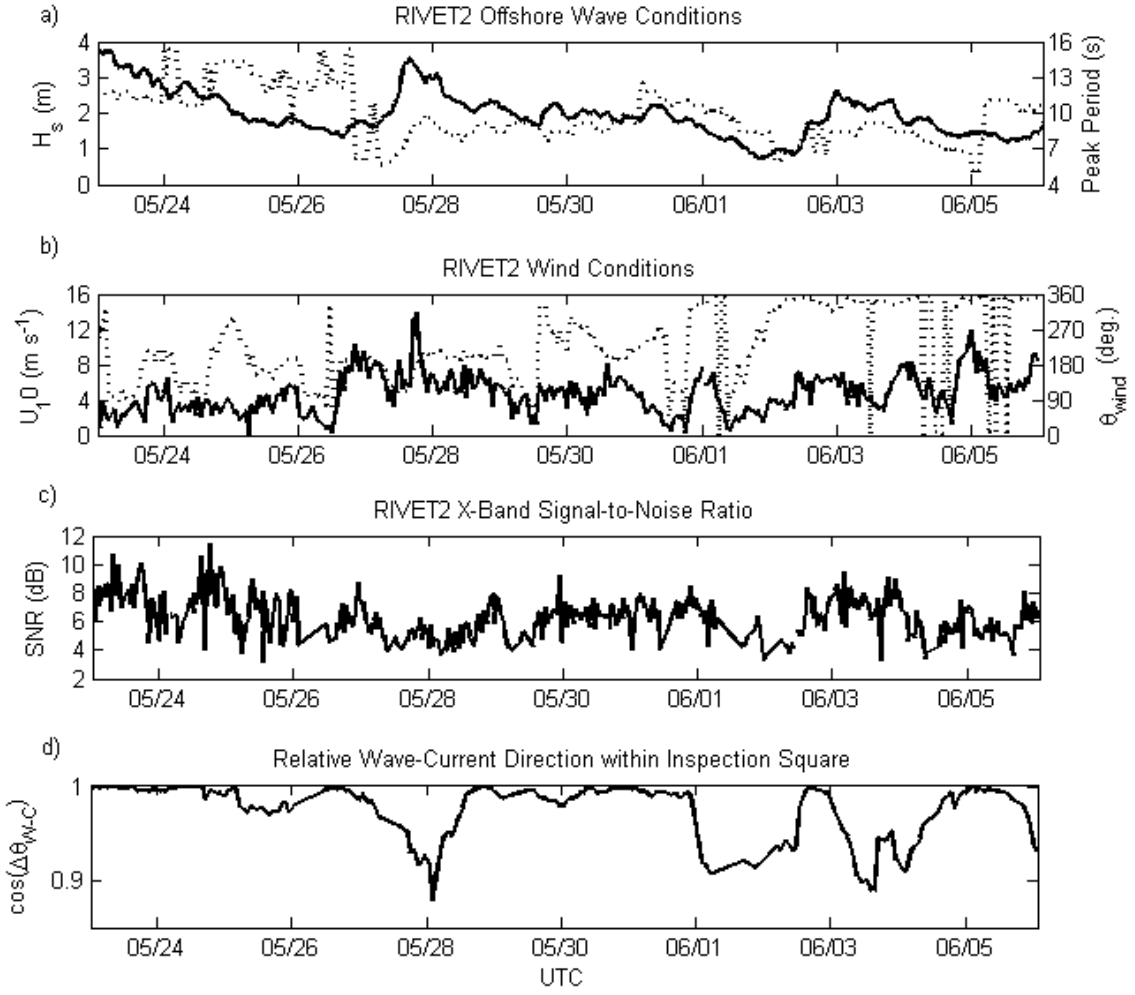

Figure 1.6 – Environmental conditions data collected at MCR near Astoria, Oregon, including (a) offshore wave conditions and (b) wind conditions at the radar site. (c) The X-Band Signal-to-Noise ratio, resulting from the wave and wind conditions. (d) Relative wave-current direction displayed as the cosine of the absolute difference between wave and current directions, $\Delta\theta_{W\text{-}C}$. This study focuses on the time period of sustained SNR and small $\Delta\theta_{W\text{-}C}$ from 30 May to 1 June.

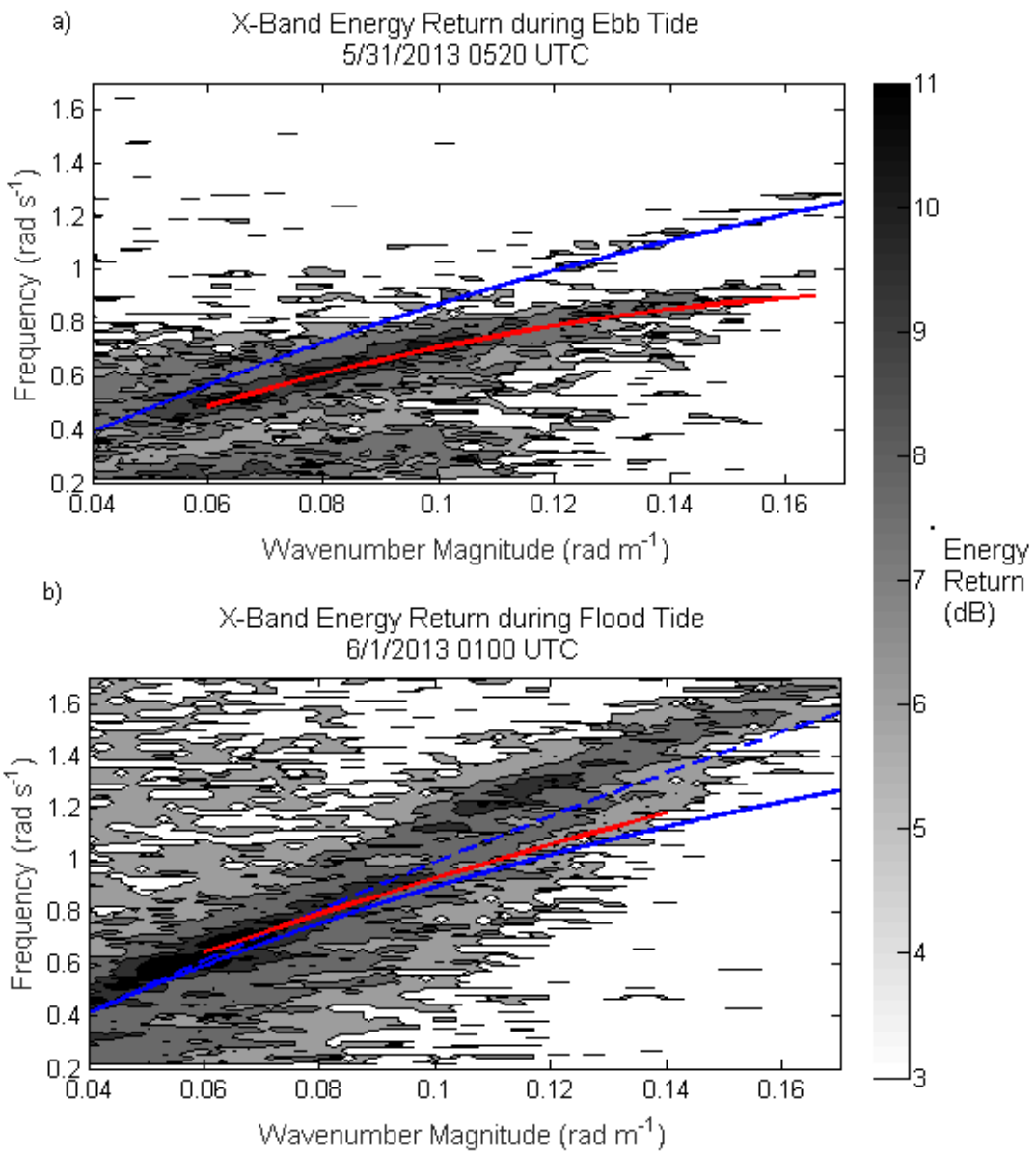

Figure 1.7 – Examples of the location of returned backscatter energy in wavenumber-frequency space during (a) ebb and (b) flood current conditions. Darker colors indicate higher energy return than lighter colors. The depth-corrected dispersion relationship (solid blue) and 1st harmonic relationship (dashed blue) indicate expected energy locations in the zero-current condition. The solid red line denotes selected $\Delta\omega(k)$ profiles for current estimation.

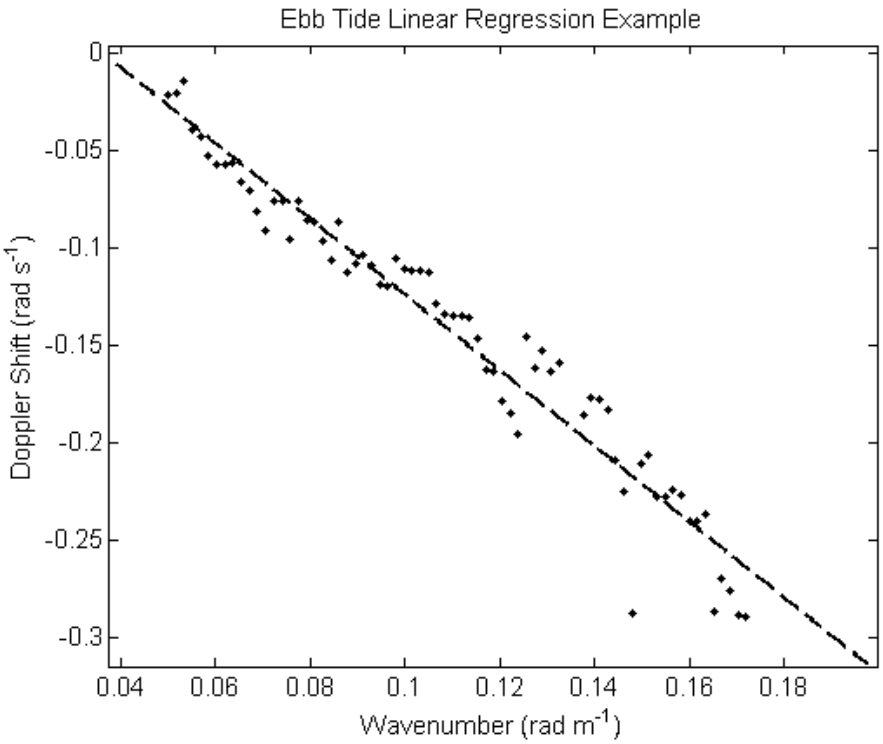

Figure 1.8 – An example of a linear fit to Doppler shift observations, where the -1.9 m s^{-1} slope represents an estimate of a depth-uniform current. These data were selected during an ebb tide at 0520 31 May 2013.

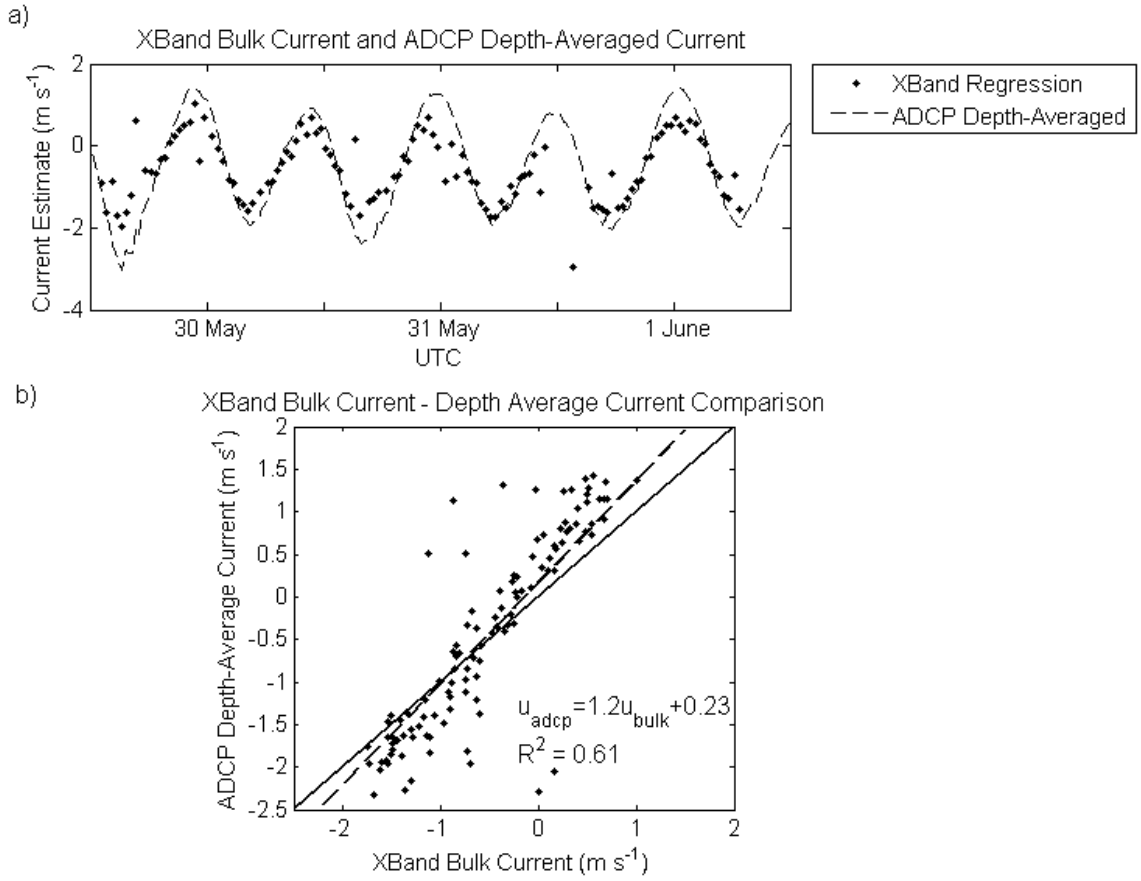

Figure 1.9 – (a) ADCP depth-averaged currents (dashed) and X-Band bulk current estimates (dotted) versus time for the 3 day period. (b) Scatter plot of X-Band bulk currents versus ADCP depth-averaged currents. Solid line indicates 1-to-1 relationship and dashed line denotes linear fit.

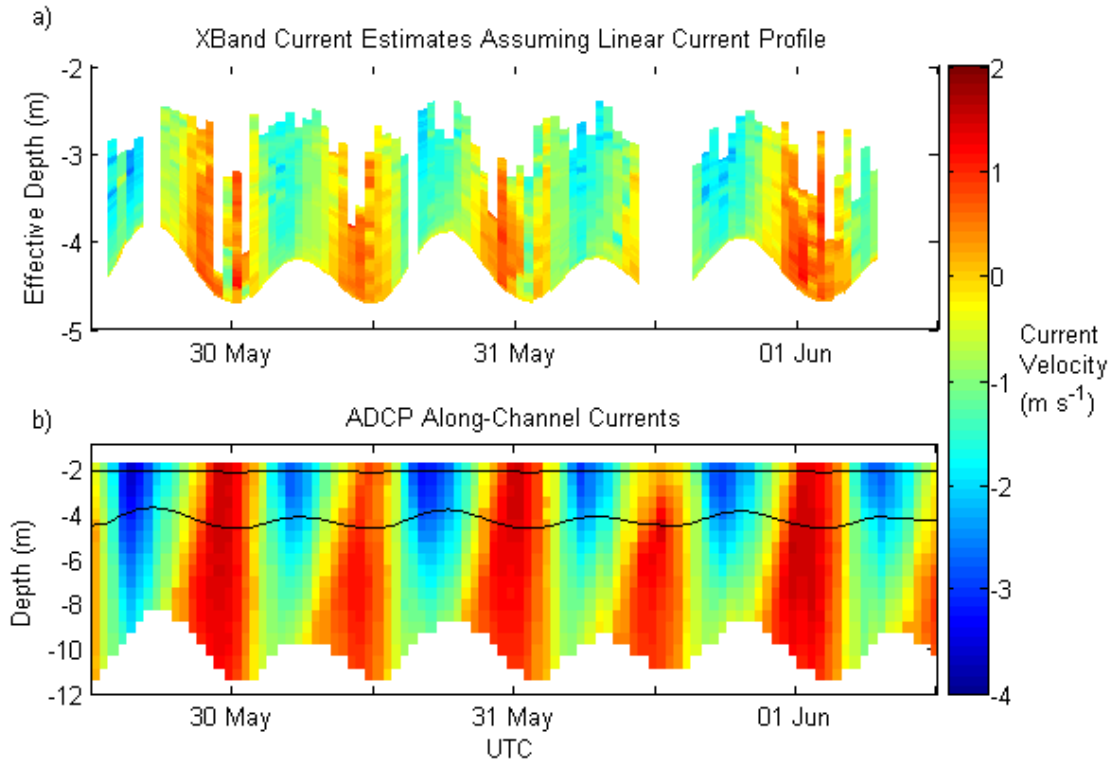

Figure 1.10 – a) X-Band-derived current profiles assuming a linear curent-depth relationship, or $u_{eff}(\tanh(kh)/(2k) = u(z)$. b) ADCP depth-current profile measurements in the along-channel direction. Black lines bound the region in which X-Band-derived currents are constrained by the range of observed wavenumbers.

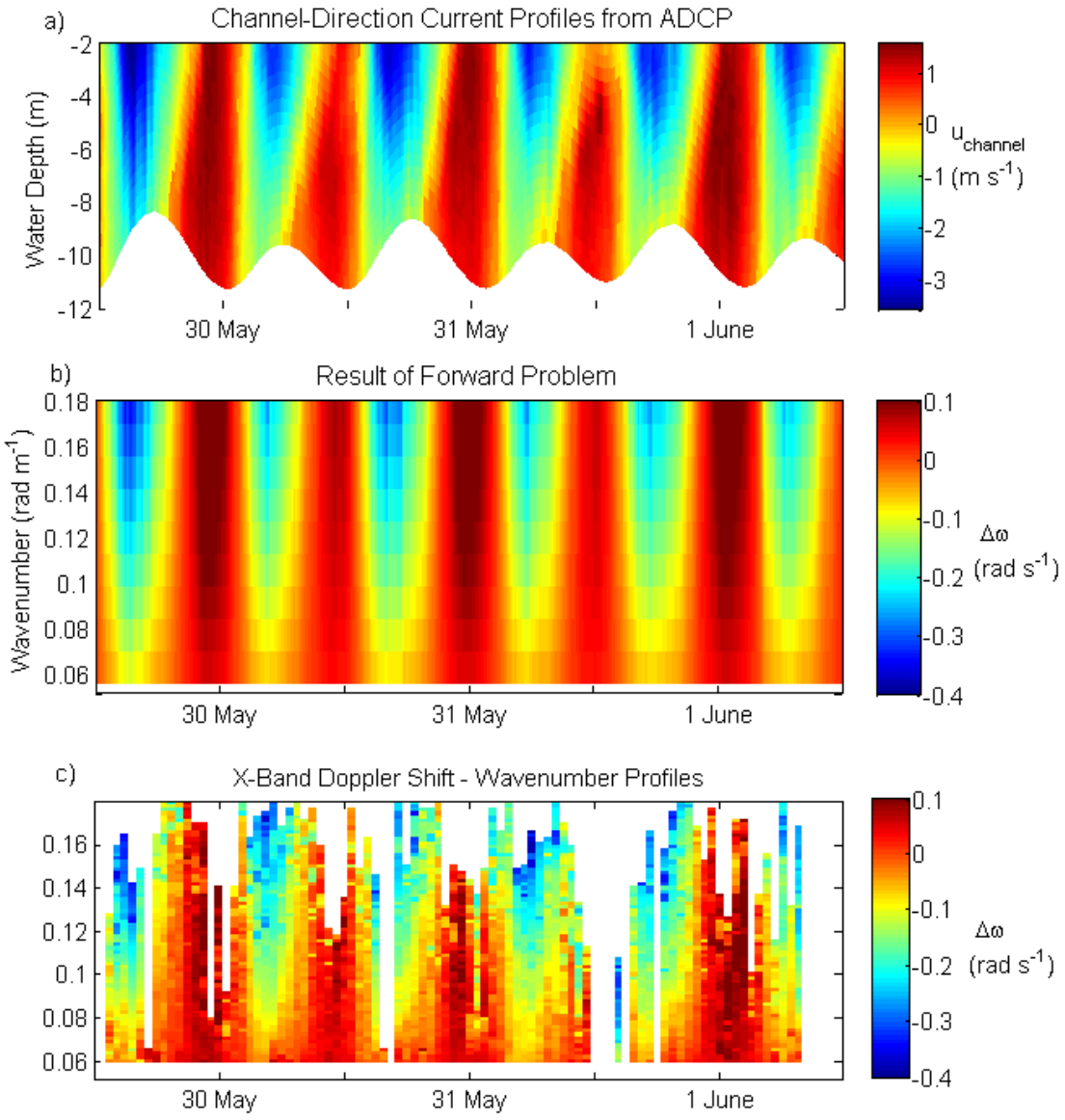

Figure 1.11 – a) ADCP depth-current profile measurements. b) The Doppler shift-wavenumber profiles resulting from transforming the ADCP current profiles via the forward problem. c)Observed X-Band Doppler shift-wavenumber profiles.

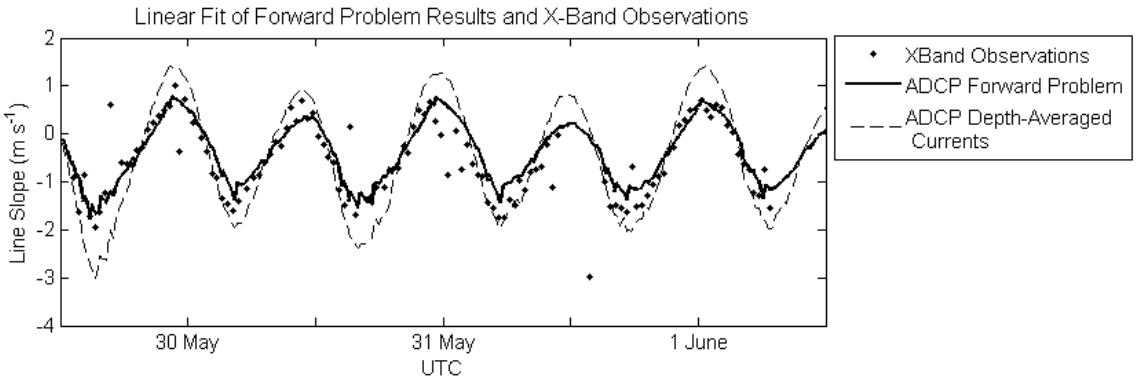

Figure 1.12 – Time series of the slopes of the $\Delta\omega(k)$ profiles from X-Band observations (dotted) and the forward problem (solid). Dashed line indicates ADCP depth-averaged currents.

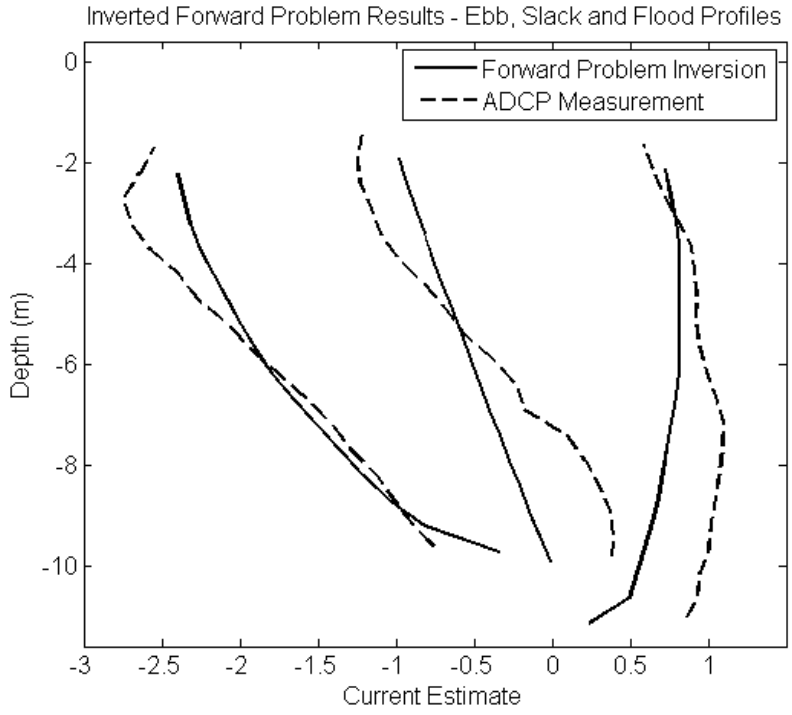

Figure 1.13 – The outcome of inverting the forward problem result (solid) is compared to measured current profiles (dashed) to tune the inversion method. In this example, Legendre order n=7 and λ=0.01 .

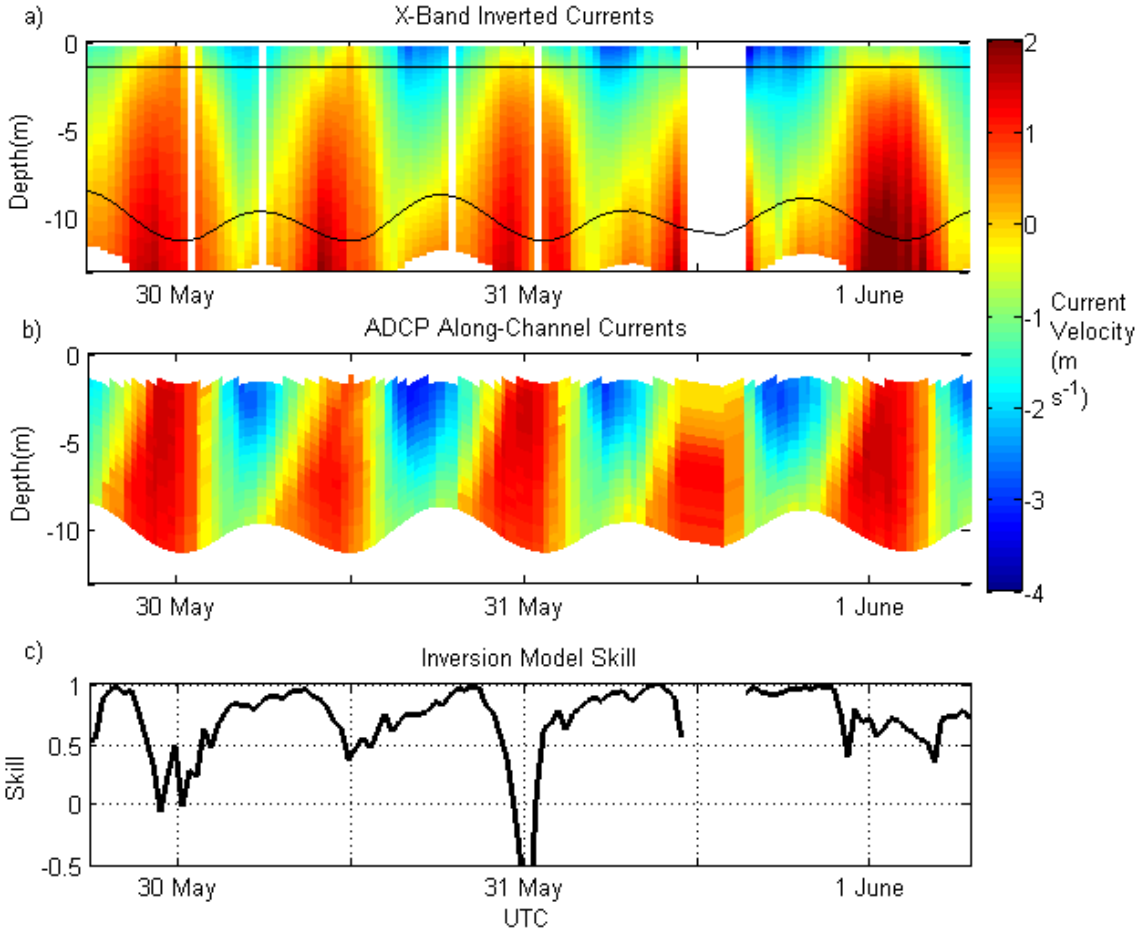

Figure 1.14 – (a) The result of the inversion of current profiles from X-Band backscatter. Black lines bound the region measured by the ADCP. (b) ADCP current measurements in the along-channel direction. (c) Time series of the skill of the X-Band inversion method.

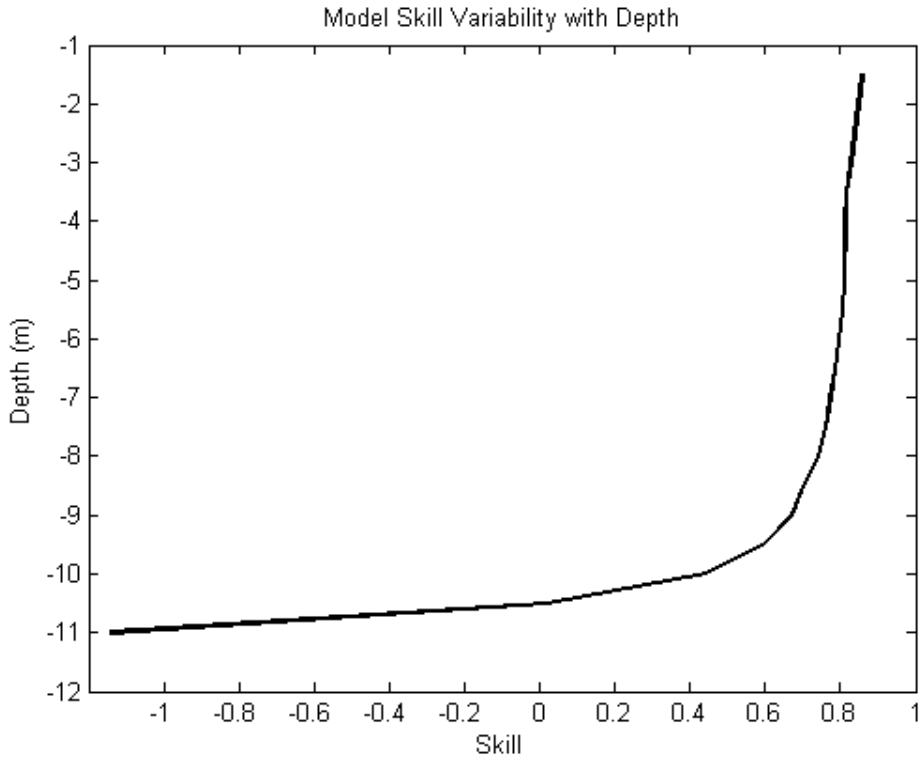

Figure 1.15 – The depth dependence of the skill of the X-Band inversion method.

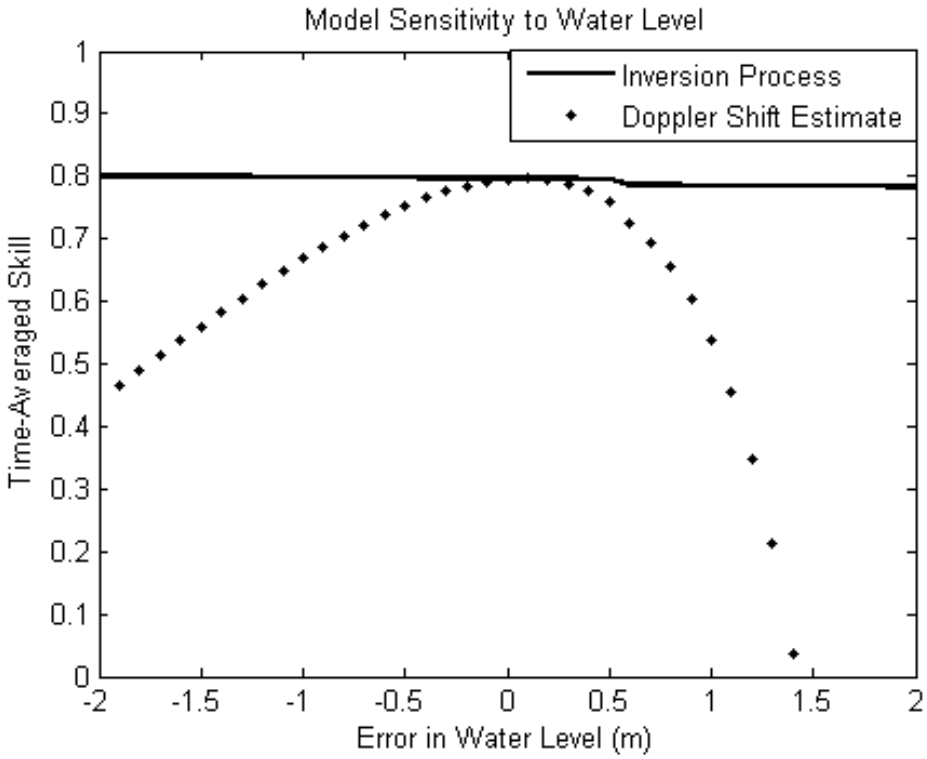

Figure 1.16 – Sensitivity of skill to error in water level estimate. Solid line describes water level sensitivity of the inversion proces assuming perfect Doppler shift estimates. Dotted line includes water depth sensitivity of the process of estimating Doppler shifts.

Chapter 2

A New Inversion Method to Obtain Upper Ocean Current Shear using X-Band Observations of Deep Water Waves

Abstract

We present a new method to estimate current-depth profiles from observations of wavenumber-dependent Doppler shifts of the overlying ocean wavefield. Consecutive scans of marine X-Band backscatter provide wavefield measurements in the time-space domain, which we transform into the directional wavenumber – frequency domain via a 3D Fast Fourier Transform (FFT). Subtracting the linear dispersion shell yields Doppler shift observations in the form of $(k_x, k_y, \Delta\omega)$ triplets. We use a constrained linear regression technique to extract the wavenumber-dependent effective velocities, which represent a weighted depth-average of the Eulerian currents (Stewart and Joy 1974). Our new method estimates these Eulerian currents from the effective velocities via the inversion of the integral relationship, which was first derived by Stewart and Joy (1974). To test the effectiveness of the method, we compare our inverted current profiles to concurrent ADCP measurements. We find the inversion method successfully predicts current behavior, with a depth-average root-mean-square (rms) error less than 0.1 m s^{-1} for wind speeds greater than 5 m s^{-1} and a broad wave spectrum. The ability of the inversion process to capture the vertical structure of the currents is assessed using a time-

average rms error during these favorable conditions. We find the time-averaged rms error is less than 0.1 m s^{-1} for depths shallower than 20 m, approximately twice the depth of existing methods of estimating current shear from wavefield measurements.

2.1 Introduction

Upper ocean processes play a major role in the transfer of heat, momentum, and gases between the ocean and atmosphere, which in turn drive local and global climate. Specifically, near surface currents are responsible for the horizontal advection of surfactants such as pollution and nutrients. Furthermore, near-surface current shear aids in the vertical advection of these tracers, which have the potential to affect biological processes and human health (Wu 1969). However, measurements of currents in the upper ocean (including depths O(10m)) are historically difficult to make, as they are contaminated by wave orbital velocities as well as wave-induced platform motion (Alpers 1981b; Davis 1981). These negative effects of wave motion can be eliminated by using remote sensing such as High Frequency (HF) radar, X-Band radar and visual imaging. These techniques use different methods to provide a measurement of wave celerity. Then, by exploiting our understanding of ocean surface wave propagation and wave dispersion, the effects of surface currents can be extracted. HF radar, for example, has been shown to provide good estimates of the average current in the upper 1 m, and is widely used to fill this gap in current measurements (Crombie 1955; Barrick et al. 1977; Teague et al. 1997; Terrill et al. 2006).

Radar, such as HF and marine X-Band, interacts with the ocean surface via Bragg scattering, which involves the EM waves interacting resonantly with ocean waves with

wavelengths corresponding to half the EM wavelength. For example, an HF radar transmitting a 12 MHz EM wave has a wavelength of approximately 25 m and resonates with an ocean wave with wavelength 12.5 m. HF operates by directly measuring the Doppler shift of the reflected EM wave, thereby measuring the velocity of the Bragg ocean wave. Marine X-Band radar, however, operates with a much higher frequency (e.g. 9410 MHz) and therefore is associated with Bragg waves in the capillary wave scale (approximately 3 cm). Rather than measuring the Doppler shift of the returned EM waves, marine X-Band radar accurately measures the range and bearing of the Bragg scatterer via a time-of-flight measurement. These capillary Bragg waves are modulated by the underlying gravity waves, causing them to collect just forward of the crest of the larger waves (Alpers 1981a; Nieto 2004). With repeating pulses emitted from a rotating antenna, consecutive backscatter maps can be constructed, which represent the location of the wave crests in directional space and time. Current information can then be extracted from the observed wave velocities using the linear wave theory (Young et al. 1985).

In deep water, linear wave theory relates wavenumber magnitude $k = |\mathbf{k}| = \sqrt{k_x{}^2 + k_y{}^2}$ and frequency, ω, via the dispersion relationship

$$\omega = \sqrt{gk} + \mathbf{k} \cdot \mathbf{u}_R(k) \tag{1}$$

where $\mathbf{u}_R(k)$ is the wavenumber-dependent *velocity of encounter*, which can be separated into two components, or $\mathbf{u}_R(k) = \hat{\mathbf{u}}(k) + \mathbf{u}_{sf}(k)$ (the velocity of the observer is assumed to be zero) (Senet et al. 2001; Dankert and Rosenthal 2004). $\hat{\mathbf{u}}(k)$ is the *effective velocity*,

which represents a weighted depth-average effect of Eulerian currents (Stewart and Joy 1974). $\mathbf{u}_{sf}(k)$ is the *filtered Stokes drift*, which is a nonlinear wave interaction correction (Weber and Barrick 1977; Ardhuin et al. 2009; Lund et al. 2015). The effect of $\mathbf{u}_{sf}$ on the wave a wavenumber k_i propagating in direction θ_i can be represented by

$$\mathbf{u}_{sf}(k_i,\theta_i) \approx u_{ss}(f_i)\cdot \mathbf{e}_{\theta_i} + 4\pi\int_{f_i}^{\infty}\int_0^{2\pi} f\cos(\theta-\theta_i)S(f,\theta)d\theta df \tag{2}$$

where $f_i = \sqrt{gk_i}/(2\pi)$, $S(f,\theta)$ is the directional wave spectrum, and $\mathbf{e}_{\theta_i}$ is the unit vector in the direction of θ_i. $\mathbf{u}_{ss}(f_i)$ represents the Stokes drift vector for waves with frequencies less than f_i by

$$\mathbf{u}_{ss}(f_i) = 4\pi\int_0^{f_i}\int_0^{2\pi} f\mathbf{k}(f,\theta)S(f,\theta)df d\theta$$

The effect of the combined currents, therefore, acts to produce a wavenumber-dependent Doppler shift with magnitude

$$\Delta\omega = \mathbf{k}\cdot\mathbf{u}_{\mathbf{R}}(k) = \mathbf{k}\cdot(\hat{\mathbf{u}}(k)+\mathbf{u}_{sf}(k)) \tag{3}$$

The relationship between the Doppler shift and the underlying current profile **u***(z)* in deep water (i.e. $kh \ll 1$ where *h* is the water depth) was derived by Stewart and Joy (1974)

$$\hat{\mathbf{u}}(k) = \frac{\Delta\omega}{\mathbf{k}} - \mathbf{u}_{sf}(k) = 2k\int_{-\infty}^{0}\mathbf{u}(z)e^{2kz}dz \tag{4}$$

In the case of a depth-uniform current $\mathbf{u}(z)=\mathbf{u}_0$, (4) suggests the effective velocity becomes independent of wavenumber, and $\hat{\mathbf{u}}(k)=\mathbf{u}_0$. To first order, $\mathbf{u}_{sf}=0$,

and a depth-uniform current can therefore be estimated with a linear fit to $\Delta\omega = \mathbf{k} \cdot \mathbf{u}_0$. In the presence of current shear, this linear fit results in a wavenumber-independent *bulk velocity*, that represents the bulk effect underlying currents have on waves. Although the bulk velocity lacks shear information, it supplies a first order current estimate used by much of the remote sensing community to derive ocean currents from wave observations (e.g. Teague et al. 1997).

In the presence of currents that vary linearly with depth, or $\mathbf{u}(z) = mz + u_0$, (4) implies the effective velocity can be expressed as

$$\hat{\mathbf{u}}(k) = -\frac{m}{2k} + u_0 = \mathbf{u}(z = -(2k)^{-1}) \tag{5}$$

This means that in the presence of a linear current profile, effective velocities of wavenumber k are equal to the geophysical velocity at an effective depth of $z = -(2k)^{-1}$. For example, under the linear current profile assumption, the effective velocity measured by a 12MHz HF radar that interacts resonantly with a Bragg wave of k=0.5 rad m^{-1} is approximately equal to the current velocity at a depth of $z = -1\text{m}$.

Similarly, if a logarithmic current-depth profile is assumed,

$$\mathbf{u}(z) = u(z = 0) - \frac{u*}{\kappa} \log\left(\frac{z}{z_0}\right)$$

where $u*$ is the friction velocity, z_0 is a roughness length and κ is the von Karman constant, then evaluating (4) results in

$$\hat{\mathbf{u}}(k) \approx u(z=0) - \frac{u^*}{\kappa}\log\left(\frac{1}{2kr}\frac{1}{z0}\right)$$

where $r = 1.78$. This result suggests the corresponding effective depth for a logarithmic current profile is $z = -(3.56k)^{-1}$ (Ha 1979). Using these two effective depth definitions, estimates of effective velocities spanning multiple wavenumbers can supply information about the current-depth profile (Stewart and Joy 1974; Ha 1979; Fernandez et al. 1996; Teague et al. 2001; Lund et al. 2015). Although these methods supply a means to extract current shear from broadband effective velocity measurements, they are dependent on an assumption of the vertical structure of the currents, and current information is constrained to a small range of depths defined by the wavenumber bandwidth and the effective depth definitions.

Ha (1979) developed a method to estimate $\mathbf{u}(z)$ from the inversion of (4) without the *a priori* assumption of a current profile shape. The input to his inversion was comprised of effective velocity measurements of four different frequency waves using a unique multi-frequency HF system. However, the inherent noise amplification of the exponential form of the inversion of (4) was not sufficiently constrained by the four unique frequency points, yielding noisy current estimates.

The aim of this study is to develop and test a new technique to estimate current depth profiles from the inversion of (4) by taking advantage of the broad wavenumber sensing capability of marine X-Band radar imaging. Our new inversion technique contains four primary steps (Figure 2.1). First, we collect X-Band backscatter data in the time-space domain, which we transform into wavenumber-frequency information via a 3-

dimensional Fourier Transform (3D FFT). Second, we remove the linear dispersion shell to create $(k_x, k_y, \Delta\omega)$ triplet points. Third, effective velocity profiles are extracted from these Doppler shift observations using a constrained regression. Finally, a stabilized inversion technique is developed to invert the effective velocities to estimate current-depth profiles. To assess the effectiveness of this method we compare these results with concurrent ADCP current measurements.

2.2 Data Collection

X-Band backscatter was collected as a part of the Office of Naval Research (ONR) funded SoCal2013 field campaign within the southern Channel Islands off the coast of Los Angeles, CA, in November 2013 (Figure 2.2). The X-Band radar antenna was mounted at a height of approximately 20 m above the sea surface on the floating instrument platform R/P FLIP (Fisher and Spiess 1963). Backscatter data was collected for nine days between 13 Nov 2013 and 22 Nov 2013, with a range and resolution of approximately 3 km and 3 m, respectively, and a scan rate of 42 rpm.

A moored Datawell buoy was deployed approximately 750 m from FLIP's location to measure wave conditions, which included a mix of wind-sea and swell (Figure 2.3). Wind conditions were measured from FLIP 10 m above sea level. The signal-to-noise ratio (SNR) of X-Band backscatter is a result of the combination of incident wind and wave conditions (Figure 2.4). SNR was highest during the first three days while wind speed was consistent and building. The second half of the time period was less consistent, with a short duration of sustained SNR on 20 Nov 2013. To avoid the strong wind

dependence on the backscatter, in this study we select only time periods when the wind speeds are greater than 5 m s^{-1}.

In support of X-Band-derived current estimates, an upward-looking 1200kHz ADCP and a downward-looking 600kHz ADCP were suspended from FLIP at a depth of -10 m and a distance 10 m from the hull. The combination of the current measurements resulted in depth-current profile estimates from -50 m to -2 m. Depth bins above -2 m were removed to avoid surface reflection and wave contamination. The evolution of the combined current profiles over time (Figure 2.5) shows evidence of wind and tidal forcing throughout the experimental time period.

2.3 Methods

To begin we defined a 750 m x 750 m inspection box, a region where we isolated backscatter data from each scan to create square subsections (Figure 2.6). We then stacked 256 consecutive square subsections (representing 6 min of data) to create a space-time cube of backscatter. A 3 dimensional Fast Fourier Transform (FFT) was then used to transform these cubes into directional wavenumber-frequency space (Young et al. 1985). The result of 3 consecutive FFTs with 50% overlap were averaged to produce spectral energy in (k_x, k_y, ω) space representing 12 minutes of backscatter (Figure 2.7).

The wavenumber bandwidth of the inversion process is defined by the dimensions and resolution of the backscatter cube, as well as the range of available observable wavenumbers. For this study, this wavenumber range was 0.05 rad $m^{-1} < k < 0.32$ rad m^{-1}.

Because of the backscatter's strong dependence on the wind, we assign the *x* and *y* directions as along- and cross-wind, respectively. A dispersion mask was applied, defining "signal" as energy that did not deviate from the dispersion relationship (1) by more than an expected maximum effective current threshold of 1 m s^{-1}. The energy that was located far from the dispersion relationship was assumed to be noise, allowing us to define a signal-to-noise ratio (SNR) (Young et al. 1985). It has been shown that the strength of the marine X-Band backscatter signal is proportional to wave height (Plant 1988). Retrieval of wave height information from X-Band backscatter data typically requires the use of a modulation transfer function (MTF), which is constructed to remove radar-imaging effects (Plant 1988). This study, however, uses only the wavenumber-frequency information and therefore does not require the use of a MTF, thus simplifying the processing. However, the magnitude of the energy returned from the FFT process reflects that of the wave spectrum, with higher energy in the lower wavenumbers than higher wavenumbers. Removing noise by applying a uniform SNR cutoff would therefore bias toward the removal of higher wavenumber information and potentially leave unwanted noise in the lower wavenumbers. To avoid this problem, instead, we applied a wavenumber-dependent SNR cutoff, selecting only (k_x, k_y, ω) points with the highest SNR in each wavenumber bin (Figure 2.7). The Doppler shift of each of these selected points was calculated by subtracting the dispersion shell (1) in the zero-current condition, or $\Delta\omega = \omega_{observed} - \sqrt{gk}$ (Figure 2.8).

The process of estimating depth-current profiles from $(k_x, k_y, \Delta\omega)$ triplets involves two major steps (Figure 2.1). First, wavenumber-dependent effective velocities

are computed from the Doppler shifts using (3). Second, current profiles are estimated from the effective velocities using an inversion of (4).

2.3.1 Estimation of the Effective Velocity Profiles

Effective velocities were estimated from Doppler shift profiles using (3) by first using a least squares process to estimate $\mathbf{u}_R(k)$, and then removing $\mathbf{u}_{sf}(k)$ estimated from wave buoy observations. Constrained least squares techniques were employed to minimize noise in the effective velocities, which is inherently amplified in the later inversion of (4) (Ha 1979). This involved constraining the curvature of the $\mathbf{u}_R(k)$ profiles, which are expected to be smooth because they can be represented by integrals of inherently smooth functions (2) and (4).

First, observations were distributed into *m* wavenumber magnitude bins, each with a unique $\mathbf{u}_R$. The i^{th} velocity of encounter can be expressed with the matrix equation

$$\begin{pmatrix} \Delta\omega_{i,j} \\ \Delta\omega_{i,j+1} \\ \\ \Delta\omega_{i,n} \end{pmatrix} = \begin{bmatrix} k_{x,i,j} & k_{y,i,j} \\ k_{x,i,j+1} & k_{y,i,j+1} \\ & \\ k_{x,i,n} & k_{y,i,n} \end{bmatrix} \begin{pmatrix} u_{Rx,i} \\ u_{Ry,i} \end{pmatrix}$$

or

$$\mathbf{\Delta\omega}_i = \mathbf{K}_i \mathbf{u}_{R_i}$$

where $\Delta\omega_{i,j}(k_{x,i,j}, k_{y,i,j})$ represents the j^{th} of *n* observations within the i^{th} wavenumber bin. Combining all wavenumber bins into one matrix equation yields

$$\begin{pmatrix} \Delta\boldsymbol{\omega}_i \\ \Delta\boldsymbol{\omega}_{i+1} \\ \vdots \\ \Delta\boldsymbol{\omega}_{\mathbf{m}} \end{pmatrix} = \begin{bmatrix} \mathbf{K}_i & & & \\ & \mathbf{K}_{i+1} & & \\ & & \ddots & \\ & & & \mathbf{K}_m \end{bmatrix} \begin{pmatrix} \mathbf{u}_{R_i} \\ \mathbf{u}_{R_{i+1}} \\ \vdots \\ \mathbf{u}_{R_m} \end{pmatrix}$$

or

$$\mathbf{d} = \mathbf{A}\mathbf{u}_R \tag{6}$$

(6) is in the appropriate form to estimate $\mathbf{u}_R$ using least squares techniques. Because there are more observation points than wavenumber bins, (6) is an overdetermined system. Therefore, the unconstrained least squares solution would result in smoother results than solving (3) for each observation point at a cost of fewer unique wavenumbers. However, the unconstrained result does not take advantage of neighboring solutions to constrain the smoothness of $\mathbf{u}_R(k)$. So, instead the smoothness was constrained by minimizing the second derivative of the solution. The second derivative of $\mathbf{u}_{R_i}$ can be estimated using a Taylor expansion by

$$\frac{\partial^2 \mathbf{u}_{R_i}}{\partial k^2} = \frac{\partial^2}{\partial k^2}\begin{pmatrix} u_{R_{x,i}} \\ u_{R_{y,i}} \end{pmatrix} \approx \frac{1}{\Delta k^2}\begin{pmatrix} u_{R_{x,i-1}} - 2u_{R_{x,i}} + u_{R_{x,i+1}} \\ u_{R_{y,i-1}} - 2u_{R_{y,i}} + u_{R_{y,i+1}} \end{pmatrix},$$

or

$$\frac{\partial^2 \mathbf{u}_{R_i}}{\partial k^2} \approx \frac{1}{\Delta k^2}\begin{bmatrix} 1 & 0 & -2 & 0 & 1 & 0 \\ 0 & 1 & 0 & -2 & 0 & 1 \end{bmatrix}\begin{pmatrix} \mathbf{u}_{R_{i-1}} \\ \mathbf{u}_{R_i} \\ \mathbf{u}_{R_{i+1}} \end{pmatrix}$$

The curvature of the combined $\mathbf{u}_R(k)$ profiles is therefore

$$\frac{\partial^2 \mathbf{u}_R}{\partial k^2} \approx \frac{1}{\Delta k^2}\begin{bmatrix} 1 & 0 & -1 & 0 & 0 & 0 & 0 & 0 & 0 & \cdots \\ 0 & 1 & 0 & -1 & 0 & 0 & 0 & 0 & 0 & \cdots \\ 1 & 0 & -2 & 0 & 1 & 0 & 0 & 0 & 0 & \cdots \\ 0 & 1 & 0 & -2 & 0 & 1 & 0 & 0 & 0 & \cdots \\ 0 & 0 & 1 & 0 & -2 & 0 & 1 & 0 & 0 & \cdots \\ 0 & 0 & 0 & 1 & 0 & -2 & 0 & 1 & 0 & \cdots \\ \vdots & \vdots & \vdots & \vdots & \vdots & \vdots & \vdots & \vdots & \vdots & \end{bmatrix}\begin{pmatrix} u_{R_{x,i}} \\ u_{R_{y,i}} \\ u_{R_{x,i+1}} \\ u_{R_{y,i+1}} \\ u_{R_{x,i+2}} \\ u_{R_{y,i+2}} \\ \vdots \end{pmatrix} \equiv \mathbf{C}\mathbf{u}_R \qquad (7)$$

To further constrain the solution to the inversion, the wavenumber - independent bulk current was used as a first guess, representing a first order depth-uniform current assumption. The bulk current was calculated from a linear regression

$$\Delta\omega = \mathbf{k} \cdot \mathbf{u}_{\mathbf{bulk}}$$

The bulk velocity vector was then reformatted to match $\mathbf{u}_R$. Solving (6) while constraining the curvature (7) yielded the least-squares result

$$\mathbf{u}_R = \mathbf{u}_{\mathbf{bulk}} + (\mathbf{A}^T\mathbf{A} + \lambda\mathbf{C}^T\mathbf{C})^{-1}\mathbf{A}^T(\mathbf{d} - \mathbf{A}\mathbf{u}_{\mathbf{bulk}})$$

where λ is a tunable scalar representing the extent to which the curvature is constrained. The effective velocities are then

$$\hat{\mathbf{u}} = \mathbf{u}_{\mathbf{bulk}} + (\mathbf{A}^T\mathbf{A} + \lambda\mathbf{C}^T\mathbf{C})^{-1}\mathbf{A}^T(\mathbf{d} - \mathbf{A}\mathbf{u}_{\mathbf{bulk}}) - \mathbf{u}_{sf} \qquad (8)$$

Following Ardhuin et al. (2009), the Stokes drift vector was approximated by the non-directional Stokes drift $u_s(f_i) = \frac{16\pi^3}{g}\int_0^{f_i} f^3 E(f)df$, where $E(f)$ is the one dimensional energy spectrum. The filtered Stokes drift contribution in (2) was calculated

using $u_s(f)$ and the directional wave spectrum from the moored wave buoy. The along-wind and cross-wind components $\hat{u}_x(k)$ and $\hat{u}_y(k)$ were then used to estimate currents $u_x(z)$ and $u_x(z)$ individually.

2.3.2 Current Profile Inversion

An inversion method was developed to estimate current profiles from the wave-number dependent effective velocities $\hat{\mathbf{u}}(k)$. Previous work in deep water (Ha 1979) showed that the inversion of (4) lead to amplification of measurement noise. The inversion process was therefore stabilized by 1) applying Legendre quadrature to approximate (4) as a finite sum (Cohen 2007) and 2) using multiple constrained least squares techniques to estimate current profiles (Twomey 1977; Wunsch 1996).

Legendre quadrature suggests that an integral of a smooth function f(ξ) can be estimated as the weighted sum

$$\int_{-1}^{1} f(\xi)d\xi \approx \sum_{i=1}^{n} f(\xi_i)w_i \tag{9}$$

where ξ are the zeros of the Legendre polynomial of order *n,* and *w* are their weights, both of which are tabulated (Golub and Welsch 1969; Cohen 2007). To change of the form of (4) to match (9), the substitution

$$\xi = 2e^{-2k_0 z} - 1$$

was made, where k_0 is a reference wavenumber chosen to minimize quadrature error (Ha 1979). The resulting integral is

$$\frac{2\hat{\mathbf{u}}(k)}{k/k_0} = \int_{-1}^{1} \mathbf{u}(z)\left(\frac{1}{2}\xi + \frac{1}{2}\right)^{\frac{k}{k_0}-1} d\xi \,, \tag{10}$$

where

$$z = \frac{\ln\left(\frac{1}{2}\xi + \frac{1}{2}\right)}{-2k_0} \tag{11}$$

Applying (9) to (10) and (11) yields

$$\frac{2\hat{\mathbf{u}}(k)}{k/k_0} \approx \sum_{i=1}^{n}\left(\frac{1}{2}\xi_i + \frac{1}{2}\right)^{\frac{k}{k_0}-1} \mathbf{u}(z_i)w_i \,,$$

or

$$\mathbf{f} = \mathbf{G}\mathbf{u} \,, \tag{12}$$

where

$$\mathbf{f}_j = \frac{2\hat{\mathbf{u}}(k_j)}{k_j/k_0}$$

$$\mathbf{G}_{ij} = \left(\frac{1}{2}\xi_i + \frac{1}{2}\right)^{\frac{k_j}{k_0}-1} w_i$$

$$\mathbf{u}_i = u(z_i)$$

$$z_i = \frac{\ln\left(\frac{1}{2}\xi_i + \frac{1}{2}\right)}{-2k_0}.$$

Similar to (6), the form of (12) is appropriate for using least squares techniques to estimate $\mathbf{u}(z)$. Again, because the solution is expected to be smooth, the curvature was constrained using the second derivative approximation

$$\frac{\partial^2 \mathbf{u}}{\partial z^2} \approx \frac{1}{\Delta z^2}\begin{bmatrix} 1 & -1 & 0 & 0 \\ 1 & -2 & 1 & 0 \\ 0 & 1 & -2 & 1 \\ 0 & 0 & 1 & -2 \end{bmatrix}\mathbf{u} \equiv \mathbf{D}\mathbf{u}. \tag{13}$$

To further constrain the inversion result, the observations were weighted by their variances with

$$\mathbf{S} = \mathbf{I}\delta \tag{14}$$

where $\delta_i = \sigma_i^{-2}$, the inverse variance of the Doppler shifts in the i^{th} wavenumber bin.

As previously, we used a uniform depth current as an initial guess

$$\mathbf{u}_0 = \mathbf{u}_{Bulk}$$

Combining (12), (13) and (14) resulted in the cost function

$$\Lambda = (\mathbf{G}\mathbf{u} - \mathbf{f})^T\left(\mathbf{D}^T\mathbf{D}\right)(\mathbf{G}\mathbf{u} - \mathbf{f}) + \eta\left[\mathbf{f}^T\left(\mathbf{S}^T\mathbf{S}\right)\mathbf{f}\right] + \gamma(\mathbf{u} - \mathbf{u}_0)^T(\mathbf{u} - \mathbf{u}_0) \tag{15}$$

where η and γ are tunable parameters, specifying the relative extent to which curvature minimization, distance from the first guess, and the weighted model are constrained. Minimizing (15) with respect to **u** yields the least squares result

$$\mathbf{u} = \left[\mathbf{G}^T(\mathbf{S}^T\mathbf{S})\mathbf{G} + \eta(\mathbf{D}^T\mathbf{D}) + \gamma\mathbf{I}\right]^{-1}(\mathbf{G}^T(\mathbf{S}^T\mathbf{S})\mathbf{f} + \gamma\mathbf{I}\mathbf{u_0}). \quad (16)$$

This result was used to estimate current profiles $u_x(z)$ and $u_y(z)$ from effective velocities $\hat{u}_x(k)$ and $\hat{u}_y(k)$, respectively.

To test the robustness of the inversion results, we compared our current profile estimates to those measured by the acoustic instruments. The root mean square error (RMSE) was used as the error metric to evaluate the success of the inversion model, where we define RMSE as

$$RMSE = \sqrt{\left\langle \left(u_{inverted} - u_{measured}\right)^2 \right\rangle}, \quad (17)$$

and $\langle\ \rangle$ denotes an average either over depth (to see time-dependence) or time (to see depth-dependence).

2.4 Results

Current profiles were estimated from X-Band-derived Doppler shift estimates using (8) and (16) using ten days of data. To increase the signal-to-noise of the Doppler shift signal, one hour of $(k_x, k_y, \Delta\omega)$ triplets were combined to estimate the effective velocities from (8).

To tune the weighting parameter λ in (8) and asses the result of the effective velocity estimation, a *forward* solution of (4) was found, which transformed ADCP current profiles into effective velocity – wavenumber profiles. This forward solution supplied useful insight into the relationship between current profiles and the overlying wavefield. For example, the exponential weighting of near-surface currents in (4) and the truncation of ADCP profiles above 2 m depth resulted in a bias between the forward solution and estimated effective velocities. To remove this bias, a surface current of magnitude $u_0 \approx \hat{u}(k_{\max})$ was added to the ADCP current profiles. The forward problem was then carried out to estimate the effective velocity. Here, λ was chosen to minimize the difference between the estimated effective velocities from (8) and the calculated effective velocity from the forward problem.

To compare the results of the forward problem with the modeled effective velocity estimates from (8), (3) was used to calculate $(k_x, k_y, \Delta\omega_{forward})$ and $(k_x, k_y, \Delta\omega_{XBand})$ triplets, where (k_x, k_y) were chosen to span all directions (Figure 2.9). As indicated by (4), a depth-uniform current $\mathbf{u}_0$ would result in a Doppler shift-wavenumber relationship $\Delta\omega \approx \mathbf{k} \cdot \mathbf{u}_0$, or a plane in $(k_x, k_y, \Delta\omega)$ space. Because our results show non-linear contour lines (Figure 2.9), this is an indication of that current shear is present. The strength and direction of the gradient of the Doppler shift- wavenumber relationships as well as their contour line shapes behave similarly, indicating the estimated effective velocities from (8) agree with the forward solution of (4) in magnitude, direction, and current shear content.

To ensure $\hat{\mathbf{u}}(k)$ estimated from (8) were not biased by the least squares process, the triplets $\left(k_x, k_y, \Delta\omega_{XBand}\right)$ were compared to those calculated by the FFT. The difference between this new set of Doppler shift-wavenumber pairs and those observed (e.g. Figure 2.8) represents the residual from (8) (Figure 2.10). The residual field is made up of small magnitude (green) values with no coherent structure in wavenumber space. This indicates the least squares technique (8) does not introduce significant bias into the effective velocity estimates.

Currents were estimated from the effective velocity profiles using (16) in the along-wind and cross-wind directions (Figure 2.11). For these data, we excluded time periods when the wind speed fell below 5 m s^{-1}. Because the integral in (4) accounts for currents at infinite depth, the depths to which the current inversion attempts to estimate currents is bounded only by the order of the Legendre Polynomial in (9). However, it is expected that the inversion has an effective depth to which inverted currents yield reliable results. Furthermore, this effective depth is expected to be dependent on the wavenumber bandwidth used in the inversion. The results show that both orthogonal current estimates approach zero at a depth of approximately 20 m, below which they rapidly become unrealistically large. Because this structure is not seen in the ADCP current profiles, this suggests the effective depth of this inversion process is approximately -20 m.

Based on our finding of -20 m for the effective depth of the inversion, we calculated the depth-averaged RMS error between inverted and ADCP currents to only -20 m depth (Figure 2.12). The average RMS errors during the first three days of the experiment were primarily below 0.1 m s^{-1}, with slightly higher errors in the cross-wind

direction. Error in the second half of the experiment, however, was typically larger than 0.1 m s^{-1} despite similar wind speeds. We attribute the higher error in the second half of the experiment to the distribution of energy in the wavefield. The periodogram from the moored Datawell buoy (Figure 2.3) shows that the location of wave energy in spectral space varied throughout the experiment. During first half of the experiment, wave energy was broadly spread throughout the band of frequencies used in the X-Band inversion (i.e. 0.7 rad s^{-1} to 1.7 rad s^{-1}). Later in the experiment, however, there was a lack of energy in either the higher (e.g. 19 Nov 2013) or lower (e.g. 20 Nov 2013) parts of the inversion's frequency band (Figure 2.3). A comparison of the wave spectra from 1300 UTC 13 Nov 2013 and 1300 UTC 20 Nov 2013 (Figure 2.14) shows the lack of wave energy in the lower part of the inversion frequency band on the later date. The higher RMS error during time periods when there are gaps in the energy spectrum implies the inversion is not only dependent on wind speed, but also on the available observable wavenumbers determined by the wave spectrum.

The tunable parameters η and γ in (17) were chosen to minimize RMS error. This process showed little sensitivity to fluctuations in γ between 0.1 and 1. The selection of η, however, was found to have a larger effect on the inversion. In general, a large η resulted in a smooth $u(z)$ profile, which effectively constrained the noise amplification with the cost of neglecting current shear. During times of high SNR, therefore, a smaller value of η could be used to attempt to capture more of the current shear structure. Data with lower SNR, however, contained more noise, requiring a larger value of η to constrain the noise amplification. Thus, we devised this simple empirical relationship between SNR and η

$$\eta(SNR) = 0.25 + 0.3\left(1 - \frac{SNR}{SNR_{\max}}\right)$$

leading to a value of η varying between 0.25 and 0.35.

The depth-dependence of the inversion result was evaluated with a time-average RMS error from (17) between inverted and measured velocity profiles (Figure 2.13). To assess this error separately from the depth-averaged error, only time periods during which the depth-average RMS error was less than 0.1 m s^{-1} were used. The inversion performs well, with an RMSE>0.1 m s^{-1} in the top 20 m, as was qualitatively expected from Figure 2.11. RMS error in the along-wind direction is smaller on average, and remains small deeper than the cross-wind direction. The depth dependence of the RMS error was also compared to the RMS error of currents estimated under the linear, logarithmic, and depth-uniform current profile assumptions (e.g. from (5)). In the along-wind direction, where current shear was highest, all three methods that took current shear into account performed better than the depth-uniform assumption (Figure 2.13a). The tidally dominated cross-wind currents were more appropriately approximated by the depth-uniform assumption, which resulted in RMS errors that were similar to the methods that took shear into account (Figure 2.13b). For both directions, currents estimated under the logarithmic and linear assumptions exhibited very similar behavior to the inversion at the depths at which they are defined, with RMS errors within 0.02 m s^{-1} of each other. However, the inversion continued to perform with similar errors down to a depth of approximately -20 m.

2.5 Discussion

The inversion method summarized by (8) and (16) successfully captured time and depth fluctuations of along- and cross-wind currents (Figure 2.11, Figure 2.12, and Figure 2.13). These results proved to be strongly dependent on environmental conditions, specifically wind speed and wave spectra. In favorable conditions (e.g. 13 Nov 2013 to 16 Nov 2013), the estimated currents had RMS errors less than 0.1 m s^{-1}. This error is similar to other reported radar-derived current estimates, which range between 0.07 and 0.2 m s^{-1} (e.g. Paduan 1996; Graber 1997; Teague et al. 2001; Kelly 2003). The smaller errors in the along-wind direction than in the cross-wind direction can be attributed to two factors. First, there is a strong dependence between winds and X-Band backscatter energy, where the backscatter is strongest in the direction of the wind (Dankert et al. 2003). Second, because wind and wave directions were similar throughout the experiment (Figure 2.4), both winds and waves contribute to the clustering of $(k_x, k_y, \Delta\omega)$ triplet points in the wind direction (Figure 2.7), leading to larger error in (8) in the cross-wind direction.

The success of the current inversion technique showed strong dependence on environmental conditions. As expected, the envelope of environmental conditions in which the inversion performed successfully is defined by the wind and wavefield. Specifically, wind speeds greater than 5 m s^{-1} and a wave spectrum with significant energy spanning the entire frequency range used in the inversion process lead to the lowest RMS error (Figure 2.12). Environmental variables that did not vary appreciably

during this experiment, but would be expected to play a role in the inversion include wave directional spread, split sea-swell events, and wind-wave direction differences.

Because of the inversion's sensitivity to the wave spectrum, one possible improvement to this inversion model is to bandpass the frequency of waves used in the inversion based on the measured wave spectrum. Changes in the frequency band, however, would require changes in the weighting parameters and would result in fluctuations of the model's effective depth..

2.5.1 Error Estimation

Although the RMS error suggests a close relationship exists between inversion error and the environmental conditions, there is not a clear way to quantify the individual effect wind and waves have on error. Instead, the source of error can be broken into components, such that the Doppler shift in (3) is

$$\Delta\omega_{observed}(k) = \Delta\omega_{True}(k) + \Delta\omega'(k) + \varepsilon_{radar}(k) \tag{18}$$

where $\Delta\omega_{True}$ is the error-free Doppler shift caused by the underlying currents. $\Delta\omega'$ is the wavenumber-dependent random noise in the observations based on data resolution, small nonlinear interactions, etc. ε_{radar} is a bias introduced by the assumption that the radar backscatter perfectly represents the spectral quantities of the wavefield. The inversion result, therefore, can be expressed as

$$u_{Inverted}(z) = u_{True}(z) + u'(z) + \hat{\varepsilon}_{radar}(z) + \delta_E(z) + \delta_I(z)$$

where u_{True} is the true current profile, u' represents the propagation of the random error in the Doppler shifts and $\hat{\varepsilon}_{radar}$ represents the radar bias that is propagated through the inversion process. δ_E is the bias introduced during the estimation of effective velocities in (8). Because of the form of the kernel in (6) (i.e. geometrically, (6) describes an overdetermined planar fit for each wavenumber bin), δ_E is expected to be very small, which is supported by the low bias of the residuals in Figure 2.10. δ_I is the depth-dependent bias introduced by the inversion process (16), which is to be determined. The error associated with the inversion process can therefore be approximated by estimating the terms $u'(z)$ and $\delta_I(z)$. This requires separating the effects of the input noise in (18).

The random noise in the radar-derived Doppler shift, $\Delta\omega'(k)$, was approximated using the scatter of the residuals in Figure 2.10. The standard deviation of the spread of these residuals was azimuthally averaged to produce profiles of $\sigma_{\Delta\omega}(k)$ for each time point for which the environmental envelope described above was filled (000 UTC 13 Nov 2013 to 0300 UTC 16 Nov 2013) (Figure 2.15). Because of the small variation among these profiles, the average $\sigma_{\Delta\omega}(k)$ profile is a good representation of the random noise for this time period.

There are many individual error sources that contribute to ε_{radar} including the various effects related to the geometry of the radar imaging. The shadowing of smaller waves by larger waves, for example, affects the spectrum of the wavefield observation. By imaging only smaller waves located near the crests of larger waves where orbital velocities are largest, shadowing also introduces bias into the Doppler shift of the smaller

waves. Furthermore, the effect of shadowing increases with range from the radar, as the imaging angle between the radar antenna and the sea surface decreases. This introduces heterogeneity within the inspection square, which is spatially averaged by the FFT. Wave height and wave age also play roles in the geometry of the radar imaging, affecting wave shadowing. Additionally, temporal and spatial fluctuations in wind speed also introduce heterogeneity in the wavefield imaging. These combined effects make it impractical to formulate an analytical solution to the influence of ε_{radar} on the Doppler shift estimate. However, if it is assumed that the forward solution to (4) using ADCP currents approximates $\Delta\omega_{True}$, a hybrid set of Doppler shifts can be constructed such that $\Delta\omega_{hybrid} = \Delta\omega_{True} + \Delta\omega'$, where $\Delta\omega'(k)$ is made up of random noise with wavenumber-dependent standard deviation $\sigma_{\Delta\omega}(k)$.

We constructed a hybrid Doppler shift profile for currents measured on 000 UTC 15 Nov 2013. A Monte Carlo analysis was used to estimate $u'(z)$ and $\delta_I(z)$ by inverting the constructed Doppler shifts and comparing them to the ADCP current profile. The results of 100 iterations of this process (Figure 2.16) show that both $\delta_I(z)$ and $u'(z)$ increase with depth, as expected from the exponential weighting in (4). The maximum of their combined values remains less than 0.05 m s^{-1} in the top 20 m, suggesting it makes up approximately half of the error in the inversion, with the other half contained in ε_{radar}. The value of the inversion bias $\delta_I(z)$ is dominated by the exponential shape of the kernel of (12), leading to its increase with depth. However, $\delta_I(z)$ is also sensitive to strong current shear, as seen in Figure 2.16a, between -15 and -20 m depth. This bias is

introduced by the necessity of enforcing a smooth current profile via the constraint in (13) and is directly related to the selection of η as discussed above.

A potential way to minimize the enhanced noise observed at low wavenumbers (Figure 2.15) is to increase the size of the inspection square, thereby sampling a higher number of longer waves. This could also provide signal at wavenumbers lower than the 0.05 rad m^{-1} cutoff used in this study. However, (4) shows that the integral express that is inverted in this work is proportional to $\Delta\omega k^{-2}$. The use of lower wavenumbers, therefore, increases the amplification of noise in the Doppler shift measurement. Therefore, if lower wavenumbers (i.e. k<0.05 rad m^{-1}) are used in the inversion process, care must be taken to reduce the noise to a lower level than was observed in this study.

2.6 Conclusion

This work has presented the development and application of a new current inversion method, using the wavenumber-dependent Doppler shift measurements of X-Band radar to estimate depth-dependent currents. The results of the current inversion showed RMS error less than 0.1 m s^{-1} for wind speeds greater than 5 m s^{-1} and a wave spectrum containing wave energy throughout the inverted wavenumber band. For the wavenumber range used for this study (0.05 rad m^{-1}<k<0.3 rad m^{-1}), the RMS error of inverted currents was below 0.1 m s^{-1} to a depth of approximately -20 m. The time and depth dependences of the RMS error of the current inversions indicate the inversion process is capable of estimating currents with a similar error as other radar-based

methods, but with approximately twice the depth range (Figure 2.13) and without an *a priori* assumption of the current-depth profile shape.

Although the X-Band backscatter used in this study was collected from a stationary floating platform, X-Band can operate with similar performance from moving vessels. This inversion process could therefore be used with a ship-based system with the requirement that the inspection square be illuminated by the radar for the required FFT window (6 min).

The results of the inversion process (Figure 2.11) indicate an amplification of the near-surface current in the along-wind direction, but not in the cross-wind direction. Although a detailed analysis of this result is left for future work, this is qualitatively consistent with models of wind-driven currents. This result holds promise for the inversion process developed here to provide current shear information in the upper few meters, a regime in which it has been historically difficult to make current measurements.

2.7 Acknowledgements

The authors would like to thank the Office of Naval Research for funding support and collaborator Ken Melville and his group at Scripps Institution of Oceanography for collecting wind stress data. We would also like to thank USACE for CDIP buoy data support and the crews of R/P FLIP and R/V Melville during the SoCal2013 experiment. Chapter 2 has been submitted to the *Journal of Atmospheric and Oceanic Technology* in 2016. Campana, Jeffrey; de Paolo, Anthony; Terrill, Eric J., A New Inversion Method to

Obtain Upper Ocean Current Shear using X-Band Observations of Deep Water Waves. The dissertation author was the primary investigator and author of this paper.

Table 2.1 – Configuration parameters for the X-Band system used during SoCal2013

SoCal 2013 X-Band Configuration Parameters	
Radar Type	Furuno 2117bb
Peak Output Power	12 kW
Antenna Length	8 ft
Beam Width	0.95^0 (Horizontal) 20^0 (Vertical)
Radar Scan Rate	42 rpm
Range Resolution	3 m
Maximum Range	~3 km
Radio Wave Frequency	9410 +/- 30 MHz
Bragg Scatterer Wavelength	3.2 cm
Antenna Height	30 m
ADC resolution	12 bit

Table 2.2 – Parameters used in the deep water current inversion process.

Inversion Parameters		
Description	Variable	Value
FFT window	-	3x6 min, 50% overlap
Radar Box size	-	~750m x 750m
Curvature Constraint 1	λ	3
Legendre Order	n	30
Curvature Constraint 2	η	$0.3\left(1-\frac{SNR}{SNR_{\max}}\right)$
Data Weighting Constraint	γ	0.5
Reference Wavenumber	k_0	0.035 rad m^{-1}
Wavenumber Range	-	0.04 to 0.35 rad m^{-1}

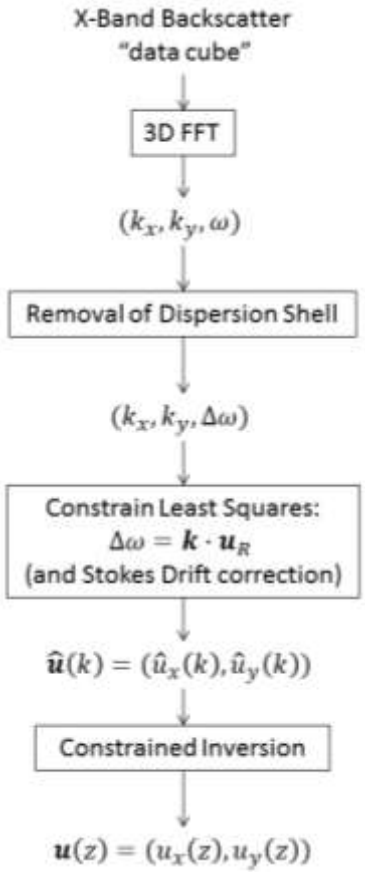

Figure 2.1 – Flow chart describing the four main parts of the inversion process that begins with building the data cube of X-Band backscatter and ends with the inversion of current profiles.

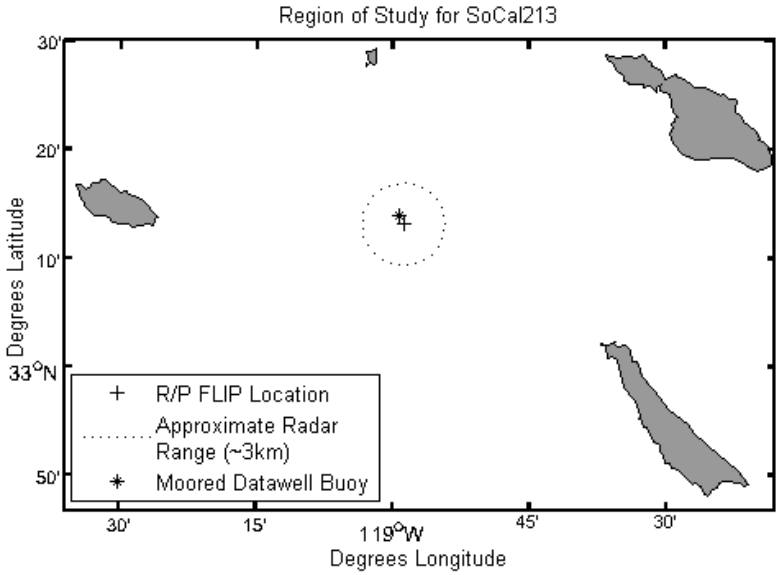

Figure 2.2 – Map showing the study region for the SoCal2013 experiment in southern California, depicting regions of land (gray) and water (white). R/P FLIP (+) was stationed between San Nicolas Island to the west and Santa Catalina Island to the east. The dotted circle denotes the maximum radar range of approximately 3 km used for this study. The average location of the moored wave buoy (asterisk) was approximately 750 m from FLIP.

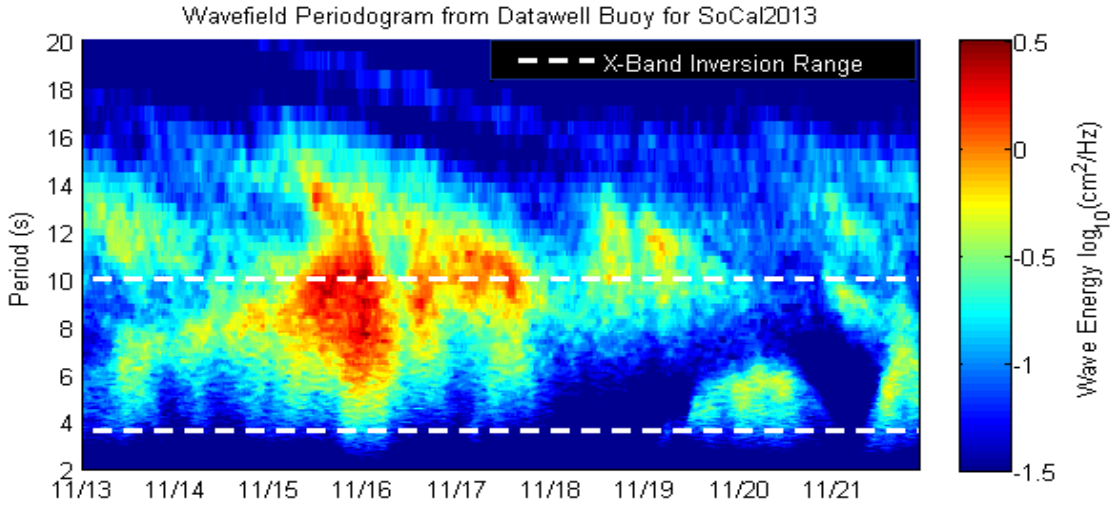

Figure 2.3 – The periodogram from the moored Datawell wave buoy. The region bound by white dashed lines indicates the range of wave periods (4 s -10 s) used in the inversion process. Warmer and cooler colors indicate high and low wave energy, respectively.

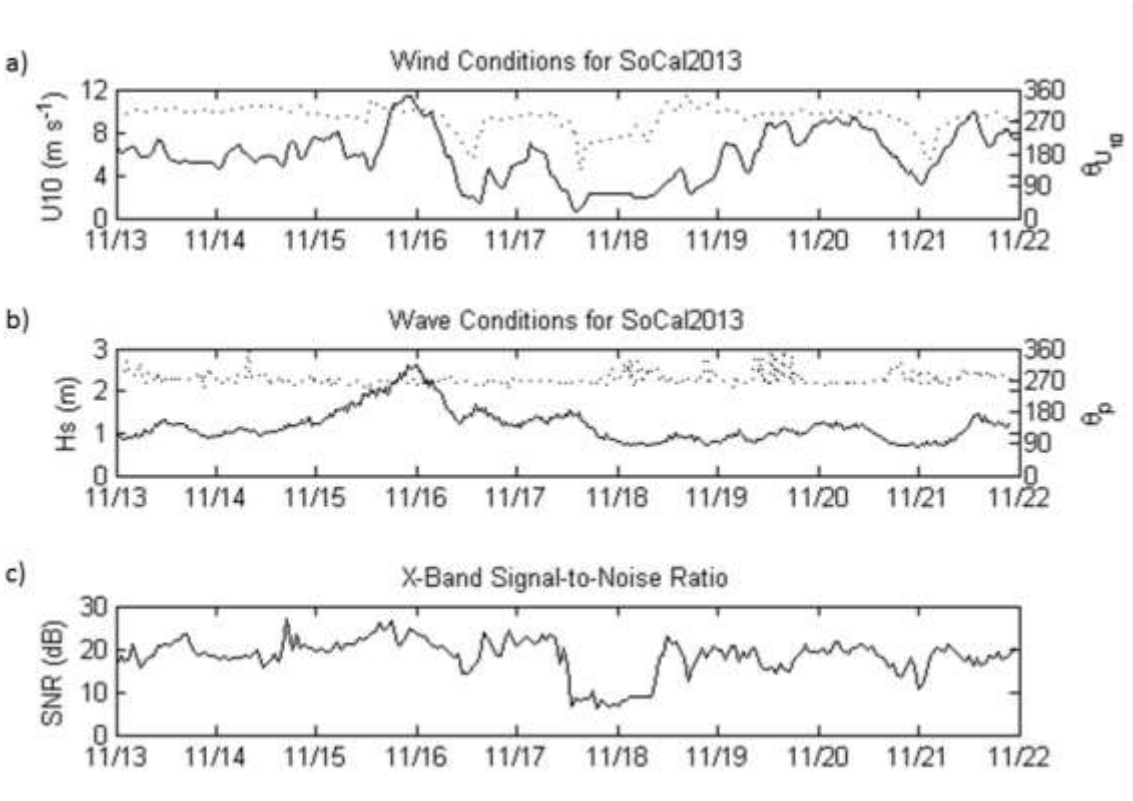

Figure 2.4 – Environmental conditions during the SoCal2013experiment as a function of time. a) Wind speed (solid) and direction (dotted) measured on R/P FLIP. b) Significant wave height (solid) and peak wave period (dotted) from the moored Datawell buoy. c) X-Band SNR resulting from wind-wave conditions.

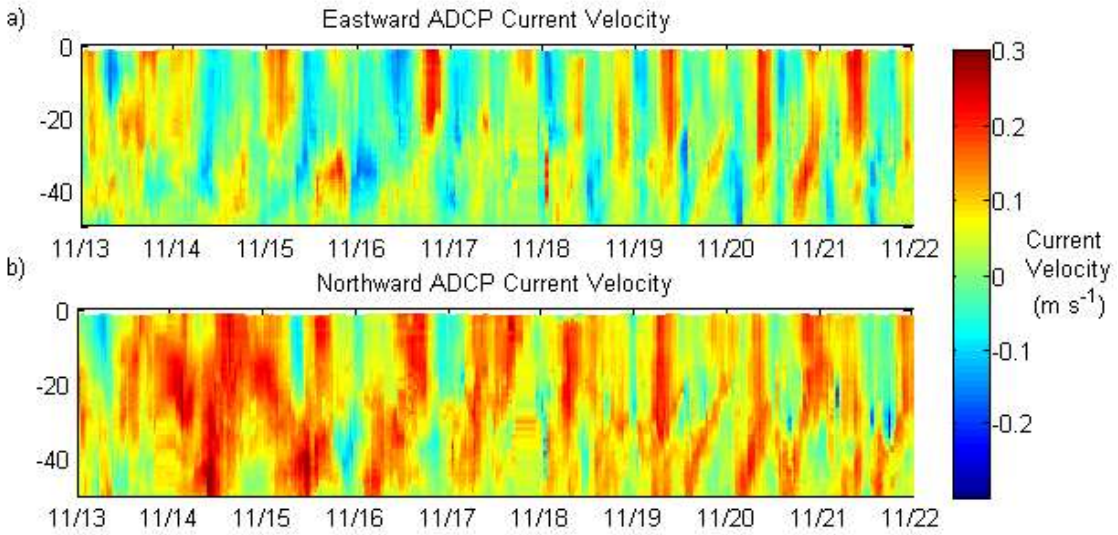

Figure 2.5 – Evolution of the depth-dependent currents measured by both ADCPs suspended from R/P FLIP for the 10 days of data recording (13 Nov 2013 to 22 Nov 2013) for: (a) eastward current velocity and (b) northward current velocity. Colors represent current velocities, where warm colors indicate velocity in the eastward (for panel a) and northward (for panel b) direction and cool colors represent velocities in the western (for panel a) and southward (for panel b) directions.

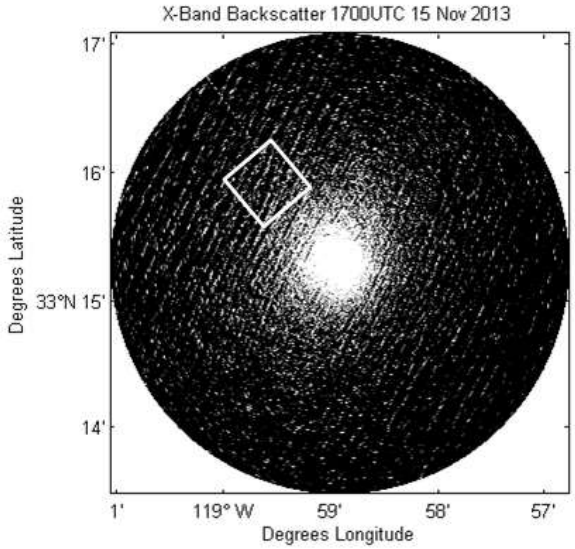

Figure 2.6 – An Example of a single X-Band scan showing strong backscatter from the dominant wave signal propagating from the Northwest for data recording on 1700 UTC 15 November 2013. Shading represents relative backscatter intensity, where black indicates low energy and white indicates high energy. The white inspection (square placed 1 km from FLIP into the wind) outlines wave information used for this study.

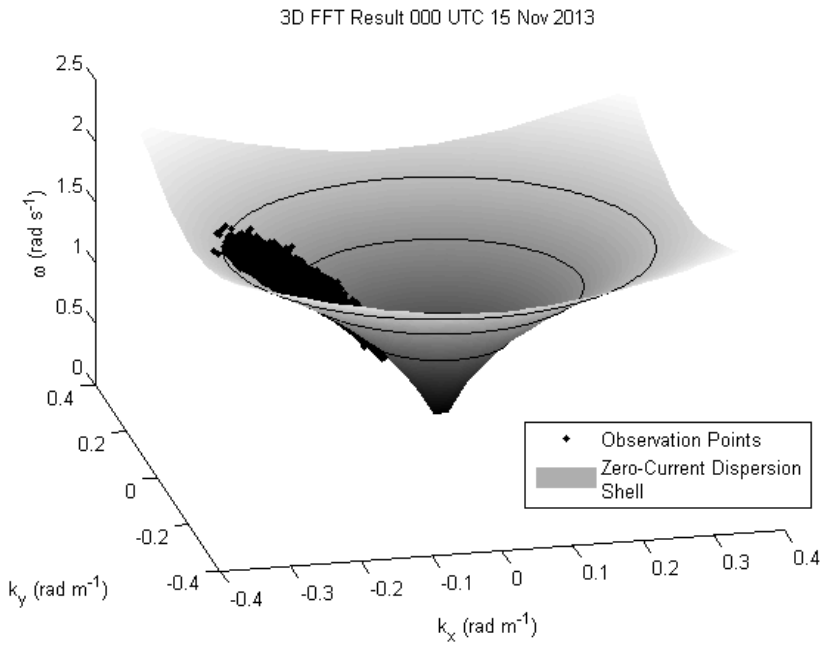

Figure 2.7 – Graphical representation of (k_x, k_y, ω) triplet points (black diamonds) from the 3D FFT performed on the 000 UTC 15 Nov 2013 data in the along-wind (x), cross-wind (y) coordinate system, where the vertical axis represents radian frequency. The points are Doppler shifted from the zero-current dispersion shell defined by (1) by the underlying currents. Black rings denote zero-current dispersion for wavenumbers 0.1, 0.2 and 0.3 rad m^{-1}, for rings of larger diameters, respectively.

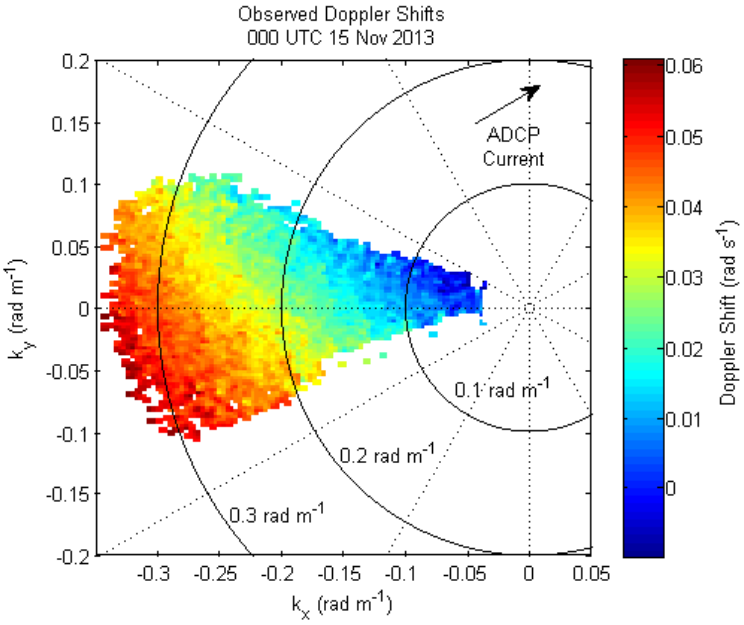

Figure 2.8 – Directional wavenumber-Doppler shifts color-coded by Doppler shift amplitude, used for estimating currents on day 000 UT 15 Nov 2013. Black rings denote wavenumber magnitudes 0.1, 0.2 and 0.3 rad m^{-1}, where smaller radius circles represent smaller wavenumbers. The black arrow indicates the direction of the depth-averaged ADCP currents between -10 m and -2 m depths.

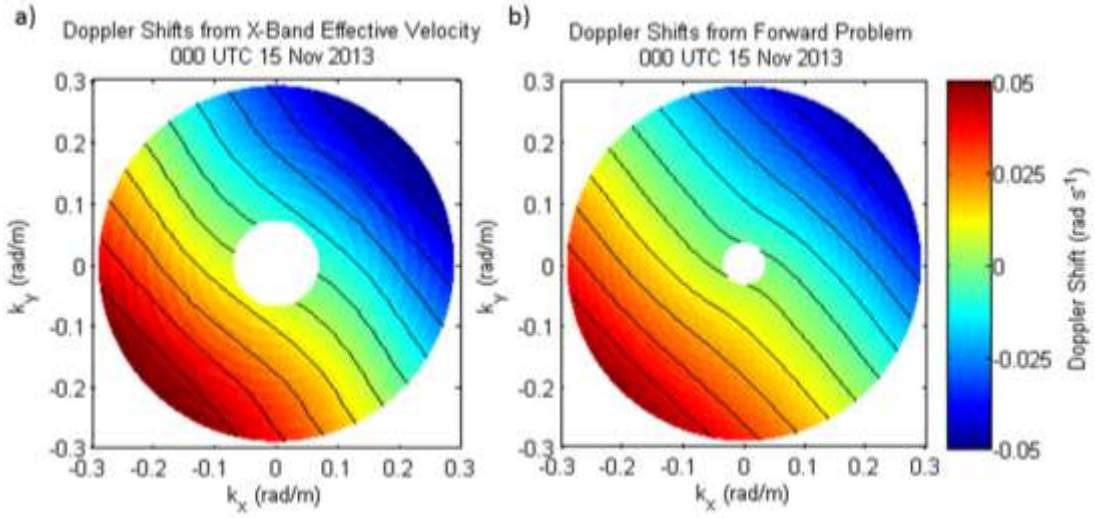

Figure 2.9 – A comparison of Doppler shifts calculated from (a) the effective velocity from (8) and (b) those from the forward problem. In the absence of current shear the counters would map as straight lines, so here the non-linearity of the contours indicate the presence of current shear. Green indicates no Doppler shift, whereas warmer (cooler) colors indicate positive (negative) Doppler shifts.

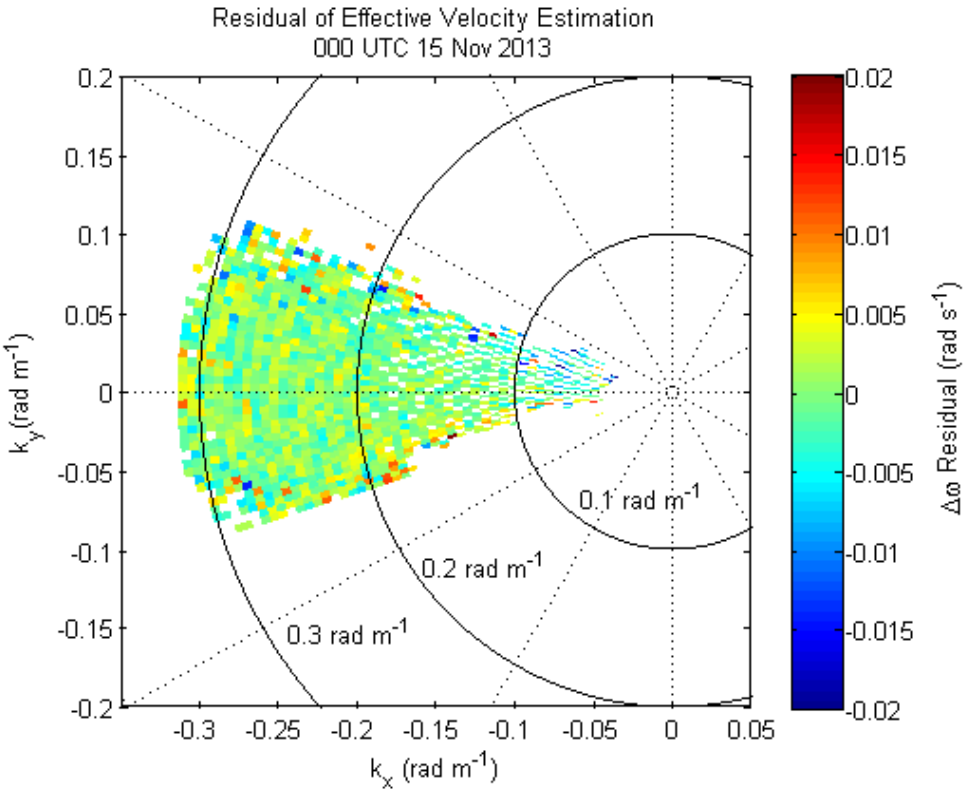

Figure 2.10 – The Doppler shift residuals, $\Delta\omega - \hat{\mathbf{u}}(k) \cdot \mathbf{k}$, derived from estimating effective velocities $\hat{\mathbf{u}}(k)$ from (8). Green denotes zero residual and red (blue) denotes positive (negative) residual.

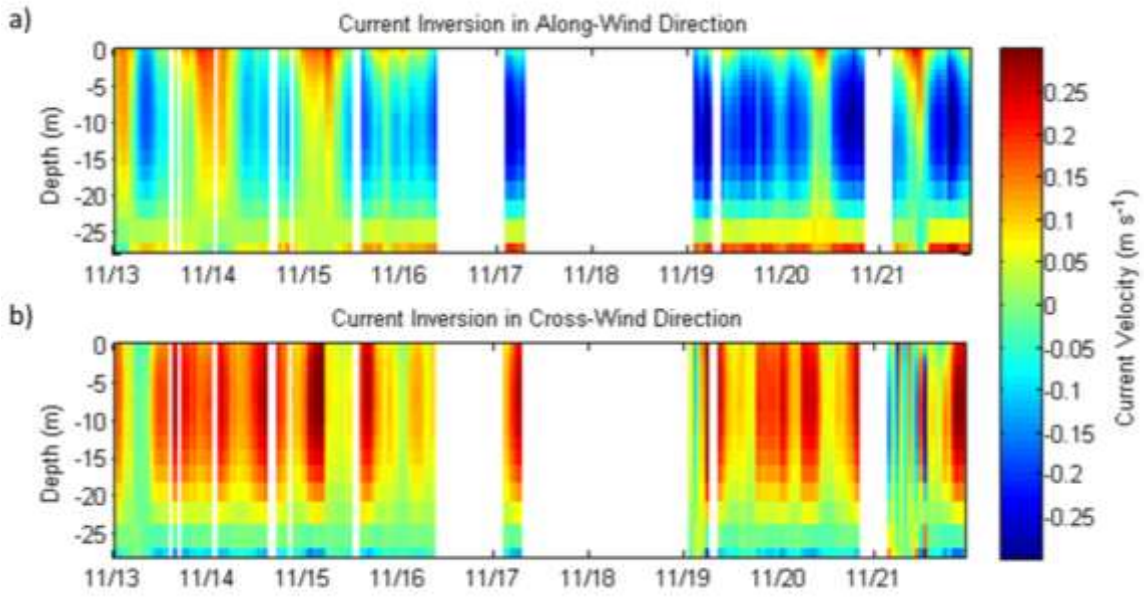

Figure 2.11 – Results of current inversion in: (a) along- and (b) cross-wind directions. White spaces indicate times of excluded data because the wind speed fell below our threshold value of 5 m s^{-1}. Warm colors represent higher velocities in the along-wind (panel a) and cross-wind (panel b) directions and cool colors represent higher velocities in the opposite direction.

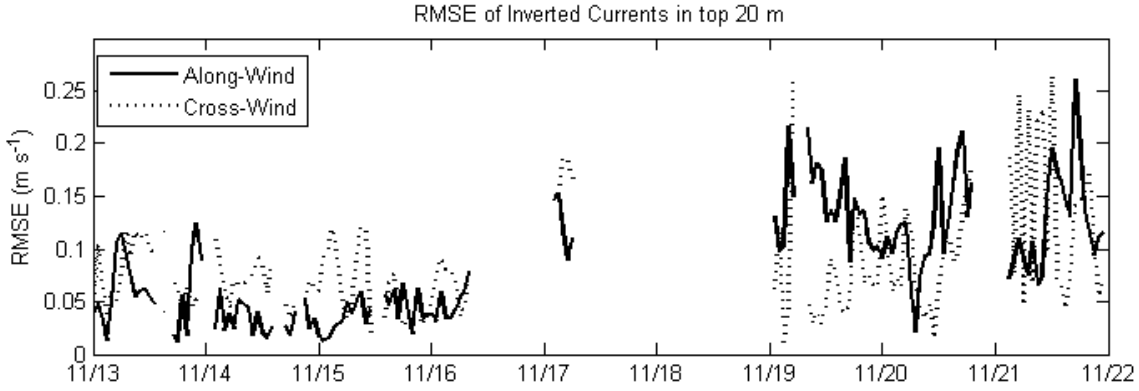

Figure 2.12 – The time series of the RMS error of inverted currents in the top 20 m for along- and cross-wind directions. Blank time periods indicate times of wind speeds less than 5 m s^{-1}.

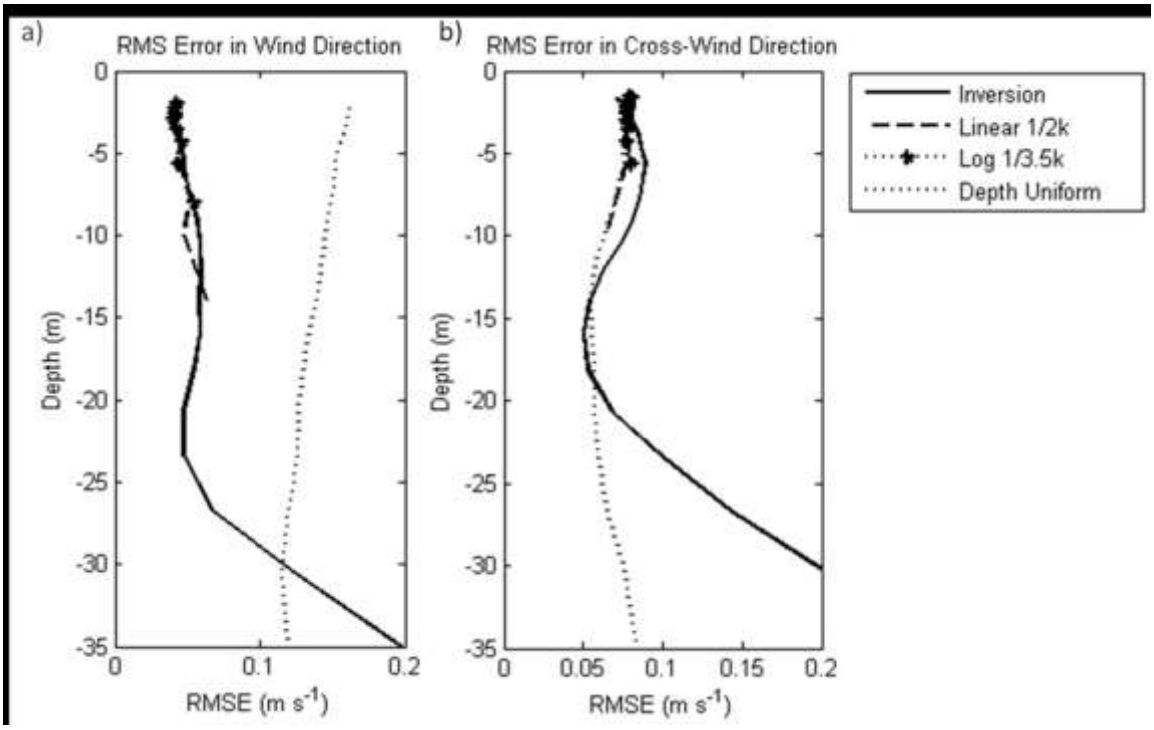

Figure 2.13 – The depth-dependence of RMS error of the (a) along-wind and (b) cross-wind current-depth profiles estimated by the Inversion (solid), a linear assumption (dashed), a logarithmic assumption (star-dotted) and depth-uniform (dotted). RMS error was calculated for times between 000 UTC 13 Nov 2013 and 0800 UTC 16 Nov 2013.

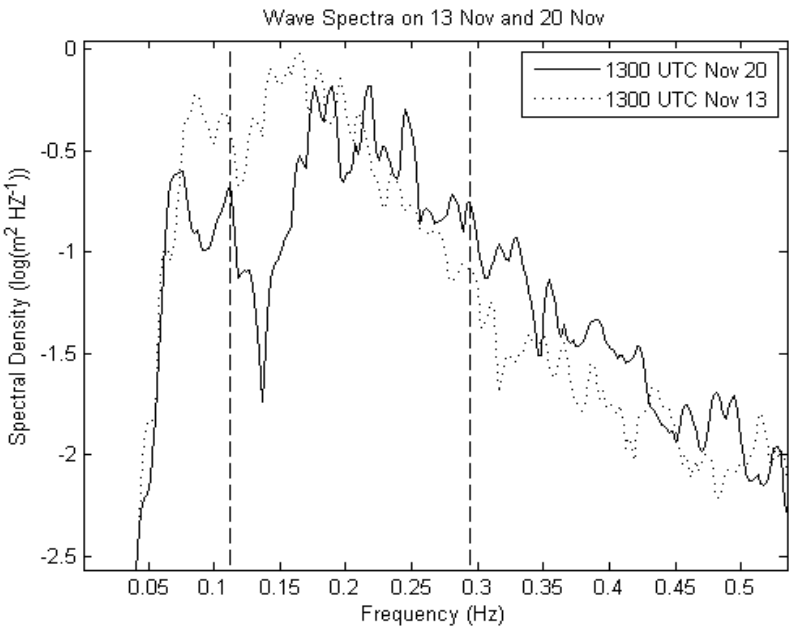

Figure 2.14 – Comparison of one-dimensional wave spectra from the Datawell buoy on 13 November 2013 (dotted lines) and 20 November 2013 (solid line). Dashed lines outline the band of frequencies used in the inversion.

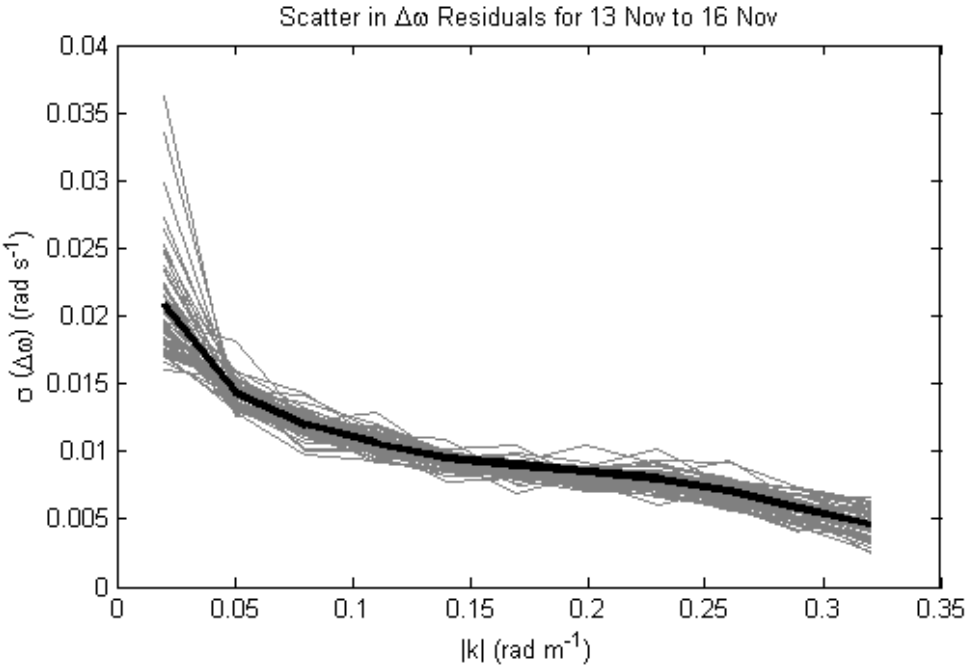

Figure 2.15 – The scatter of the Doppler shift residuals after azimuthal averaging, representing the standard deviation of the Gaussian noise $\Delta\omega'(k)$. The black line indicates the time average of the grey profiles, which span data collected from 13 Nov 2013 to 16 Nov 2013.

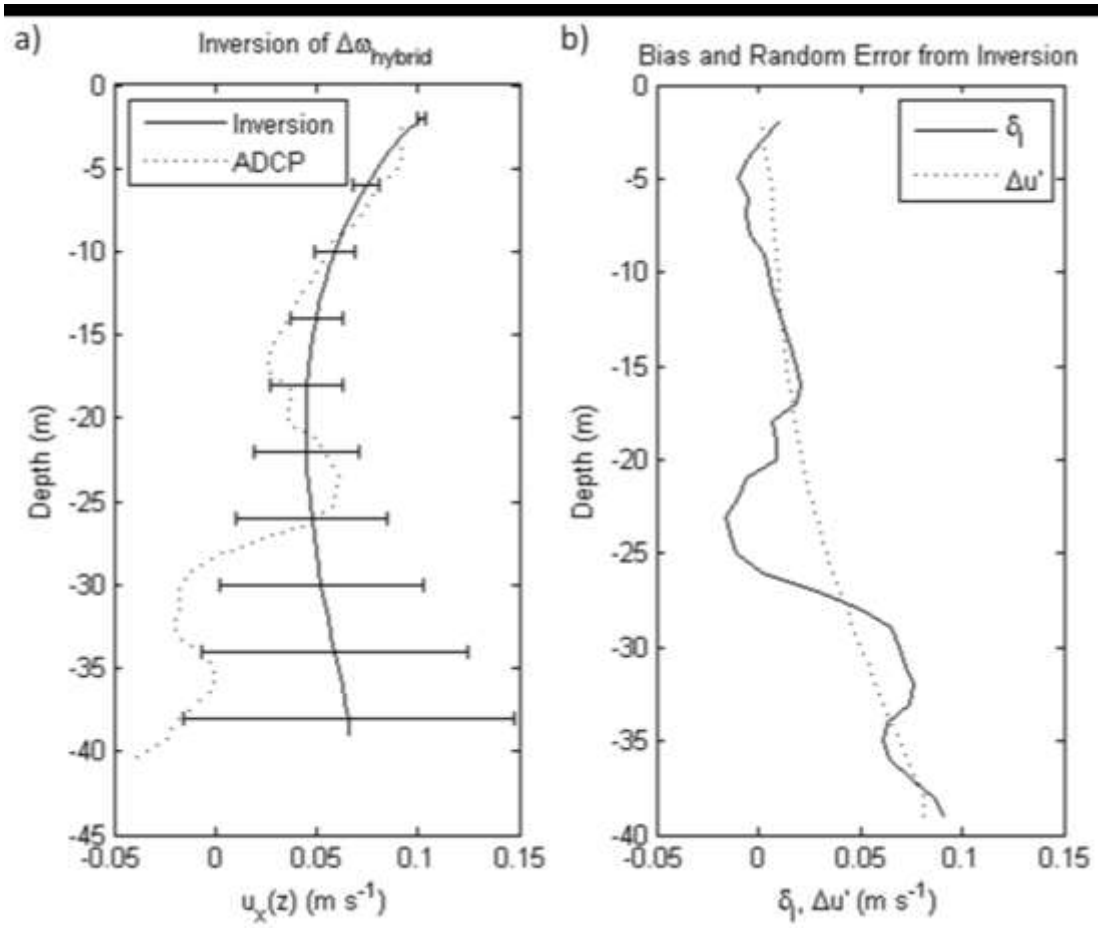

Figure 2.16 – Average (solid) and standard deviation (error bars) of the iterative inversion of $\Delta\omega_{hybrid}$ compared to the ADCP current profile (dotted) on 000 UTC 15 Nov 2013 (a). The average bias (solid) and standard deviation (dotted) represent the error constituents $\delta_I(z)$ and $\Delta u'(z)$, respectively (b).

Chapter 3
Observations of Wind-Driven Current Shear from the Inversion of X-Band Backscatter

Abstract

The inversion of depth-current profiles from X-Band observations of the wavefield have been shown to agree with concurrent ADCP observations (Chapter 2). However, the inversion also supplies current information within the very near-surface layer (z>-2m), outside of the range of the ADCP. Furthermore, the exponential form of the inversion suggests that waves are more sensitive to the current structure in this regime. Without secondary current measurements, inversion results must be compared to near-surface current models. This section compares inverted current profiles in the upper 4 m with results of models of near-surface currents. The presence of internal waves is observed using processing of X-Band backscatter as well as temperature measurements. The reaction of the near surface current shear to the combination of wind and internal wave forcing is shown to be qualitatively consistent with linear internal wave propagation. In the absence of internal waves, currents are compared to wind stress measurements and model results of wind-driven currents. Agreement with wind stress measurements is shown to be best when the roughness length, z_0, is one half the rms wave amplitude. Current profile observations are shown to agree with the well-established concept of a shallow wave-enhanced region of lower current shear above a deeper logarithmic layer. In agreement with other findings, the transition between the two layers

is shown to occur between $7.5z_0$ and $10z_0$. The results show that the inversion methods developed in the previous chapters provide valuable current shear information in the wave-enhanced regime in which wave motion makes it difficult to measure currents via well-established in situ methods.

3.1 Introduction

The previous chapters have shown that, under the favorable wind and wave conditions, current-depth profiles $\mathbf{u}(z)$ can be accurately estimated from the inversion of X-Band backscatter. The inversion scheme developed in Chapter 2 estimates $\mathbf{u}(z)$ from the integral relationship developed by Stewart and Joy (1974)

$$\hat{\mathbf{u}}(k) = 2k\int_{-\infty}^{0} \mathbf{u}(z)e^{2kz}dz \tag{1}$$

The integral was discretized using the Gauss-Legendre method to the sum

$$\frac{2\hat{\mathbf{u}}(k)}{k/k_0} \approx \sum_{i=1}^{n}\left(\frac{1}{2}\xi_i + \frac{1}{2}\right)^{\frac{k}{k_0}-1}\mathbf{u}(z_i)w_i \tag{2}$$

$$\xi = 2e^{-2k_0 z} - 1 \tag{3}$$

where n is the Legendre order, k_0 is the reference wavenumber (Ha 1979), and ξ_i and w_i are the tabulated zeros and weights of the Legendre polynomials (Golub and Welsch 1969; Cohen 2007). The solutions of the inversion are therefore defined at the depths z_i, which, for $n=30$ and k_0=0.035 rad m^{-1} used in Chapter 2, range from approximately -60 m to -0.02 m. Furthermore, the uneven distribution of z_i from (3) leads to more solutions

at shallower depths, with one third of them being shallower than -2 m. This means that a large portion of the current information supplied by the inversion technique is contained within the near-surface layer above the shallowest ADCP bin. Although this means that it is difficult to validate the current inversion results with secondary observations, these current estimates have the potential to model an important measurement gap for near-surface interaction studies. Without direct current measurements, a comparison of inversion results must rely on existing models of wind-driven currents in the near-surface region. Because this section focuses on the wind-induced near-surface currents, only the inversion result in the direction of the wind will be used, hereafter notated $u(z)$.

Because of the difficulty of making direct measurements of currents in the wave-affected layer of the ocean, modeling of the near-surface currents and dissipation has a long history. Though different models employ turbulence closure schemes differently, the basic structure is similar (e.g. Thompson and Turner 1975; Kundu 1980; Weber 1983; Craig and Banner 1994). This section outlines the work done by Craig and Banner (1994) to develop a model of the near surface layer that includes effects of currents and waves . Though many modifications of this model have been made (e.g. Terray et al. 1996; Umlauf et al. 2003; Umlauf and Burchard 2003), the Craig and Banner model supplies a well-accepted fundamental structure of the near surface currents (Figure 3.1a).

Following the model used by Craig and Banner (1994), the one-dimensional ocean model (e.g. Ekman 1905) simplifies the full momentum equations in the downwind and cross-wind to

$$\frac{\partial u}{\partial t} - \frac{\partial}{\partial z}(A\frac{\partial u}{\partial z}) = fv$$
$$\frac{\partial v}{\partial t} - \frac{\partial}{\partial z}(A\frac{\partial v}{\partial z}) = -fu \tag{4}$$

respectively, where A is the eddy viscosity. Craig and Banner (1994) used the level 2 1/2 turbulence scheme developed by Mellor and Yamada (1974, 1982), under which the eddy viscosity is represented as

$$A = lqS_M \tag{5}$$

where l is the turbulent length scale, q is the turbulent velocity scale, and S_M is a model constant. The turbulent velocity is defined by $b = q^2/2$, where b is the TKE density. The equation for b is

$$\frac{\partial b}{\partial t} - \frac{\partial}{\partial z}(lqS_q\frac{\partial b}{\partial z}) = lqS_M\left(\left(\frac{\partial u}{\partial t}\right)^2 - \left(\frac{\partial v}{\partial z}\right)\right) - \varepsilon \tag{6}$$

where ε is the dissipation and S_q is a model constant. Taylor (1935) showed that, by dimensional arguments,

$$\varepsilon = q^3/Bl, \tag{7}$$

where B is a constant. The model constants (S_M, S_q, B) are found empirically (Mellor and Yamada 1982).

Finally, the turbulent length scale must be defined. Observations in the laboratory and ocean suggest that the turbulent length scale decays linearly with depth (e.g.

Thompson and Turner 1975; Hopfinger and Toly 1976; Hannoun et al. 1988; Cheng and Law 2001), or

$$l = L(z_0 - z) \tag{8}$$

where z_0 is the *roughness length* and L is the proportionality constant. This generic model of the turbulent length scale is used for many models of the upper ocean, with the value of L ranging between 0.05 and 0.4 (Mellor and Yamada 1982; Wilcox 1988; Rodi 1987; Craig and Banner 1994; Umlauf and Burchard 2003).

As a first approach to modeling, the currents are assumed to behave similarly to the wind blowing over the ocean surface in a classic "law of the wall" formulation. By assuming the system is in steady state, the first terms of (4) and (6) become zero. The effect of the surface waves is assumed to be only that of a rough surface under which the current flows. Without an additional source of TKE, (6) becomes a balance between shear production of TKE and its dissipation. The current profile is then the classic logarithmic profile

$$u(z) = U_{\log} - \frac{u^*}{\kappa}\log(z_0 - z) \tag{9}$$

where $U_{\log}$ is an additive constant. The friction velocity u^* is related to the shear stress τ in the logarithmic layer through

$$u^* = \sqrt{\frac{\tau}{\rho_w}} \tag{10}$$

where ρ_w is the density of water.

Current profile observations confirm the presence of a logarithmic relationship, but only below a surface layer in which the injection of TKE by surface waves is significant (e.g. Kitaigorodskii et al. 1983, Thorpe 1984, Terray et al. 1996). As a first approach, Craig and Banner (1994) assume that TKE injected by the wavefield is balanced by its dissipation. That is, the shear production of TKE is zero. They model the TKE injected by the wavefield as a boundary condition of the TKE flux proportional to $u*^3$. They find the current profile in the near-surface layer, where rotation can be neglected, is

$$u = U_{pwr} - 3r^4 \alpha^{-1/3} u* \left(\frac{z_0 - z}{z_0} \right)^p \tag{11}$$

where $r = 1$ was derived from model constants and U_{pwr} is an additive constant . α is the *wave energy factor* related to the wave age (Drennan et al. 1992), though Craig and Banner (1994) suggest $\alpha = 100$ is appropriate for a wide range of wave ages. For the model constants used by Craig and Banner (and Mellor and Yamada 1982), they found that $p = 0.8$. This result implies the effect of the additional TKE from the wavefield acts to decrease the amount of current shear in the near-surface layer.

By neglecting rotation in the wave enhanced layer, the momentum equation in the wind direction simplifies to

$$A \frac{\partial u}{\partial z} = const.$$

This, along with (5), (7), and (8), describe the relationship between the structure of TKE dissipation ε and the velocity profile. Specifically, if $\varepsilon \propto z^{n_\varepsilon}$ and $u \propto z^{p}$, then

$$p = -(n_\varepsilon + 1)/3 . \tag{12}$$

From the Craig and Banner (1994) result, therefore $n_\varepsilon = -3.4$. This is consistent with observations of dissipation decay rates in the wave-enhanced layer, which span the range $-4 < n_\varepsilon < -2$ (Drennan et al. 1992, Anis and Moum 1992, Terray et al. 1996, Gemmrich and Farmer 2004). Using (12), this range of dissipation decay rates suggests that the order of the power law decay of the current profile falls within the range $1/3 < p < 1$.

Craig and Banner (1994) then solved the full model, which involved the balance between TKE transport from the wavefield, shear production of TKE, and the dissipation of TKE. The resulting current profile consisted of a two layer structure, with a shallow wave enhanced layer exhibiting a power law profile, and a deeper layer that satisfied the logarithmic profile. This two layer structure is consistent with other models and observations in this regime. Craig and Banner (1994) find that the transition between these two layers occurs at a depth of -6z_0. Though this transition depth varies between models and observations, it generally lies between -5z_0 and -10z_0 (Agrawal et al. 1992; Thorpe 1992; Craig and Banner 1994; Terrey et al. 1996).

The selection of z_0 has been shown by others to have a large effect on the estimate of the decay rates from model results, but it is still unclear what value z_0 should take. In fact, the choice of the value of z_0 by other studies varies by multiple orders of magnitude.

One common approach is to approximate z_0 using the an adaptation of Charnock's (1955) formula

$$z_0 = a\frac{u^{*2}}{g} \tag{13}$$

where a is a constant (e.g. Craig and Banner 1994; Terray et al. 1996; Melsom and Sætra 2004). The value of a, however, ranges multiple orders of magnitude from 10^2 to 10^5 among studies using both model results and observations (Bye 1988; Cheung and Street 1988; Terray et all. 1996; Stacey 1999; Melsom and Sætra 2004). Although it is traditionally termed the *roughness length* because of its appearance in the law-of-the-wall (9), Umlauf and Burchard (2003) noted z_0 is more closely related to the length scale of the injected turbulence by the wavefield. Similarly, because $u^{*2}/g \propto H_s$ (Agrawal et al. 1992), the (13) can be thought of as a scaling between z_0 and the wave height. Its relationship to the depth of the wave-enhanced layer, as well as the injected turbulence length scale, suggests its relationship to wave amplitude is intuitive (Thorpe 1992). This has led to range of approximations scaling with significant wave height from $0.25H_s < z_0 < 2H_s$ (Thorpe 1992; Terray et al. 1996; Soloviev and Lukas 2003). Because of the historic uncertainty in the assignment of z_0, this work investigates the effect of multiple z_0 values ranging from $H_s/16 < z_0 < H_s/4$.

Although the expressions (9) and (11) do not explicitly depend on wind speed, u^* is related to the stress at the surface (as is z_0, though more indirectly through H_s). The momentum flux from the wind to the water enters the wavefield and is then transferred into the currents, primarily via breaking (Phillips 1977). Although some momentum

contributes to the building of the wavefield, most it is transferred to the currents locally (Melville 1996). Assuming that the momentum flux contributing to wave generation is negligible, the wind stress is approximately equal to the shear stress in the water. Using (10) on either side of the air-sea interface, therefore

$$u*_{water} \approx u*_{air} \sqrt{\frac{\rho_{water}}{\rho_{air}}} \tag{14}$$

This expression provides a useful means to compare estimates of friction velocities made on either side of the air-sea interface.

The results of the Craig and Banner (1994) model assume the surface layer is unstratified. Some expansions of this model (e.g. Mellor and Yamada 1982; Umlauf et al. 2003) account for buoyant production of TKE with an additional term in the TKE balance. The effect of internal wave motion, however, is not taken into account. The reaction of surface currents to the propagation of a linear internal wave results in horizontal flow that oscillates with the frequency of the passing wave (Figure 3.1b) (Phillips 1966). The presence of internal waves, therefore has the potential to affect the vertical structure of the near surface currents. Specifically, if an internal wave is propagating with the wind, the current above the crest of the thermocline heave travels opposite the wind and therefore acts to increase the current shear. The current over the trough of the thermocline heave, on the other hand, travels with the wind, leading to less current shear than in a purely wind-driven flow.

The goal of this work is to compare the current inversion results in the near-surface layer (z>-3 m) with various models. First, the effect of internal waves on the vertical structure of currents estimated by the X-Band inversion is investigated. Then, for times during which the near surface layer is unstratified, the current inversion result will be compared to the Craig and Banner model. Specifically, the inverted current profiles will be compared to a logarithmic layer (9) and a power law profile (11). Using both of these models, the friction velocity $u*$ will be estimated and compared to $u*_{water}$ computed using (14) from concurrent wind stress measurements.

3.2 Observations

The inversion results of the previous chapter showed a strong dependence on the wave spectrum (see Figure 2.11), specifically on the presence of low frequency wave energy. For example, on 20 November 2013, the wave energy is primarily contained in the higher frequency portion of the inversion range (Figure 3.2). The increased noise resulting from less energy in lower frequencies results in a higher RMS error for this time period. Raising the lower limit of the wavenumber band of the inversion process removes this effect at the cost of raising the inversion's effective depth above -20 m. This raising of the inversion's effective depth is a result of removing Doppler shift measurements of longer waves, which contain more information about deeper currents than do shorter waves. As shown in Chapter 2, lower wavenumber Doppler shifts also contain the majority of the measurement noise (Figure 2.15). The range of wavenumbers to use in the inversion, therefore, must balance 1) the location of energy within the wave spectrum, 2)

the required effective depth of the inversion, and 3) the noise contamination from lower wavenumber observations.

The periodogram measured by the moored wave buoy (Figure 3.2) shows wave energy was variable within the wavenumber range used in the inversion, suggesting a time-dependent band-passed wavenumber range could be selected for the inversion. With a focus on near-surface currents, a shallower effective depth does not affect the analysis of this section, which means the effect of removing low wavenumbers would be minimal. However, noise in the high wavenumbers introduced by lower wave energy in the wave spectrum has a smaller effect on the inversion than the noise in the low wavenumber Doppler shift observations. This means it is more advantageous to include high wavenumber observations in the inversion, regardless of their spectral energy. Therefore, a variable high-pass wavenumber range was defined using the wave energy spectrum observed by the moored wave buoy (white solid line in Figure 3.2). The current inversion of Chapter 2 was then re-calculated within this new wavenumber range (Figure 3.3). Depths below which the inversion becomes unstable have been removed. The effect of the wavenumber range truncation is most obvious on 20 Nov 2013, when the inversion result becomes unstable below a depth of approximately 8 m.

Similar to Chapter 2, the depth-averaged rms error was used as an error metric, defined by

$$RMSE = \sqrt{\left\langle \left(u_{inverted} - u_{measured} \right)^2 \right\rangle}$$

where $\langle\ \rangle$ signifies a depth-average. Because of the shallower effective depth of the high-passed inversion, the depth-average rms error was calculated for the top 8 m instead of the 20 m average used in Chapter 2. Results show the new inversion yields smaller error in surface current estimates during times of low wave energy in low frequency bands (Figure 3.3c). To isolate the current shear structure of the inversion results from the depth-uniform tidal component, the current velocities were referenced to their values at a depth of -4 m (Figure 3.4c).

As a part of the SoCal2013 campaign, collaborators at Scripps Institution of Oceanography measured water temperature using a string of thermistors suspended from R/P FLIP as well as wind stress using a sonic anemometer (Figure 3.4a-b).

3.3 Results

The vertical structure of the temperature measured from FLIP shows signals that are consistent with propagating internal waves (Figure 3.4b). To confirm the presence of internal waves, the X-Band radar was used to observe their surface expression. The oscillating near surface currents resulting from internal wave propagation creates regions of convergence and divergence, which modulate the surface waves. Both X-Band and HF radar have been used in the past to observe this surface wave modulation (Alpers 1985; Watson and Robinson 1990). By averaging 400 consecutive marine X-Band backscatter scans (representing 10 minutes of data), contribution to the majority of the backscatter energy by the surface wavefield disappears. This leaves spatial structures that are coherent throughout the 10 minutes time period, including the surface modulation due to

internal waves (Figure 3.5). Other features visible in the averaged images include the large region of nearfield backscatter just upwind of FLIP (due to the wind-dependent directional asymmetry in the backscatter) as well as the reflection from the R/V Melville. Two of these time-averaged images taken one hour apart show the propagation of the internal waves.

These surface expressions of internal waves were observed throughout the first three days of the experiment, which is consistent with the thermocline heave seen in the temperature data. The most extreme thermocline heave occurred on 13 Nov 2013 (Figure 3.4b). At this same time, the current inversion results shows enhanced near-surface shear (Figure 3.4c). The surface expression analysis using the X-Band backscatter shows the internal waves propagating obliquely to the wind, with a component traveling in the down-wind direction (Figure 3.5). The increase in near-surface current shear during the thermocline heave seen on 13 Nov 2013 and the subsequent lack of shear (despite consistent wind forcing) are therefore consistent with the simple linear internal wave model (Figure 3.1b).

The temperature measurements suggest that internal wave influence on near-surface current shear was only significant from 13 Nov 2013 to 16 Nov 2013. This period was followed by a time period of low winds (Figure 3.4a) and therefore no current inversion results (Figure 3.3b). Beginning on 19 November 2013, wind speed increased sharply, generating high frequency wind-sea (Figure 3.2), which lead to the enhance current shear signal (Figure 3.4c). This behavior, along with the non-stratified temperature structure, suggest that a comparison between current observations and the

Craig and Banner model is appropriate for this time period. The structure of the wind-driven currents was therefore analyzed for the time period from 19 November 2013 to 22 November 2013.

The wind-current relationship was quantified using an estimate of the friction velocity u^* from functional fits to the logarithmic (9) and power law relationships (11). To estimate u^* from the logarithmic profile (9), the data were organized into the two terms $U_{\log} - u$ and $\log(z_0 - z)$, where U_{log} was chosen as the surface current. Following (9), a linear fit between the two terms provided the estimate of u^* (Figure 3.6a). To estimate u^* from the power-law relationship, (11) was reorganized to

$$\log(U_{pwr} - u) = p\log(z_0 - z) + \log(au^* z_0{}^p) \tag{15}$$

which is a linear relationship between $\log(U_{pwr} - u)$ and $\log(z_0 - z)$ with a slope of p and an intercept related to u^*. Again, by assigning U_{pwr} as the surface current, the data was reorganized to match (15). A linear fit therefore resulted in an estimate of u^* and p for each time point (Figure 3.6b). This analysis was done for the three choices of z_0 mentioned above.

The results of the power law fit show good agreement to the power law order found by Craig and Banner (1994) (Figure 3.7). The short time periods of large scatter in the p correspond to time periods of low high frequency wave energy (Figure 3.2). This leads to more noise in the inversion process in the high wavenumbers, which affects current estimates in the near surface region. The variation of z_0 within the range

$H_s/16 < z_0 < H_s/4$ appears to have a minimal effect on the power law order, resulting in an average difference in p of approximately 0.15. For all of the roughness lengths used, estimates of p are consistent with previous observations, falling within the range $1/3 < p < 1$ mentioned above. For each choice of z_0, p shows little dependence on wind speed, which is consistent with (11).

Friction velocity estimates from the functional fits were compared to $u*_{water}$, computed using (14) and wind stress measurements (Figure 3.8). The time series shows $u*$ estimates from logarithmic and power law fits agree to within 0.002 m s^{-1} of each other (Figure 3.8a). The time dependence of both estimates is similar and agrees well with the time dependence of the wind speed. The friction velocity estimated by the power law is more sensitive to changes in the choice of z_0. At the wind peak, for example, the range in z_0 leads to a $u*$ range of 0.007 m s^{-1} for the power law and 0.003 m s^{-1} for the logarithmic fit. The magnitudes of the friction velocity estimates are closest to $u*_{water}$ for $z_0 = H_s/8$, or when the roughness length is one half of the rms wave height. Furthermore, for this z_0, the two $u*$ estimates from current measurements agree with each other to within 10^{-4} m s^{-1}. The scatter comparison of $u*$ estimated from the power law fit and $u*_{water}$ shows good agreement between the two (Figure 3.8b). Large discrepancies in the time series and scatter plot occurs during the time periods of low wave energy in the high frequency band as mentioned above.

To collapse the observations to be compared with (9) and (11), the friction velocity was used to normalize the current profiles. The new normalized current profiles are

$$\bar{u}_{\log} = \frac{U_{\log} - u}{u*} = \frac{1}{\kappa}\log(z_0 - z)$$

$$\bar{u}_{pwr} = \frac{U_{pwr} - u}{u*} = 3r^4\alpha^{-1/3}\left(\frac{z_0 - z}{z_0}\right)^p$$

$$\bar{u}_{obs} = \frac{u(z=0) - u}{u*}$$

The results of the previous section suggest the appropriate friction velocity estimate to use for this normalization is that for $z_0 = H_s/8$ (Figure 3.8). The $u*$ used to normalize the observed current profiles was chosen as that estimated from the power law fit, though, as mentioned above, the logarithmic result could be used with a similar result. The normalized observations were plotted as a time-averaged $\bar{u}_{obs}$ with error bars representing one standard deviation (Figure 3.9). Horizontal variations in the profiles are due to the selection of the additive constants in (9) and (11), chosen to highlight the similarity of the profiles (Craig and Banner 1994). The results are plotted against z/z_0 so that the numerical result found by Craig and Banner (1994) could be directly compared. This comparison shows good agreement; they both display a region of weaker shear near the surface and logarithmic behavior at depth. The depth at which this transition occurs is between $7.5z_0$ and $10z_0$, which is consistent with the range found by others (Agrawal et al. 1992; Thorpe 1992; Craig and Banner 1994; Terrey et al. 1996).

3.4 Discussion

These results have shown that the current inversion technique developed in Chapter 2 supplies current estimates within 4 m of the surface that are consistent with models and other observation within this layer. The observation time period was separated into two intervals. During the first half of the experimental period, we observed the presence of internal waves and their resulting current structure. Conditions during the second half of the experiment allowed for a comparison of current observations to the Craig and Banner (1994) model and to wind stress measurements.

Many modifications have been made to the Craig and Banner model to more accurately represent the surface boundary layer. For example, the effect of the intermittency of wave breaking has been investigated using various approaches (Melsom and Sætra 2004; Sullivan et al. 2004). Although these studies found that intermittent breaking can have an effect on the vertical current structure, the fundamental two-layer structure of the Craig and Banner (1994) structure remains consistent. Melville and Matusov (2002) showed that, for wind speeds less than 15 m s^{-1}, the area of active (air-entraining) breaking makes up at most O(1%) of the sea surface area. For this study, with wind speeds less than 12 m s^{-1}, these large breaking events are expected to be even less frequent. Furthermore, Melsom and Sætra (2004) conclude that the effect of intermittent wave breaking leads to an increase in the surface current velocity by at most a few percent. Therefore, the use of the Craig and Banner model for the comparison shown here was appropriate. However, in future applications of the inversion process to observe near surface currents, intermittent wave breaking may play a larger role.

Errors in the inverted currents have been discussed in the previous chapter. The most relevant source of error pertaining to this section, however, is the effect of enforcing a smooth current profile. This smoothness constraint of the inversion process can introduce unwanted bias by underestimating or overestimating neighboring current estimates to minimize curvature. Although this potentially changes the shape of the current profile and could be one source of the near-surface deviation between the observations and the Craig and Banner model (Figure 3.9), the high density of current estimates near the surface minimizes its effect.

An additional potential source of error in the current measurement is the linearization of boundary conditions in the derivation of (1) (Stewart and Joy 1974). This linearization replaces the true water level with the mean water level, neglecting fluctuations between crests and troughs. Although Stokes drift effects are removed from the inverted currents used here (see Chapter 2), differences in mean current shear across the mean water line are not. It has been shown the dissipation is largely enhanced above the mean water line (Stewart and Grant 1962; Gemmrich and Farmer 2004). Although this effect is not directly solved for due to the linearization, current shear in the wave crests does affect the observed Doppler shifts of the wavefield, which in turn affects the results of the current inversion. The linearization of (1), therefore, collapses the information of the wave crests to the mean water level, potentially overestimating the current shear at the surface. This effect could be one cause of the time-dependence of the estimation of p (Figure 3.7), as well as the small increase in current shear seen in the upper 40 cm (Figure 3.9).

It is worth noting that by applying the variable high pass filter to the wavenumber range used for inverting currents for this process, the relationship between this wavenumber bandwidth and the effective depth of the inversion could be approximated. The wavenumber bandwidth varied between the full range (0.05 rad m^{-1}<k<0.3 rad m^{-1}) and the minimum range on 1800 19 Nov 2013 (0.12 rad m^{-1}<k<0.3 rad m^{-1}). The range of effective depths between 20 m and 8 m suggests that the inversion process is able to estimate currents to a depth of approximately $k_{\min}^{-1}$, where $k_{\min}$ is the smallest observed wavenumber. As alluded to in Chapter 2, this is twice the depth of the current estimate made under the linear current profile assumption (See Figure 2.13).

A potential extension of using the inversion method of Chapter 2 to estimate near-surface currents is to use a wavefield measurement method with the ability to observe higher wavenumbers than the processing of X-Band radar. The largest wavenumber used in this inversion was 0.32 rad m^{-1}, corresponding to a wavelength of approximately 20 m. From (1), the e-folding depth of this wave is -1.6 m. A collection of higher wavenumber waves would therefore be more sensitive to fluctuations in currents in the upper 2 m.

3.5 Conclusion

The response of near-surface currents to internal waves and wind forcing was shown to be well captured by the current inversion technique introduced in Chapter 2. Marine X-Band backscatter images were processed to observe the surface signature of propagating internal waves. Temperature measurements supplied details of the depth

dependence and phase of these internal waves. The reaction of the surface currents to the rise and fall of the thermocline was shown to be well captured by the inverted currents.

Later in the experiment, when the temperature structure was non-stratified, current observations in the top 4 m were compared to wind stress measurements and the Craig and Banner model of wind-driven current shear. Friction velocities in the near-surface region were estimated using functional fits to power law and logarithmic profiles suggested by Craig and Banner (1994). These friction velocities were shown to agree well with those derived from concurrent wind stress measurements for a choice of roughness length of $H_s/8$, or one half the rms wave height. With this value of roughness length, current observations were shown to agree with the well-accepted two-layer model of wind-driven currents. Specifically, a shallow wave-enhanced layer was observed in which the effect of waves lead to a reduced in current shear than predicted by a classic law-of-the-wall profile. Below this wave-enhanced layer, the current structure approached a logarithmic profile. The transition between the two layers occurred at a depth of approximately -1.5 to -2 m. Using the approximation of z_0 as ½ the rms wave amplitude, this transition depth was in agreement with previous estimates of $O(10z_0)$ (Agrawal et al. 1992; Thorpe 1992; Craig and Banner 1994; Terrey et al. 1996).

The overall agreement between current observations and the predicted current response to wind and internal wave forcing shows that the inversion method developed in the previous chapters provides valuable current information in a regime in which traditional in situ current measurement techniques are contaminated by wave motion.

Furthermore, with the temporal and spatial averaging inherent in the inversion process, current observations are more statistically robust than traditional point measurements.

3.6 Acknowledgements

The author would like to thank Ken Melville for his valuable insight and his group at Scripps Institution of Oceanography for the collection of wind stress measurements. Chapter 3 is currently being prepared for submission for the publication of the material. Campana, Jeffrey; Terrill, Eric J. Observations of Wind-Driven Current Shear from the Inversion of X-Band Backscatter. The dissertation author was the primary investigator and author of this material.

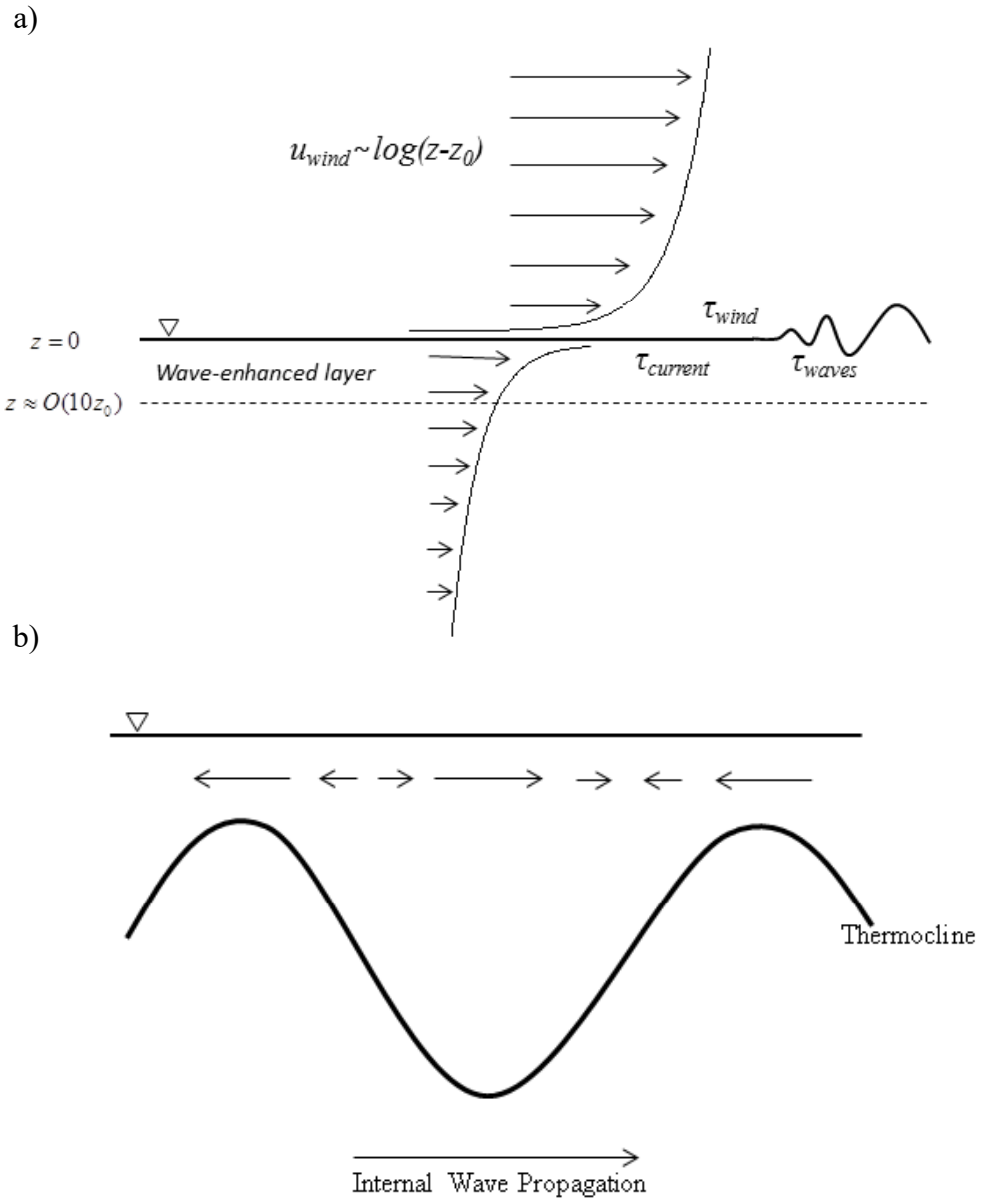

Figure 3.1 – a) A schematic describing wind-generated currents. Momentum flux from the wind to the water τ_{wind} is partitioned into building the wavefield (τ_{waves}) and local current generation ($\tau_{current}$). Current structure in the shallow wave-enhanced layer is affected by wave motion, whereas below this region, currents approach the classic law-of-the-wall behavior. b) A schematic describing the effect of a propagating linear internal wave on surface currents. The current oscillation leads to surface regions of convergence and divergence, which are visible in the X-Band backscatter.

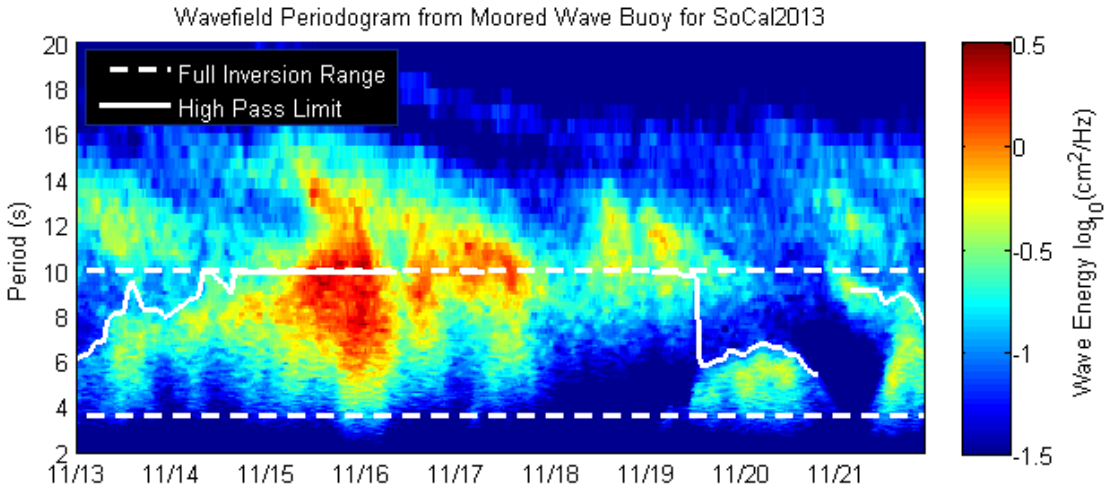

Figure 3.2 – The periodogram measured by the moored Datawell buoy with dashed lines outlining the full range of wavenumbers used in the inversion in Chapter 2. The solid white line defines the lower limit of the high-passed wavenumber range used for the current inversion in this chapter.

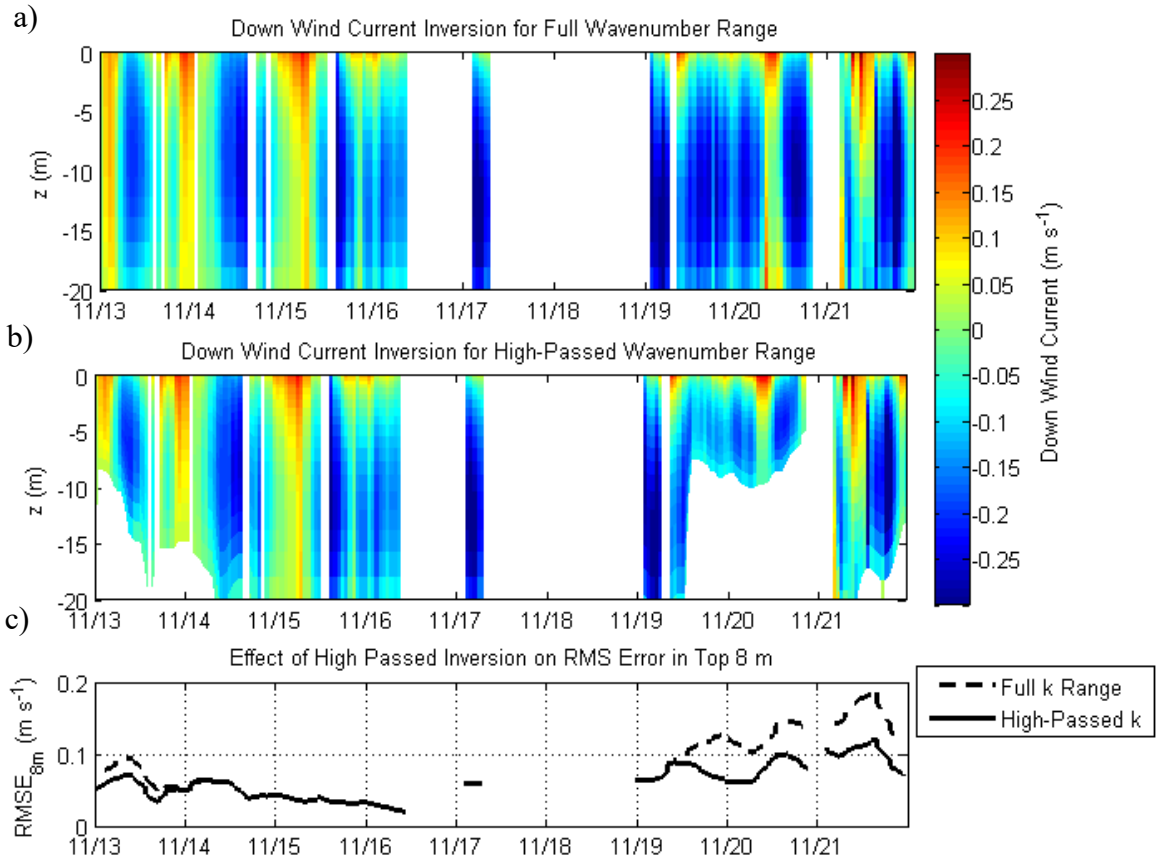

Figure 3.3 – a) The down-wind current inversion using the full range of wavenumbers as in Chapter 2. b) The down-wind current inversion using the variable high-passed wavenumber range shown in Figure 3.2. c) The 8 m depth-average rms error for the full-range inversion (dashed) and the truncated inversion (solid).

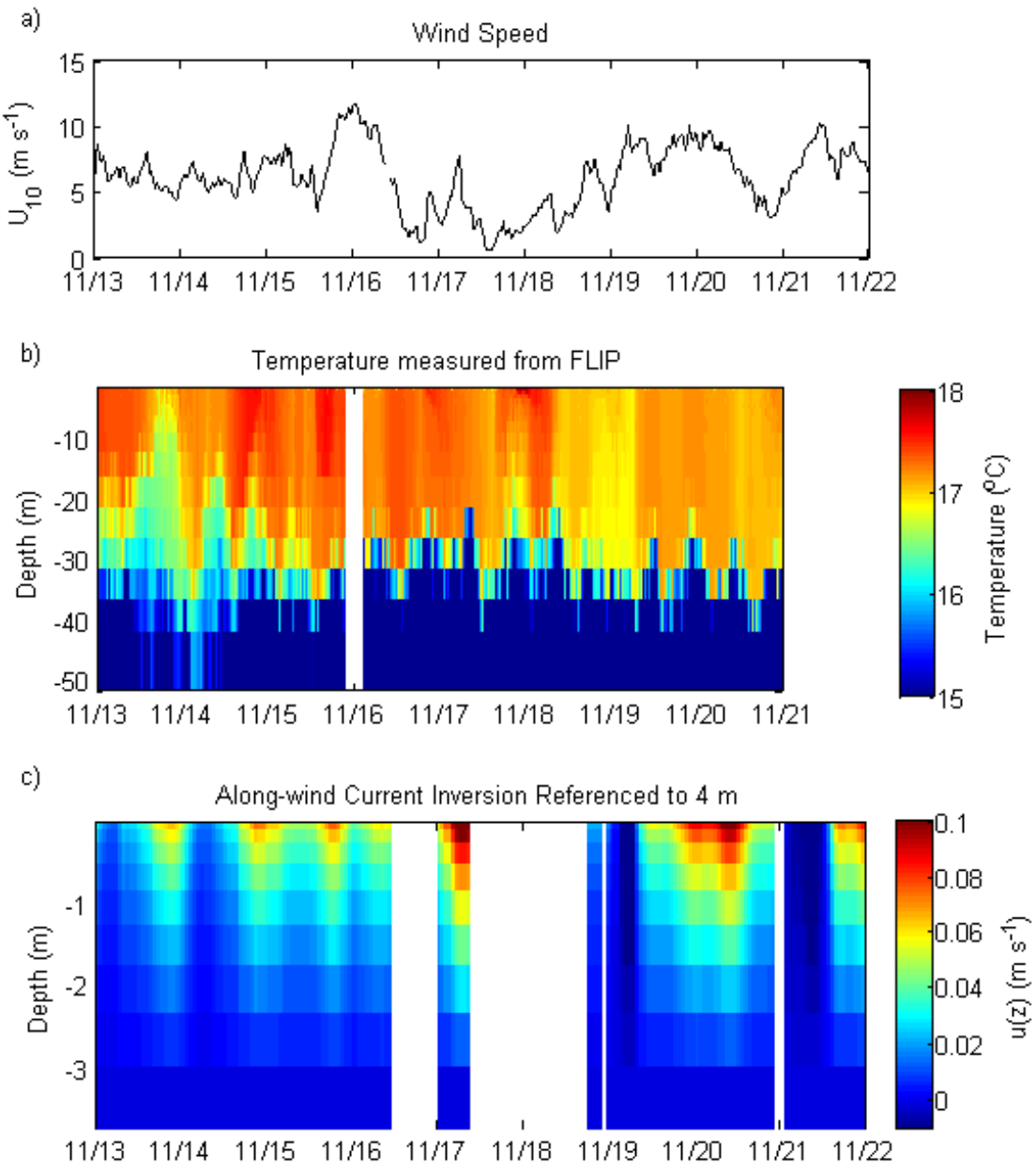

Figure 3.4 –a) The wind speed measured 10 m above the sea surface from R/P FLIP. b) Temperature measurements made from R/P FLIP during Socal2013, where warm colors are denote higher temperatures and cool colors denote lower temperatures. Propagating structures during the first few days of the experiment indicate the presence of internal waves. c) The result of the current inversion in the down-wind direction referenced to 4 m to remove the depth-uniform current signal.

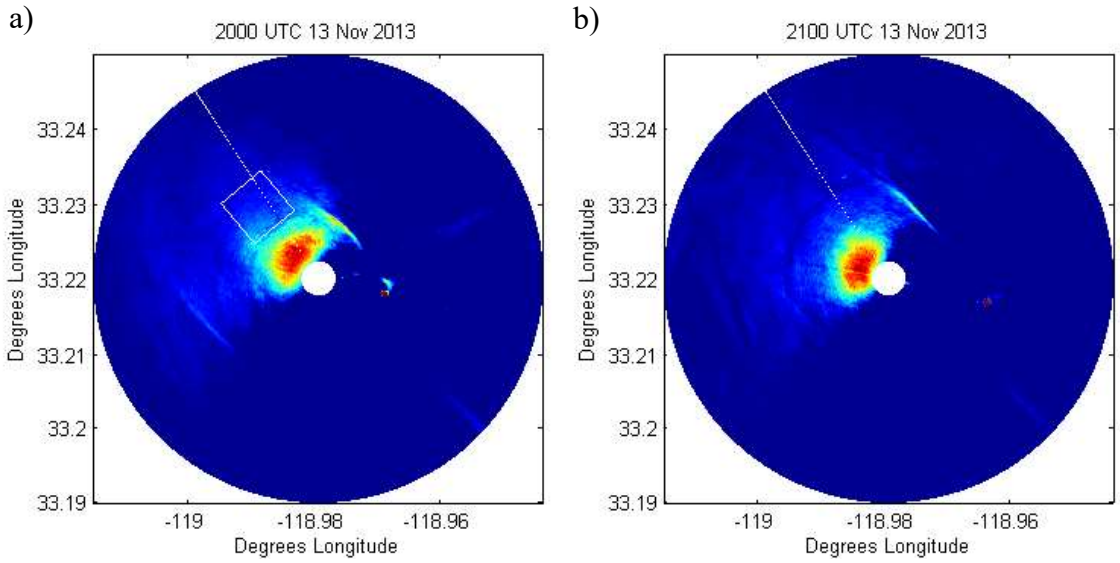

Figure 3.5 – The surface expression of an internal wave viewed by the X-Band radar. Each image represents the average of 400 consecutive scans (10 minutes of data), with hot color representing strong backscatter energy and cool colors representing weak backscatter. The two images are separated by one hour to show the advance of the internal wave.

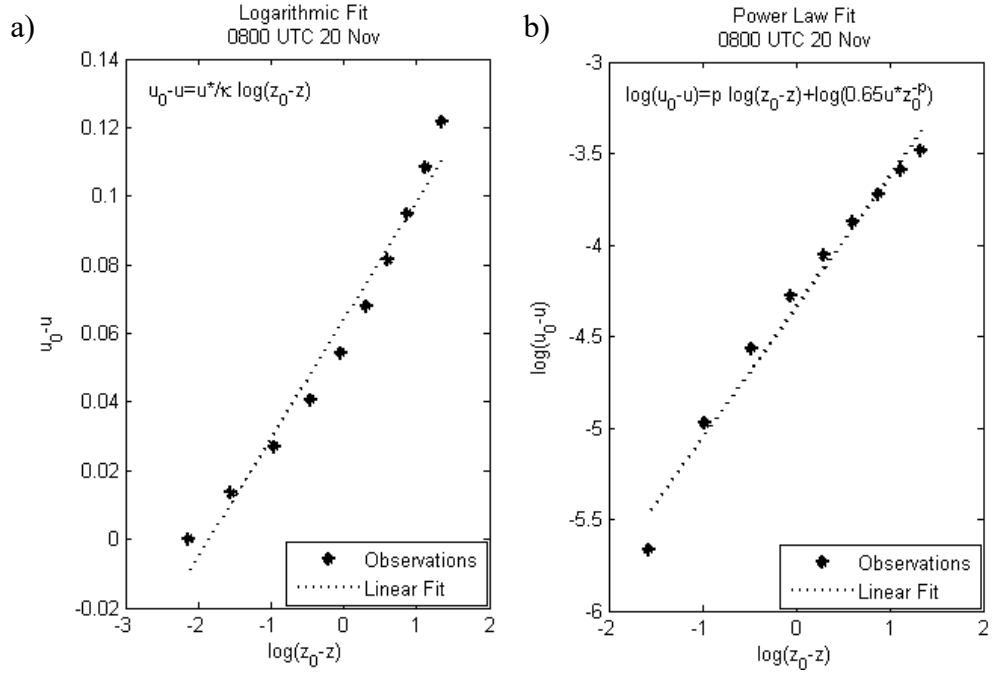

Figure 3.6 – Examples of linear fits to estimate the friction velocity from (a) logarithmic and (b) power law profile assumptions. This example was taken on 0800 UTC 20 Nov.

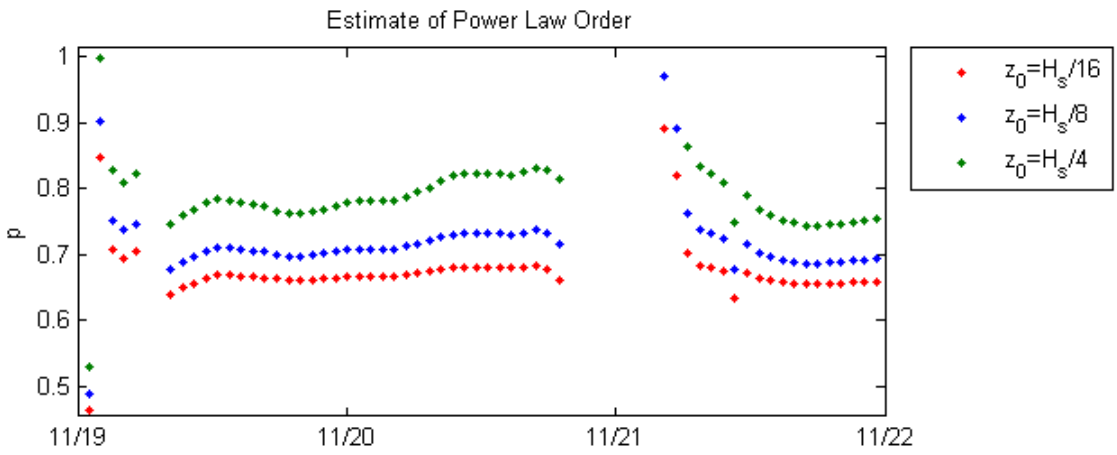

Figure 3.7 – The order of the power law fit for various roughness lengths, estimated by the linear fit as in Figure 3.6b.

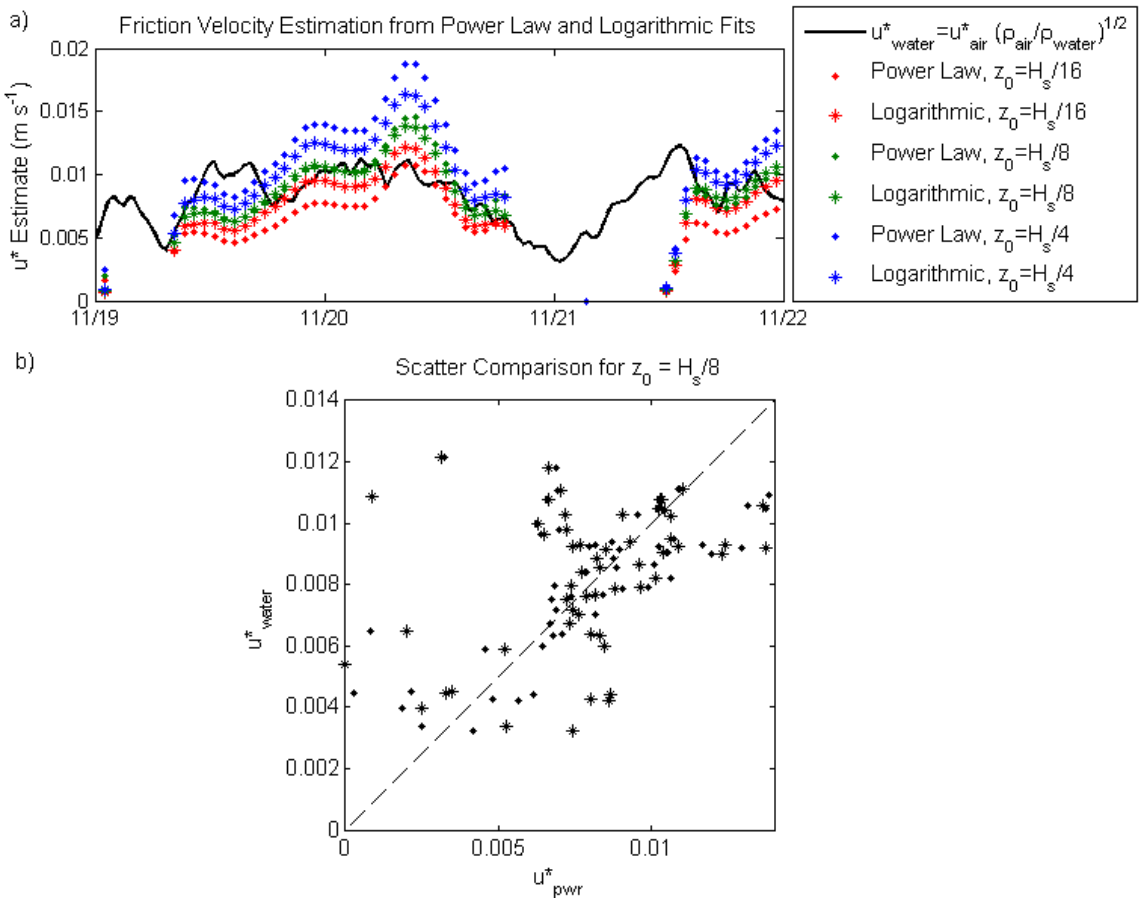

Figure 3.8 – a) Time series of the estimated friction velocity for power law (dot) and logarithmic profile (star) functional fits for varying roughness lengths (colors). The black line represents u^*_{water} calculated from wind stress measurements using (14). b) Comparison between friction velocity calculated from wind stress measurements (u^*_{water}) and u^* estimated from both the power law (dot) and logarithmic (star) for $z_0=H_s/8$. The dashed line indicates the 1:1 line, where $u^*=u^*_{water}$.

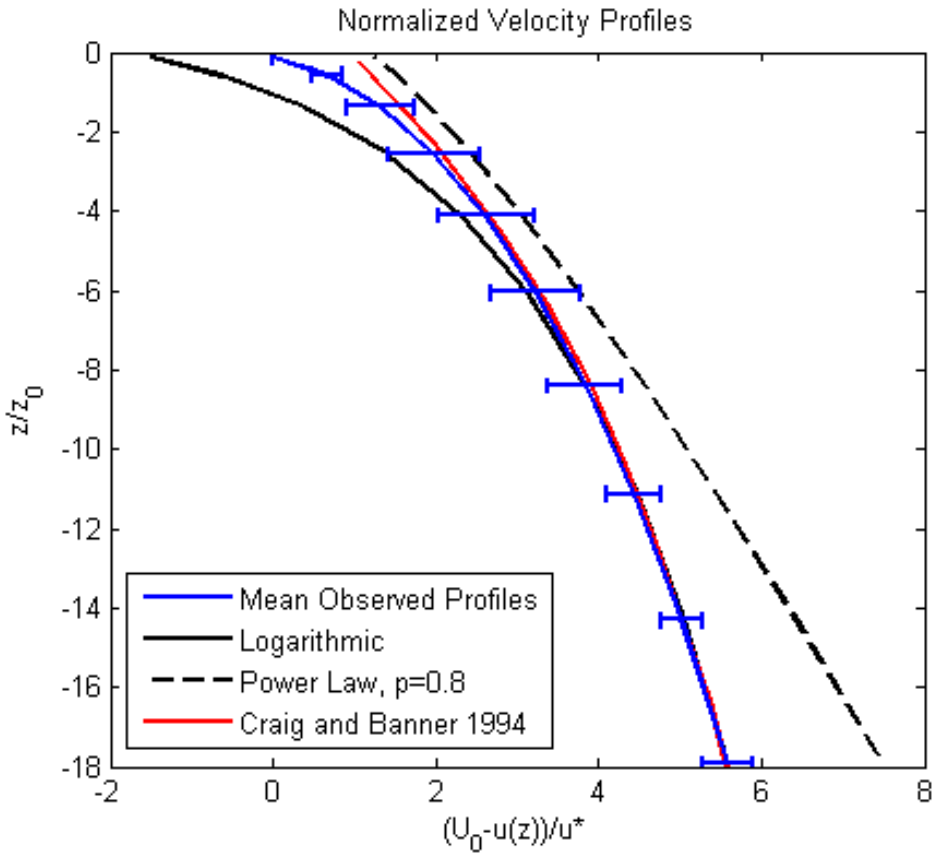

Figure 3.9 – The observed near-surface current profiles normalized by u^* (blue) compared with the power law with a power of 0.8 (dashed) and the logarithmic profile with κ=0.4 (black). Error bars indicate one standard deviation. The red line is the result of the Craig and Banner (1994) model.

Concluding Remarks

This dissertation has thoroughly investigated the effect of depth-dependent currents on the wavefield, and how this effect can be leveraged to extract current shear information from wavefield observations. Specifically, inversion techniques were developed to estimate depth-current profiles from wavenumber-dependent Doppler shifts derived from marine X-Band radar backscatter in moderate and deep water environments.

The moderate-depth inversion was applied to observations of the energetic region within the Mouth of the Columbia River. The time and depth behavior of the inverted currents were shown to be consistent with ADCP current measurements. This agreement was highlighted by the direction reversal of deeper currents preceding that of shallow currents during tidal transition, a behavior consistent with salt wedge propagation. This result shows the inversion technique holds promise for future applications to the study of tidally-driven two layer flows containing a large amount of current shear. Because of its use of remote sensing, this method also offers the advantage of being applied in otherwise inaccessible areas (e.g. due to hazardous conditions).

The expansion of the newly developed inversion technique to a deep water environment overcame the obstacles of lower current velocities and current direction variability. Results of the deep water current inversion were shown to perform with similar success to other remote sensing techniques at near the surface. However, the inversion was able to estimate current velocities with this same accuracy down to a depth of approximately 20 m. More generally, this work has shown that the maximum depth of

the inversion is approximately $k_{\min}^{-1}$, corresponding to twice the depth range offered by other radar-based current shear estimates.

Finally, the inversion process developed here was shown to provide estimates of the current profile within the top 2 m of the water column. In this very near-surface region, the current inversion successfully captured the reaction of the current shear to propagating internal waves. Current estimates in this surface layer also proved to agree well with models of wind-driven current shear, displaying a vertical structure comprised of a shallow wave-enhanced layer lying above a logarithmic region. Furthermore, the spatial averaging inherent in the processing of X-Band backscatter results in a more statistically robust current estimate than traditional point measurements. With a novel way of measuring currents in a region traditionally plagued by wave motion contamination, this method holds promise for future studies of air-sea and wave-current interactions.

Although this work focuses on the use of marine X-Band radar to make observations of the wavefield, the inversion process described here has the potential to be expanded for use with other wavefield observation methods. For example, optical methods have been shown to provide wavenumber-frequency information in a higher wavenumber range than that used here (e.g. Dugan et al. 2001). Simultaneous wavefield measurements from multiple sensors (e.g. X-Band, HF, and optical) could also be combined to extend the inverted wavenumber range, which would have an effect on the maximum depth of the inversion and the depth-resolution of the inversion. The denser field of inputs could also potentially constrain the inversion, allowing for the relaxation

of curvature constraints. This would result in the ability to better capture sharp variations in the depth-current profile.

The novel current estimation technique developed in this dissertation provides a valuable means of extracting current shear from X-Band backscatter. Results have shown this technique holds potential to address scientific and navigational concerns in both deep and moderate water depth. Furthermore, its modular design allows for potential extension for use with other wavefield measurement techniques.

Reference List

Agrawal, Y. C., E. a. Terray, M. a. Donelan, P. a. Hwang, a. J. Williams, W. M. Drennan, K. K. Kahma, and S. a. Kitaigorodskii, 1992: Enhanced dissipation of kinetic energy beneath surface waves. *Nature*, 359, 219–220.

Alpers, W., J. Schroeter, F. Schlude, H.-J. Mueller, and K. P. Kolterman, 1981b: Current Measurements by an L band Two-Frequency Microwave Scatterometer. *Radio Sci.*, 16, 93–100.

Alpers, W., Ross, D., and Rufenach, C., 1981a: On the Detectibility of Ocean Surface Waves by Real and Synthetic Aperture Radar. *J. Geophys. Res.*, *86*, 6481–6498.

Alpers, W., 1985: Theory of radar imaging of internal waves. *Nature*, 314, 245–247, doi:10.1038/314245a0.

Anis, A., and J. N. Moum, 1992: The Superadiabatic Surface Layer of the Ocean during Convection. *J. Phys. Oceanogr.*, 22, 1221–1227.

Ardhuin, F., L. Marié, N. Rascle, P. Forget, and A. Roland, 2009: Observation and Estimation of Lagrangian, Stokes, and Eulerian Currents Induced by Wind and Waves at the Sea Surface. *J. Phys. Oceanogr.*, 39, 2820–2838.

Barrick, D. E., 1972: First-Order Theory and Analysis of MF/HF/VHF Scatter from the Sea. *IEEE Transactions on Antennas and Propagation*, *20*, 2–10.

Barrick, D. E., M. W. Evans, and B. L. Weber, 1977: Ocean Surface Currents Mapped by Radar. *Science (80-.).*, 198, 138–144.

Bell, P. S., 1999: Shallow water bathymetry derived from an analysis of X-band marine radar images of waves. *Coast. Eng.*, 37, 513–527, doi:10.1016/S0378-3839(99)00041-1.

Bogden, P. S., Malanotte-Rizzoli, P., and Signell, R., 1996: Open-Ocean Boundary Conditions From Interior Data: Local and Remote Forcing of Massachusetts Bay. *J. Geophys. Res.*, *101*, 6487–6500.

Charnock, H., 1955: Wind stress on a water surface. *Q. J. R. Meteorol. Soc.*, 81, 639–640, doi:10.1002/qj.49708135026.

Cheng, N.-S., and A. W.-K. Law, 2001: Measurements of Turbulence Generated by Oscillating Grid. *J. Hydraul. Eng.*, 127, 201–208.

Clément, B, M., M. Gurvan, A. L. Fischer, A. Lazar, and D. Iudicone, 2004: Mixed layer depth over the global ocean: An examination of profile data and a profile-based climatology. *J. Geophys. Res.*, 109, C12003, doi:10.1029/2004JC002378.

Cohen, A. M., 2007: *Numerical Methods for Laplace Transform Inversion*. C. Brezinski, Ed. Springer, New York,. 252 pp.

Craig, P. D., and M. L. Banner, 1994: Modeling Wave-Enhanced Turbulence in the Ocean Surface Layer. *J. Phys. Oceanogr.*, 24, 2546–2559.

Crombie, D. D., 1955: Doppler Spectrum of Sea Echo at 13.56 Mc/s. *Nature*, 175, 681–682.

Dankert, H., and Rosenthal, W., 2004: Ocean surface determination from X-band radar-image sequences. *J. Geophys. Res.*, *109*(C4).

Dankert, H., J. Horstmann, and W. Rosenthal, 2003: Ocean wind fields retrieved from radar-image sequences. J. Geophys. Res., 108, doi:10.1109/IGARSS.2002.1026475.

Davis, R. E., R. Deszoeket, D. Halpern, and P. Niler, 1981: Variability in the upper ocean during MILE. Part I: The heat and momentum balances. *Deep. Res.*, 28, 1427–1451.

Drennan WM, Kahma KK, Terray EA, Donelan MA, Kitaigorodskii SA. 1992. Observations of the enhancement of kinetic energy dissipation beneath breaking wind waves. In *Breaking Waves: IUTAM Symposium* Sydney, Australia 1991, ed. ML Banner, RHJ Grimshaw, pp. 95-102. Berlinmeidelberg: Springer-Verlag. 387 pp.

Dugan, J. P., C. C. Piotrowski, and J. Z. Williams, 2001: Water depth and surface current retrievals from airborne optical measurements of surface gravity wave dispersion. *J. Geophys. Res.*, 106, 16903–16915, doi:10.1029/2000JC000369.

Dugan, J., Piotrowski, C., Zuckerman, S., Chinn, C., Yi, M., and Vierra, K., 2008: Near-surface current profile measurements using time series optical imagery. *IEEE/OES/CMTC 9th Working Conference on Current Measurement Technology*, Charleston, SC, Institute of Electrical and Electronics Engineers, 174–180.

Ekman, W. V., 1905: On the Influence of the Earth's Rotation on Ocean-Currents. *Ark. för Mat. Atronomi och Fys.*, 2, 1–53.

Fan, Y., I. Ginis, and T. Hara, 2010: Momentum Flux Budget across the Air–Sea Interface under Uniform and Tropical Cyclone Winds. *J. Phys. Oceanogr.*, 40, 2221–2242, doi:10.1175/2010JPO4299.1.

Fernandez, D. M., J. F. Vesecky, and C. C. Teague, 1996: Measurements of Upper Ocean Surface Current Shear with High-Frequency Radar. *J. Geophys. Res.*, 101, 28615–28625.

Gemmrich, J. R., and D. M. Farmer, 1999: Near-Surface Turbulence and Thermal Structure in a Wind-Driven Sea. *J. Phys. Oceanogr.*, 29, 480–499, doi:10.1175/1520-0485(1999)029<0480:NSTATS>2.0.CO;2.

Gemmrich, J., and D. M. Farmer, 2004: Strong Turbulence in the Wave Crest Region. *J. Phys. Oceanogr.*, 34, 1067–1086, doi:10.1175/2009JPO4179.1.

Godin, G. 1972: The Analysis of Tides. Liverpool University Press, 264 pp.

Golub, B. G. H., and Welsch, J. H., 1969: Calculation of Gauss Quadrature Rules. *Mathematics of Computation*, *23*, 221–230.

Graber, H. C., B. K. Haus, R. D. Chapman, and L. K. Shay, 1997: HF radar comparisons with moored estimates of current speed and direction: Expected differences and implications. *J. Geophys. Res.*, 102, 18749–18766, doi:10.1029/97JC01190.

Ha, E.C., 1979: Remote Sensing of Ocean Surface Current Shear by HF Backscatter Radar. *Doctoral Thesis*, 134 pp, Stanford University.

Halpern, D., 1977: Description of Wind and of Upper Ocean Current and Temperature Variations on the Continental Shelf off Northwest Africa during March and April 1974. *J. Phys. Oceanogr.*, *7*, 422–430.

Hannoun, I. a., H. J. S. Fernando, and E. J. List, 1988: Turbulence structure near a sharp density interface. *J. Fluid Mech.*, 189, 189–209, doi:10.1017/S0022112088000965.

Harlan, J., Allen, A., Howlett, E., Terrill, E., Kim, S. Y., Otero, M., Glenn, S., Roarty, H., Kohut, J., O'Donnell, J., and Fake, T., 2011: National IOOS high frequency radar search and rescue project, *Oceans 2011*, Waikoloa, HI, Institute of Electrical and Electronics Engineers, 1-9.

Harlan, J., Terrill, E., and Burnett, B., 2009: National high frequency radar network: Update, *OCEANS 2009, MTS/IEEE Biloxi - Marine Technology for Our Future: Global and Local Challenges.* Biloxi, MS, Institute of Electrical and Electronics Engineers, 1-25.

Hessner, K., and Bell, P. S., 2009: High resolution current and bathymetry determined by nautical X-Band radar in shallow waters. *Proc. OCEANS ´09 IEEE Bremen - Balancing technology with future needs*. Bremen, Germany, Institute of Electrical and Electronics Engineers, 1-5.

Hetland, R. D., 2006: Event-Driven Model Skill Assessment. *Ocean Modelling*, *11*(1-2), 214–223.

Hopfinger, E. J., and J.-A. Toly, 1976: Spatially decaying turbulence and its relation to mixing across density interfaces. *J. Fluid Mech.*, 78, 155–175, doi:10.1017/S0022112076002371.

Kelly, F. J., J. S. Bonner, J. C. Perez, D. Trujillo, R. H. Weisberg, M. E. Luther, and R. He, 2003: A Comparison of Near-Surface Current Measurements by ADCP and HF-Radar on the West Florida Shelf. *IEEE*, 70–74.

Kirby, J. T. (UF), and Chen, T.-M., 1989: Surface Waves on Vertically Sheared Flows: Approximate Dispersion Relations. *J. Geophys. Res.*, *94*, 1013–1027.

Kitaigorodskii, S. a, M. A. Donelan, J. L. Lumley, and E. A. Terray, 1983: Wave-Turbulence Interactions in the Upper Ocean. Part II: Statistical Characteristics of Wave and Turbulent Components of the Random Velocity Field in the Marine Surface Layer. *J. Phys. Oceanogr.*, 13, 1988–1983.

Kohut, J. T., Roarty, H. J., and Glenn, S. M., 2006: Characterizing Observed Environmental Variability with HF Doppler Radar Surface Current Mappers and Acoustic Doppler Current Profilers: Environmental Variability in the Coastal Ocean. *IEEE Journal of Oceanic Engineering*, *31*(4), 876–884.

Kundu, P. K., 1980: A Numerical Investigation of Mixed-Layer Dynamics. *J. Phys. Oceanogr.*, 10, 220–236.

Lund, B., H. C. Graber, H. Tamura, C. O. I. Collins, and S. M. Varlamoc, 2015: Journal of Geophysical Research : Oceans. *J. Geophys. Res. Ocean.*, 120, 8466–8486, doi:10.1002/2015JC010961.

Mellor, G. L., and T. Yamada, 1974: A Hierarchy of Turbulence Closure Models for Planetary Boundary Layers. *J. Atmos. Sci.*, 31, 1791–1806, doi:10.1175/1520-0469(1974)031<1791:AHOTCM>2.0.CO;2.

Mellor, G. L., and T. Yamada, 1982: Development of a Turbulence Closure Model for Geophysical Fluid Problems. *Rev. Geophys. Sp. Phys.*, 20, 851–875.

Melsom, A., and O. Sætra, 2004: Effects of Wave Breaking on the Near-Surface Profiles of Velocity and Turbulent Kinetic Energy. *J. Phys. Oceanogr.*, 34, 490–504, doi:doi:10.1175/1520-0485(2004)034<0490:EOWBOT>2.0.CO;2.

Melville, W. K., 1996: The Role of Surface-Wave Breaking in Air-Sea Interaction. *Annu. Rev. Fluid Mech.*, 28, 279–321, doi:10.1146/annurev.fl.28.010196.001431.

Melville, W. K., and P. Matusov, 2002: Distribution of breaking waves at the ocean surface. *Nature*, 417, 58–63, doi:10.1038/417058a.

Nieto Borge, J. C., RodrÍguez, G. R., Hessner, K., and González, P. I., 2004: Inversion of Marine Radar Images for Surface Wave Analysis. *J. Atmos. Oceanic Technol.*, *21*, 1291–1300.

Ohlmann, C., White, P., Washburn, L., Terrill, E., Emery, B., & Otero, M., 2007. Interpretation of Coastal HF Radar-Derived Surface Currents with High-Resolution Drifter Data. *J. Atmos. Oceanic Technol.*, *24*, 666–680.

Paduan, J. D., and L. K. Rosenfeld, 1996: Remotely sensed surface currents in Monterey Bay from shore- based HF radar (Coastal Ocean Dynamics Application Radar). *J. Geophys. Res.*, 101, 20669–20686.

Phillips, O.M., 1966: *The Dynamics of the Upper Ocean*. Cambridge University Press, 344 pp.

Phillips, O.M., 1977: The sea surface. Modelling and Prediction of the Upper Layers of the Ocean, E.B. Kraus, Ed., Pergamon, 229-237.

Plant, W. H., 1988: The modulation transfer function: Concept and applications. Radar Scattering from Modulated Wind Waves, G. J. Komen and W. A. Oost, Eds., Kluwer Academic, 155–172.

Rodi, W., 1987: Examples of calculation methods for flow and mixing in stratified fluids. *J. Geophys. Res.*, 92, 5305–5328, doi:10.1029/JC092iC05p05305.

Senet, C. M., J. Seemann, and F. Ziemer, 2001: The near-surface current velocity determined from image sequences of the sea surface. *IEEE Trans. Geosci. Remote Sens.*, 39, 492–505.

Senet, C. M., Seemann, J., Flampouris, S., and Ziemer, F., 2008: Determination of Bathymetric and Current Maps by the Method DiSC Based on the Analysis of Nautical X-Band Radar Image Sequences of the Sea Surface. *IEEE Transactions on Geoscience and Remote Sensing*, *46*, 2267–2279.

Shuchman, R., 1979: The Feasibility of Measurement of Ocean Current Detection using SAR Data*, Proc. of the 13th Int. Symp. on Remote Sensing of the Environment*, Ann Arbor, MI, International Center for Remote Sensing of Environment, 93–103.

Soloviev, A., and R. Lukas, 2003: Observation of wave-enhanced turbulence in the near-surface layer of the ocean during TOGA COARE. *Deep. Res. I*, 50, 371–395, doi:10.1016/S0967-0637(03)00004-9.

Stewart, R. H., and J. W. Joy, 1974: HF radio measurements of surface currents. *Deep. Res.*, 21, 1039–1049.

Stewart, R. W., and H. L. Grant, 1962: Determination of the Rate of Dissipation of Turbulent Energy near the Sea Surface in the Presence of Waves. *J. Geophys. Res.*, 67, 3177–3180.

Sullivan, P. P., J. C. McWilliams, and W. K. Melville, 2004: The oceanic boundary layer driven by wave breaking with stochastic variability. Part 1. Direct numerical simulations. *J. Fluid Mech.*, 507, 143–174, doi:10.1017/S0022112004008882.

Taylor, G. I., 1935: Statistical Theory of Turbulence. *Proc. R. Soc. London. Ser. A - Math. Phys. Sci.*, 151, 421–444.

Teague, B. C. C., J. F. Vesecky, and D. M. Fernandez, 1997: HF Radar Instruments, Past to Present. *Oceanography*, 40–44.

Teague, C. C., J. F. Vesecky, and Z. R. Hallock, 2001: A Comparison of Multifrequency HF Radar and ADCP Measurements of Near-Surface Currents During COPE-3. *IEEE J. Ocean. Eng.*, 26, 399–405.

Terray, E. a, M. a Donelan, Y. C. Agrawal, W. M. Drennan, K. K. Kahma, a J. Williams, P. a Hwang, and S. a Kitaigorodskii, 1996: Estimates of kinetic energy dissipation under breaking waves. *J. Phys. Oceanogr.*, 26, 792–807, doi:10.1136/bmj.1.4303.792. papers2://publication/uuid/1AA7C6FA-5421-44C9-BE18-D0582A431696.

Terrill, E. Otero, M., Hazard, L., Conlee, D., Harlan, J., Kohut, J., Reuter, P., Cook, T., Harris, T., and Lindquist, K, 2006: Data Management and Real-Time Distribution for HF Radar National Network. *Oceans 2006,* Boston, MA, Institute of Electrical and Electronics Engineers, 1–6.

Thompson, S. M., and J. S. Turner, 1975: Mixing across an interface due to turbulence generated by an oscillating grid. *J. Fluid Mech.*, 67, 349–368, doi:10.1017/S0022112075000341.

Thorpe, S. A., 1984: On the Determination of K_v in the Near-Surface Ocean from Acoustic Measurements of Bubbles. *J. Phys. Oceanogr.*, 14, 855–863.

Thorpe, S. A., 1992: Bubble clouds and the dynamics of the upper ocean. *Q.J.R. Metereological Soc.*, 118, 1–22.

Trizna, D., and Xu, L., 2006: Target classification and remote sensing of ocean current shear using a dual-use multifrequency HF radar. *IEEE Journal of Oceanic Engineering*, *31*(4), 904–918.

Twomey, S., 1977: *Introduction to the Mathematics of Inversion in Remote Sensing and Indirect Measurements*. Dover Publications, 237 pp.

Umlauf, L., and H. Burchard, 2003: A generic length-scale equation for geophysical. *J. Mar. Res.*, 61, 235–265, doi:10.1357/002224003322005087.

Umlauf, L., H. Burchard, and K. Hutter, 2003: Extending the k-ω turbulence model towards oceanic applications. *Ocean Model.*, 5, 195–218, doi:10.1016/S1463-5003(02)00039-2.

Watson, G., Robinson, I.S., 1990. A Study of internal wave propagation in the Strait of Gibraltar using shore-based marine radar images *J. Phys. Oceanogr.*, 20, 374–395.

Weber, B. L., and D. E. Barrick, 1977: On the Nonlinear Theory for Gravity Waves on the Ocean's Surface Part I: Derivations. *J. Phys. Oceanogr.*, 7.

Weber, J. E., 1983: Steady wind-and wave-induced currents in the open ocean. *J. Phys. Oceanogr.*, 13, 524–530.

Weeks, W. T., 1966: Numerical Inversion of Laplace Transforms Using Laguerre Functions. *Journal of the Association for Computing Machinery*, *13*, 419–426.

Wilcox, D. C., 1988: Reassessment of the scale-determining equation for advanced turbulence models. *AIAA J.*, 26, 1299–1310, doi:10.2514/3.10041.

Wu, J., 1969: An Estimation of Wind Effects on Dispersion in Wide Channels. *Water Resour. Res.*, 5, 1097–1104.

Wunsch, C., 1996: *The Ocean Circulation Inverse Problem*. Cambridge University Press, 442 pp.

Young, I. R., W. Rosenthal, and F. Ziemer, 1985: A Three-Dimensional Analysis of Marine Radar Images for the Determination of Ocean Wave Directionality and Surface Currents. *J. Geophys. Res.*, 90, 1049–1059.